UNIVERSIDADE
BEIRA INTERIOR

Analytical and Numerical Analysis of Euler-Bernoulli Beams: Telescopic Beam Deflection

(versão final após defesa)

Duarte André Bombas

Dissertação para obtenção do Grau de Mestre em
Engenharia Aeronáutica
(Mestrado Integrado)

Orientador: Prof. Doutor Pedro Vieira Gamboa

julho de 2021

Dedicatória

À minha mãe e ao meu pai

Agradecimentos

Em primeiro lugar gostaria de agradecer aos meus pais, pelo apoio incondicional que me deram, por estarem sempre do meu lado e ajudado nas decisões mais difíceis e importantes da minha vida, por nunca me deixarem desamparado e por garantirem que devo sempre seguir os meus sonhos e para onde quer que vá na vida, ser feliz.

Em seguida, um agradecimento especial ao meu irmão Bernardo, com o qual convivo todos os dias e fez parte importante do meu percurso académico; e à minha irmã Carolina, que sempre se preocupa comigo e com quem não consigo partilhar tantos momentos quantos gostaria. Amo-vos.

A todos os meus amigos, por partilharem comigo os melhores momentos da vida académica e boémia e sem os quais não seria a pessoa que sou hoje.

À minha família da Desertuna, com a qual conheci o país e pude partilhar o meu gosto pela música e pisar muitos palcos por Portugal fora.

Ao meu orientador, o Professor Doutor Pedro Gamboa, por me apoiar durante o desenvolvimento deste trabalho e por todo o conhecimento que partilhou comigo durante o ano que passou e com quem sei que poderei contar no futuro.

Por fim, quero agradecer à cidade do meu coração, que me deu mais do que eu alguma vez poderei retribuir. "E quando um dia me lembrar da minha universidade, dos anos de estudante, que guardo com saudade. *Recordações-Desertuna*"

Resumo

A adaptação da morfologia de aeronaves é cada vez mais importante de modo a melhorar significativamente a sua adaptação à missão a desempenhar. Aeronaves de envergadura variável são estudadas há já bastante tempo e estão provados os seus benefícios em termos de eficiência e desempenho. No entanto, são geometrias estruturalmente complexas e difíceis de analisar.

Este estudo surge com o intuito de simplificar dita geometria e analisar as deformações que ocorrem numa viga telescópica sujeita a uma carga distribuída ao longo da sua envergadura e de que forma diferentes tipos de apoios entre os segmentos que a constituem e determinadas diferenças estruturais podem influenciar significativamente, ou não, essas mesmas deformações.

Nesta dissertação é assumida uma análise teórica de vigas de Euler-Bernoulli, cuja principal característica é desprezar as forças de corte ao longo da envergadura da viga, admitindo que as secções transversais são perpendiculares ao eixo neutro antes e após a deformação. Esta teoria é usada devido ao facto de se lidar com pequenas deflexões e admitindo que a viga não diminui as suas dimensões no eixo longitudinal após a deformação.

De modo a testar os três diferentes tipos de mecanismos telescópicos, é importante saber quais as características que são necessárias para o correto estudo das deformações. Em primeiro lugar, os dois segmentos têm diferentes valores de rigidez à flexão. Em segundo lugar, os tipos de suporte usados entre os segmentos são diferentes, sendo para o Caso 1 um suporte de viga encastrada; para o Caso 2 uma viga em suspensão com um suporte simples; e para o Caso 3 um viga em suspensão com contacto contínuo entre os dois segmentos. Para a análise analitica e numérica os parâmetros usados são o comprimento total da viga (L), os comprimentos de cada segmento (L_0, L_1 e L_2), as razões entre esses comprimentos e o comprimento total da viga (K_{L_0} e K_{L_2}) e a razão entre a rigidez à flexão de cada um dos segmentos (K_{EI}). Estes parâmetros são usados de modo a obter resultados adimensionalizados.

Procede-se então à análise analítica e obtenção das equações que descrevem o comportamento de deformação das vigas. Posteriormente, efetuou-se a análise numérica dos mesmos casos com recurso a ferramentas computacionais de elementos finitos para que se possam comparar estes resultados com os da análise analítica.

Com isto, pretende-se perceber como é que estes tipos de apoios e alterações no tamanho dos segmentos influenciam as deformações e com que veracidade e acuidade tais equações descrevem as mesmas. É também proposta a hipótese de que existe uma margem ideal do comprimento do segmento telescópico em que a deflexão da ponta da viga diminui, antes de voltar a aumentar até ao seu valor máximo.

Palavras-chave

Viga telescópica, Euler-Bernoulli, rotação, deflexão e Método de Elementos Finitos.

Abstract

Aircraft morphology adaptation is a subject that is becoming increasingly more important in order to significantly improve its adaptation to the mission to perform. Variable wingspan aircraft have been studied for a while now and its benefits in terms of efficiency and performance are well known. However, they have a type of geometry that is structurally complex and difficult to analyze.

This study appears with the purpose of simplifying said geometry and analyze the displacements that occur on a telescopic beam subjected to a certain load distributed along its span and in what way different types of supports between its constituent segments and certain structural differences can influence significantly, or not, such displacements.

In this dissertation it is assumed a theoretical analysis of Euler-Bernoulli beams, whose primary characteristic is to neglect the shear strains along the beam's length, admitting that plane cross-sections are perpendicular to the axis before and after the deformation. This theory is used due to the fact that this study only deals with small deflections and assuming that the beam does not decrease its dimensions on the longitudinal axis after the displacements.

To test the three different cases of telescopic beam mechanisms, it is important to know what characteristics are necessary for a correct study of the displacements. Firstly, the two different segments have different flexural rigidities. Secondly, the types of supports used between the segments are different, being for Case 1 a cantilever beam support; for Case 2 a simply supported overhanging telescopic mechanism; and for Case 3 an overhanging telescopic support with a continuous contact. For both the analytical and numerical analysis, the parameters used are the total length of the beam (L), each segment's length (L_0, L_1 and L_2), the ratios between those lengths and the total length of the beam (K_{L_0} and K_{L_2}) and the ratio between the flexural rigidity of the tip and root segments (K_{EI}). These parameters are used in order to obtain non-dimensionalized results.

The analytical analysis is carried out and the equations that describe the deformation behavior of the beams are obtained. Posteriorly, the numerical analysis of the same cases is performed with the aid of finite element analysis computational tools, in order to compare those results with the former ones.

With this, it is intended to understand how these types of support mechanisms and segment size alterations influence the deformations and what is the veracity and acuity of the equations that describe them. It is also proposed the hypothesis that an ideal margin of length of the telescopic segment exists where the beam's tip deflection decreases, before it reaches its maximum value.

Keywords

Telescopic beam, Euler-Bernoulli, rotation, deflection and Finite Element Method.

Contents

List of Figures

List of Tables

List of Acronyms

FEA	Finite Element Analysis
FEM	Finite Element Method

Nomenclature

I	Area Moment of Inertia
M	Bending Moment
A	Cross-sectional Area
y	Deflection
x_a, x_b, x_c	Discontinuity Points
j, r	Distributed Load
w	Distributed Load
K_{EI}	Flexural Rigidity Ratio
δ_x	Horizontal Displacement for large deflections
$A_1, A_2, B_1, B_2, C_1, C_2$	Integration Constants
x, u	Integration Variables
L	Length
K_{L_0}, K_{L_2}	Length Ratios
$\frac{dy}{dx}$	Rotation
L_0, L_1, L_2	Segment Lengths
Q	Shear Force
G	Shear Modulus
φ	Slope
k	Timoshenko Coefficient
δ_y	Vertical Displacement for large deflections
E	Young's Modulus of Elasticity

Chapter 1

Introduction

Technology was defined as “a material entity created by the application of mental and physical effort to nature in order to achieve some value” by Radovan Richta, who also coined the term “technological evolution” in his first work “Man and Technology in the Revolution of Our Day” (1963) [1]. In order to achieve this value, Humanity evolves its methods and tools, seeking the best possible solutions to the obstacles that slowly appear in its way.

Like in all fields of study such as Medicine, Economics, Engineering and Physics, the Aeronautics and Aviation industry also feels the need to evolve in order to keep up with modern society and their demands, whether it is for the comfort of the population or the need to create a solution for a problem that had not been considered until due time.

One common problem that has been around since the dawn of aviation is the constraints that every aircraft has according to its task, i.e. different aircraft for different missions. Aerospace structures are usually designed as ”passive” systems, i.e. their topology, geometry and material is defined during the development process in order to satisfy a set of different requirements with minimum weight [2].

With this in mind, it would be much simpler if we could have some type of aircraft capable of adaptation mid-flight in order to use the best characteristics in different flight stages, having a fleet of a single morphing aircraft capable of being utilized on different mission objectives and flight conditions, as opposed to a fleet of several aircraft types, each designed for a specific mission objective and function [3].

Being a field of constant change and ever-growing technology, the aviation industry has made enormous progress in the area of wing design and optimization, resorting to the change of wing and airfoil shape in order to obtain better performance, such as flight envelope, flight control and flight range [3]. This alteration of wing and airfoil shape, known as morphing, will lead to improvements in the performance and efficiency of the aircraft and, according to Weisshaar [4], is defined as ”a set of technologies that increase a vehicle’s performance by manipulating certain characteristics to better match the vehicle’s state to the environment and task at hand”.

Morphing wings are not a novelty in the aeronautical industry. Commercial aircraft already use geometry changes with the deployment of their flaps and slats to adapt wing morphology to certain flight conditions. However, this adaptation does not allow the best geome-

try/performance commitment of the aircraft for each flight condition, as the latter is usually substandard due to limitations to only a few flight stages and bring smaller benefits compared to adaptable wing configurations.

In the field of aeronautics, ”shape morphing” has been used to identify those aircraft that undergo certain geometrical changes to enhance or adapt to their mission profiles [5]. Since there is no compliance on the scope of geometrical changes that are required to place an aircraft in the ”shape morphing” family, a fixed definition of what it means to be a ”shape morphing” aircraft and what changes places them as such, does not yet exist. Ignoring conventional control surfaces which provide discrete geometry changes, such as flaps or slats, as a type of wing morphing seems to be one of the few agreements amongst the aeronautical research community so far by not being ”powerful” enough to cause significant changes in aircraft performance at all stages due to their singular functionality nature and they are only operated for a very short period of time along the flight envelope. In addition, they are only applied locally along the airframe, and they are designed not to carry the flight loads [5].

Outside this short period of working time, these control surfaces can have a neutral or negative aerodynamic influence, thus lowering efficiency. Conventional hinged mechanisms are effective in controlling the airflow, but they are not efficient, as the hinges and other junctions usually create discontinuities in the surface, resulting in unwanted fluid dynamic phenomena [6].

According to Reich and Sanders [7], some of the major challenges that need to be addressed in terms of ”shape morphing” are distributed high-power density actuation concepts, structural mechanization concepts, flexible skins and control law development. These changes must occur during the entire flight process and adapt for different flight stages in order to provide the best performance and efficiency.

The differences between the small changes caused by control surfaces such as slats, flaps, landing gears, etc., and the bigger changes that provide more noticeable performance and efficiency improvements at all flight stages, makes it possible for us to organize them as Discrete and Continuous Morphing, respectively [8]. Table 1.1 encapsulates the more significant differences between them:

Table 1.1: Definitions of Discrete and Continuous Morphing. Adapted from R. Ajaj *et al.* [8].

Discrete Morphing	***Continuous Morphing***
Singular functionality.	Multiple functionalities.
Adopted locally on board the aircraft.	Adopted all over the body of the aircraft.
Operated at few points of the flight envelope.	Operated continuously along the flight envelope.
Suppress coupling between the aircraft axis.	Exploit couplings in morphing schedules and between the aircraft axis.

1.1 Morphing

With wing and airfoil changes becoming one of the most researched and already used forms of ”shape morphing”, we need to understand in what way do these geometry alterations appear and what benefits we can obtain by using them.

Aircraft wings are usually optimized for a specific design point [2]. This point, chosen in the design phase, is the one that allows the aircraft to reach the best aerodynamic performance. Outside that design point, where flight conditions are different, a loss of wing efficiency will emerge. Here is where wing morphing gains its importance, by adapting the geometry of the wing in order to achieve the best behavior in a much wider range of conditions.

Wing morphing concepts can be classified into three major types, as seen in Figure 1.1: planform transformation, out-of-plane transformation, and airfoil adjustment.

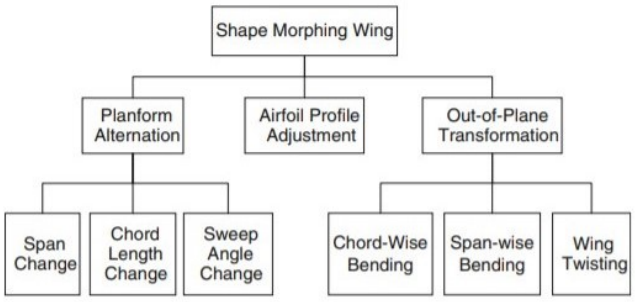

Figure 1.1: Classification for shape morphing of wing: (I) planform alternation, (II) out-of-plane transformation, (III) airfoil profile adjustment. A. Sofla *et al* [5].

In the matter of planform transformation i.e., the shape of the wing we see from above, alterations of wing area, being transformations of sweep, span resizing, and chord length changes are approached, whereas in the matter of out of plane transformation i.e., changes are no longer constrained to the same plane as the wing, chord and span-wise camber changes are included, such as wing twisting and chord and span-wise bending. Airfoil adjustment is about the designs that change the wing profile but may or may not alter wing camber.

In this chapter only planform alternations, in particular changes in span length, will be discussed, as out-of-plane transformations and airfoil adjustments are not relevant for this study.

1.1.1 Wing planform alternation: Changes in span length

Wing planform alteration can be achieved by the resizing of span length, chord length and by the change of sweep angle or even a combination of all of them, as seen in Figure 1.2. The first two directly affect the wing’s aspect ratio, hence altering lift-to-drag ratio.

Neal et al. designed and demonstrated a variable planform aircraft capable of different wing

morphing combinations. The adaptive model is designed to achieve large scale shape changes in order to investigate morphing for multi-mission UAVs. There are five independent planform changes along with independent twist control for each wing.

It was concluded that a 38% change in span, 40 degrees of sweep change, 12% change in chord length and 20 degrees of wing twist that the vehicle undergoes, prove to maintain low drag throughout a various range of lift coefficients and to be beneficial to the aircraft flight conditions [9].

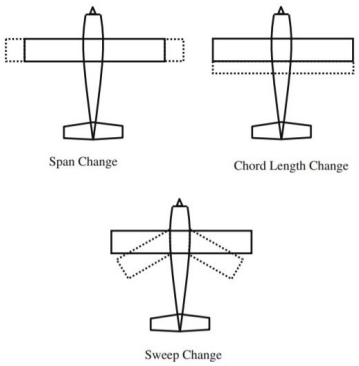

Figure 1.2: The three different types of planform alternation: Span change (top-left), chord length change (top right) and sweep change (bottom). A. Sofla *et al* [5].

1.2 Motivation

Fixed high aspect-ratio wings have an advantage in fuel efficiency and lateral stability but lack maneuverability and operate at relatively low cruise speeds. On the other hand, aircraft with low-aspect-ratio wings are faster and have better maneuverability, however, show mediocre aerodynamic efficiency.

With these two seemingly opposite configurations in mind, variable-span wings appear with the potential to bring together the advantages of both designs. From an aerodynamic perspective, the change in aspect-ratio produces differences in lift curve slope and forces due to the change in the wing area [6].

From Figure 1.3, we can understand that a higher aspect ration means a higher lift coefficient and vice-versa.

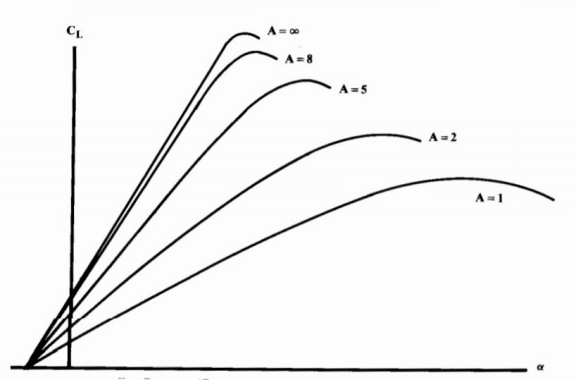

Figure 1.3: Effect of aspect ratio on lift. Daniel P. Raymer [10]

1.2.1 Telescopic wings

The concept of variable geometry wings is owed to russian engineer and inventor Yvan Makhonine, who first introduced the telescopic wing on the Mak-10 research aircraft in September 1929, in France, and such aircraft scheme and configuration had never been built.

This aircraft had a telescopic mechanism that allowed the wing's outer parts to retract inside the root parts of the wing and whose wingspan could vary from $13m$ to $21m$ (a 62% increase) and wing area that could vary from $19m^2$ to $33m^2$ (a 57% increase) [4]. By doing this, harmful resistance was significantly reduced when flying at high speed. After 4 years of improvements, the aircraft gained the designation of Mak-101.

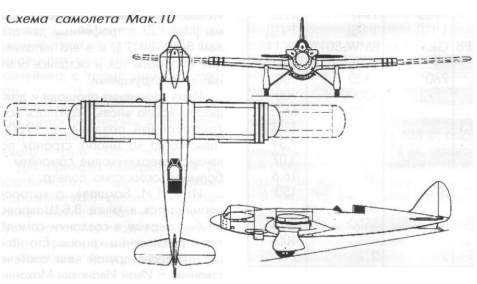

(a) Mak-10 blueprint with variable wingspan.

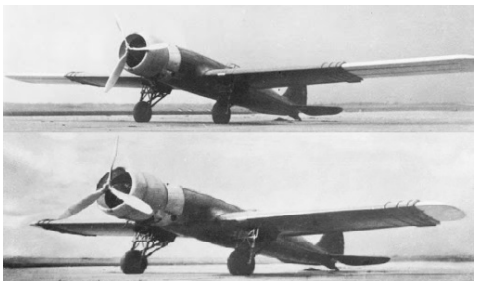

(b) Mak-101 with maximum wingspan (up) and minimum wingspan (down).

Figure 1.4: Mak-10 and Mak-101 with variable wingspan. Adapted from [11] and [12].

Telescopic structures have been extensively used and studied for dire length changes of the wing structure. The morphing wing in the telescopic configuration is sectioned longitudinally to form at least two segments with consecutive reducing cross-sectional area, such that each segment can be accommodated in the adjacent inner segment with minimum sliding clearance. Given the required length change, the number of segments can be determined.

As mentioned above, by increasing wingspan, we increase aspect-ratio and wing area, which in turn decreases span-wise lift distribution (for the same lift) thus decreasing the drag of the wing. On the other hand, this increment of wingspan generates a bigger bending moment of the wing root and a larger deflection of the wing tip.

It has been found in previous studies that the tip deflection of a wing whose span is variable, by means of a telescopic mechanism, could depend on the flexural rigidity EI of each material that constitutes the different parts of the wing and also the portion of length of the two parts of the wing that are in contact with each other. Results [13] show that for a semi-span of $2m$, a moving fraction of 5% would cause a displacement of $0.0416m$ on the wing tip, a moving fraction of 20% would cause a displacement of $0.0338m$ of the wing tip and a moving fraction of 30% would cause a displacement of $0.0560m$ of the wing tip. These results indicate that an ideal margin of wing movement exists in which the wing tip suffers a minimum amount of deflection, thus creating the main goal of this study.

1.3 Scope of current study

The main objective of this study is to understand how the portion of length of the two parts of the wing that are in contact with each other, a ratio between the flexural rigidities of those two parts and the type of support between the telescopic and fixed wing parts influence the wing tip deflection and why it decreases in a certain interval of contact length and then increases again to higher values.

The problem will be simplified by studying a simple geometry of a telescopic beam, instead of a more complex wing geometry, to obtain results that support this hypothesis and after that, a Finite Element Analysis will be presented in order to support the analytical analysis of the beams.

This will happen by analyzing three different cases and configurations of telescopic beams with different support types between each part.

1.4 Outline

The first chapter of this dissertation is composed of the introduction and the motivation, with the state-of-the-art on some important notions for this study. Also, the scope of the current study and the main objectives are described in this chapter as well as the outline of the dissertation.

Chapter 2 presents the state-of-the-art of types of beams and the different theories that explore this important structural element as well as the main differences between large and small deflections of cantilever beams. It also presents an introduction to Finite Element Analysis.

Chapter 3 commences the analytical analysis of the different cases, the theory applied and the equations for displacements that are obtained and its calculations.

Chapter 4 presents the numerical analysis of the three cases, how the FEM is applied and

chosen and how the structural models were built.

Chapter 5 exposes the results of the analytical analysis and the plots obtained with the equations for displacement and discusses them.

Chapter 6 presents the results for the FEM analysis and compares them with the results from Chapter 5.

Chapter 7, the final chapter, sums up the entire results of this study and the conclusions drawn from them, as well as possible future work that can come from this study.

Chapter 2

Literature Review

2.1 Beams

A beam is a structural element designed to resist loads applied crosswise to the beam's axis. Its primarily mode of deflection is by bending and the loads applied to it result in reaction forces at its support points. The total effect of all the forces acting on the beam produce shear forces and bending moments within the beam, thereby inducing internal stresses, strains and deflections of the beam.

Beams are characterized by their type of support, cross-section shape, equilibrium conditions, length and material. The most common beam types of support are:

- Cantilever – a projecting beam fixed only at one end.
- Simply supported – a beam supported on the ends which are free to rotate and have no moment resistance.
- Over hanging – a simple beam extending beyond its support on one end.
- Continuous – a beam extending over more than two supports.
- Fixed ended – a beam supported on both ends and restrained from rotation.
- Cantilever simply supported – a beam fixed at one end and supported on the free end.

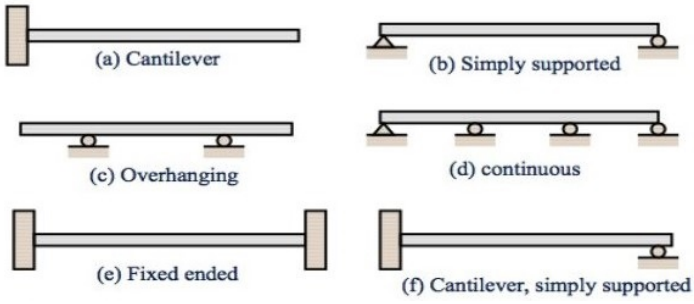

Figure 2.1: Different types of beam support. Adapted from [14].

The first three types of beams represent *statically determinate* beams since the reactions at the supports, produced by a given load, can be determined from the equations of statics.

Deflection is the degree to which a structural element is displaced under a certain load and it can be a distance or an angle. By integrating the function that describes the slope of the deflected shape, we can calculate the deflection distance of that member to which the load is being applied.

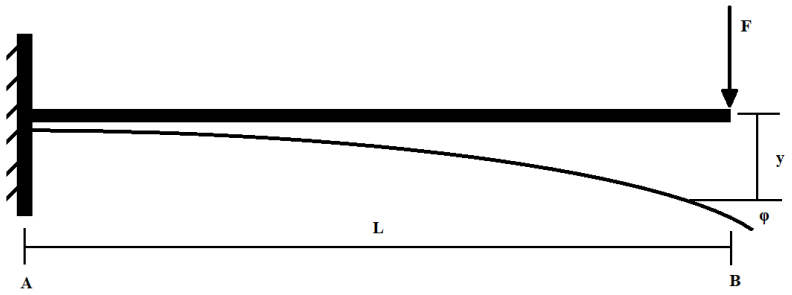

Figure 2.2: Deflection (y) and slope (φ) of a cantilevered beam.

The equation regarding the beam's deflection (y) can be approximated as:

$$\frac{d^2y(x)}{dx^2} = \frac{M(x)}{E(x)I(x)} \quad (2.1)$$

where the second derivative of its deflected shape with respect to x is interpreted as its curvature, E is the Young's modulus, I is the area moment of inertia of the cross-section, and M is the internal bending moment in the beam.

2.2 Euler-Bernoulli beam theory

Beam models are often used at a pre-design stage because they provide valuable insight into the behavior of structures. Such calculations are also quite useful when trying to validate purely computational solutions [15].

Several theories of beam analysis have been developed through the years based on various assumptions and often lead to different levels of accuracy, from the simplest models to some theories that require finding solutions to intricate differential equations. One of those simple models is also one of the primary tools for structural analysis of beams and is commonly called the Euler–Bernoulli beam equation. This equation accurately describes the elastic behavior of slender beams where the cross-sectional dimensions are small compared to the length of the beam ($L/t >> 10$).

In the Euler-Bernoulli (or simple) beam theory, it is assumed that plane cross-sections perpendicular to the axis of the beam are infinitely rigid in its own plane and remain plane and perpendicular to the axis after deformation.

This assumption implies that all transverse shear strains are zero [16].

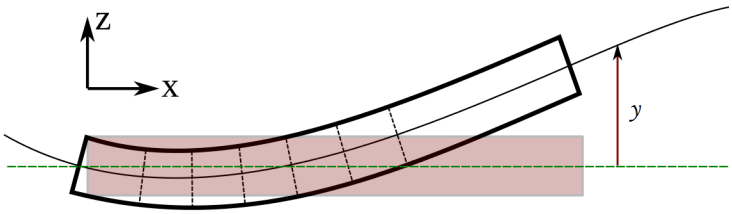

Figure 2.3: Euler-Bernoulli deflected beam with cross-sections at 90º with beam's neutral axis. Adapted from [17].

The Euler–Bernoulli equation describes the relationship between the beam's deflection and the applied load [18]:

$$\frac{d^2}{dx^2}\left(EI\frac{d^2y}{dx^2}\right) = w \quad (2.2)$$

By modeling the beam as a one-dimensional object, the curve y describes the deflection of the beam at some position and w represents a distributed load acting on the beam. I must be calculated with respect to the axis which passes through the centroid of the cross-section and which is perpendicular to the applied loading (neutral axis). If the product between the Young's module E and the area moment of inertia I, known as flexural rigidity, is constant, the previous equation can be written as follows:

$$EI\frac{d^4y}{dx^4} = w(x) \quad (2.3)$$

By successive derivation of the deflection equation (y), we obtain other physical meanings such as the beam slope dy/dx, bending moment M in the beam (2.4) and shear force Q in the beam (2.5).

The beam slope is equivalent to the first derivative of the deflection because we consider small deflections, thus the derivative is the slope of the tangent of each point along the neutral axis so it can be considered as the rotation of the beam.

$$M = -EI\frac{d^2y}{dx^2} \quad (2.4)$$

$$Q = -\frac{d}{dx}\left(EI\frac{d^2y}{dx^2}\right) \quad (2.5)$$

After we determine the deflection y due to a certain load w, we can use equations 2.4 and 2.5 to calculate the stresses in the beam.

Figure 2.4 represents the variation of bending moment M, shear force Q and deflection y in a cantilever beam with a uniformly applied load. At the fixed end of the beam there cannot be any displacement or curvature of the beam, which means that at that end, both rotation and deflection are zero. At the free end of the beam, with no external moments applied, bending

moment is zero, and maximum at the clamped end. Shear force is zero at the free end since dM/dx is zero and no external forces are applied. The boundary conditions for this situation are as follows:

- Fixed end

$$y|_{x=0} = 0 \qquad \left.\frac{\partial y}{\partial x}\right|_{x=0} = 0 \quad (2.6)$$

- Free end

$$\left.\frac{\partial^2 y}{\partial x^2}\right|_{x=L} = 0 \qquad \left.\frac{\partial^3 y}{\partial x^3}\right|_{x=L} = 0 \quad (2.7)$$

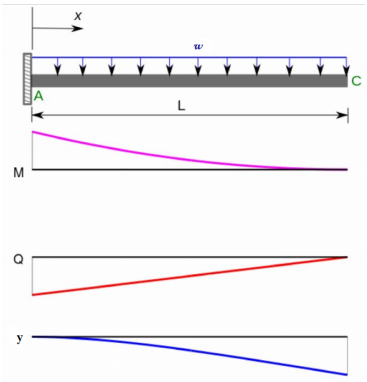

Figure 2.4: Bending moment and shear force diagram. Adapted from [17].

2.3 Timoshenko's beam theory

For beams that are not slender, a different theory needs to be adopted to account for the deformation due to shear forces and, in dynamic cases, the rotary inertia. The beam formulation adopted here is that of Timoshenko, which we will approach next.

As stated before, the simple beam theory is based on the assumption that straight lines normal to the midplane before deformation remain straight and normal to the midplane after deformation. Although the assumption leads to a very simple fourth-order differential equation for solving the deflection of the beam, it suppresses any transverse shearing strain.

This leads to an inconsistent beam theory where on one hand the constitutive shear force is zero but on the other hand the shear force must be nonzero for equilibrium of beams under transverse loads [19].

Timoshenko's more refined beam theory eases the plane cross-sections' normality assumption, which means sections remain plane but not necessarily normal to the longitudinal axis after deformation (Fig. 2.5), admitting a nonzero transverse shear strain, thus a constant

shear stress through the beam thickness.

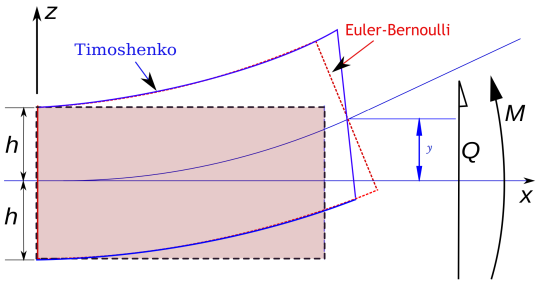

Figure 2.5: Cross-section differences between Euler-Bernoulli and Timoshenko's beam theory. Adapted from [20].

The governing equations for a Timoshenko beam that describes the relation between the beam's deflection and the applied load are the following coupled system of differential equations:

$$\frac{d^2}{dx^2}\left(EI\frac{d\varphi}{dx}\right) = w(x) \quad (2.8)$$

$$\frac{dy}{dx} = \varphi - \frac{1}{kAG}\frac{d}{dx}\left(EI\frac{d\varphi}{dx}\right) \quad (2.9)$$

By neglecting the last term, the Timoshenko beam theory is equivalent to the Euler-Bernoulli beam theory when

$$\frac{EI}{kL^2AG} << 1$$

proves valid.

In equations 2.8 and 2.9, φ represents the beam's rotation, L is the length of the beam, A is the cross-section area, G is the shear modulus and k is the Timoshenko shear coefficient. Combining the two equations for a constant cross-section beam we obtain:

$$EI\frac{d^4y}{dx^4} = w(x) - \frac{EI}{kAG}\frac{d^2w}{dx^2} \quad (2.10)$$

The bending moment M and the shear force Q in the beam are related to the deflection y and rotation φ, which for a linear elastic Timoshenko beam can be written as:

$$M = -EI\frac{\partial\varphi}{\partial x} \quad (2.11)$$

$$Q = kAG\left(-\varphi + \frac{\partial y}{\partial x}\right) \quad (2.12)$$

Figure 2.6 represents the variation of bending moment M, shear force Q and deflection y of a cantilever beam with a uniformly applied load. Similar to the Euler-Bernoulli theory, at the

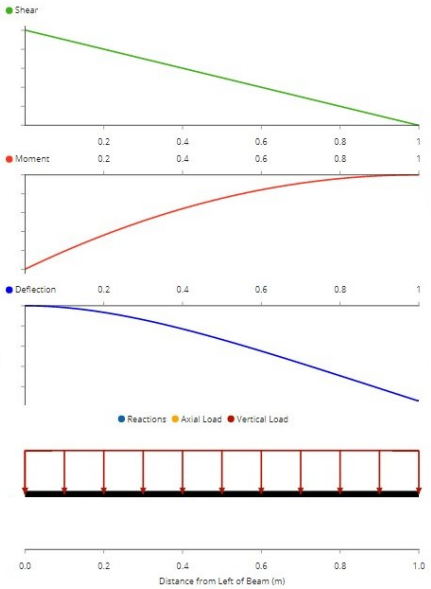

Figure 2.6: Bending moment and shear force diagram of a cantilever beam for large deflections.

clamped end there cannot be any displacement or rotation of the beam hence both deflection and slope are zero at that end and have maximum value at the free end. At the free end of the beam, if there are no external moments applied, bending moment is zero and so is the shear force, if no external forces are applied. Bending moment has maximum value at the fixed end. The boundary conditions for this situation are as follows:

- Fixed end

$$y|_{x=0} = 0 \qquad \left.\frac{\partial y}{\partial x}\right|_{x=0} = 0 \quad (2.13)$$

- Free end

$$\left.\frac{\partial^2 y}{\partial x^2}\right|_{x=L} = 0 \qquad \left.\frac{\partial^3 y}{\partial x^3}\right|_{x=L} = 0 \quad (2.14)$$

2.4 Large and small deflections of a cantilever beam

The deflection of a cantilever beam is essentially a three-dimensional problem. An elastic stretching in one direction is accompanied by a compression in the perpendicular directions: the ratio is known as Poisson's ratio. However, we can ignore this effect when the length of the beam is larger than the thickness of the perpendicular cross-section and this is shorter than the curvature radius of the beam [21].

The main difference between large and small deflections is the displacement in the x axis. A large beam deflection will significatively decrease the length of the deflected shape compared

to the non-deflected beam length, whereas in small deflections, the length of the deflected shape can be considered the same as the non-deflected beam.

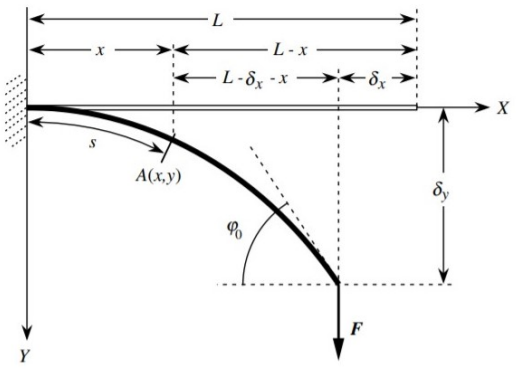

Figure 2.7: Cantilever beam loaded with an external vertical concentrated load at the free end and the parameters for large deflections. T. Belendez *et al.*[22].

Figure 2.7 [22] shows a cantilever beam of length L with a concentrated load F applied at the free end of the beam and where δ_x and δ_y are the horizontal and vertical displacements at the free end, respectively, and φ_0 takes into account the maximum slope of the beam. These large deflections cannot be obtained from simple beam theories because the assumptions are no longer valid as they neglect the square of the first derivative in the curvature formula and provide no correction for the shortening of the moment arm, as the loaded end of the beam deflects.

For small deflections, these theories are valid because we assume that the curvature of the deflection curve depends, at any point, only on the magnitude of the bending moment at that point and shear force effects on the curvature are neglected, as was stated before. This relationship between the curvature and bending moment allows us to use elementary beam theories such as the Euler-Bernoulli beam theory and thus the equation:

$$M = -EI\frac{d^2y}{dx^2} \quad \text{(2.4 revisited)}$$

In the next chapter, the problem regarding this study will be introduced and the process and steps taken to approach it will be explained thoroughly. Also, the analytic study and calculations will be presented to better understand the problem at hand.

2.5 Finite Element Method

The previous sections presented an overview of the analytic methods and theories that can be used to analyze and approach beam related problems. However, because the problems related to structural analysis usually involve thousands of unknowns and complex mathematical expressions, even though the derivation of such expressions is not of great difficulty, obtaining its solutions by exact methods of analysis is an extremely laborious task. Hence

the need for computer assisted solving methods where the finite element method and its multidisciplinary computations come in hand.

The finite element method is a procedure for the numerical solution of the equations that govern the problems found in nature, i.e. mathematically speaking, it is a numerical technique for solving partial differential or integral equations. When referred to the analysis of structures the finite element method is a powerful method for computing the displacements, stresses and strains in a structure under a set of loads [23].

This method allows us to come up with solutions, as a set of numbers, for the mathematical expressions that describe the problem by transforming them into a set of algebraic equations which depend on a finite set of parameters.
A finite element can be visualized as a small portion of a whole (*continuum*). The word *finite* distinguishes a portion from the *infinitesimal* elements of differential calculus. The complex geometrical domain of the *continuum* is considered to be formed by an assembly of a collection of non-overlapping sub-domains with simple geometry named finite elements. Over each finite element, the approximation functions are derived using the basic idea that any continuous function can be represented by a linear combination of algebraic polynomials [24].

This collection of sub-domains that discretize the *continuum* is called a *mesh*, which can be seen in Figure 2.8.

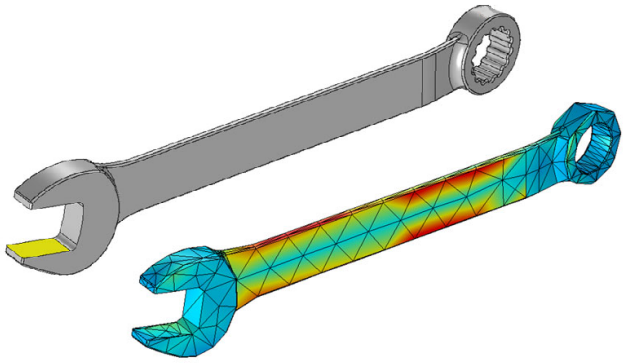

Figure 2.8: Solid object and respective mesh. Adapted from [25].

Since the exact analytical variation of such parameters is more complex and generally unknown, the finite element method only provides an approximation to the exact solution. Knowing what a finite element is and its use, it is important to structure the problem and know the steps involved in computing the approximate value of its solution.

Firstly, we need to identify the problem before we analyze the structure: which are the more relevant physical phenomena influencing the structure; is the problem of static or dynamic nature; are the material properties linear or non-linear; which are the key results requested

and what is the level of accuracy sought. Answering these questions is essential for selecting a structural model and the adequate computational method [23].

With the problem duly identified, the structural model must be chosen and built. This mathematical model must include some key aspects:

• Finite element discretization: the domain of the *continuum* is represented as a collection of sub-domains - a mesh of finite elements - of which we have the description of its geometrical components, such as points, lines, surfaces and volumes;

• Mathematical expression of the basic physical laws that govern the behavior of the structure, such as force-equilibrium equations and boundary conditions;

• Specification of the properties of the materials and of the loads acting on the structure.

• Assembly of element equations and solution: the approximate value of the solution is obtained by putting together the element properties in a meaningful way.

• Convergence and error: the modeling and discretization of the structure are two error sources. Improving the conceptual and structural models which describe the behavior of the structure can reduce the modeling associated errors. The discretization error can be reduced by using a finer mesh, i.e. with more elements (Fig. 2.9) or increasing the accuracy of the elements chosen, using higher order polynomial expansions for approximating the displacement field within each element. Reducing mesh and model associated errors leads to a numerical solution that converges to the mathematical one (more approximate).

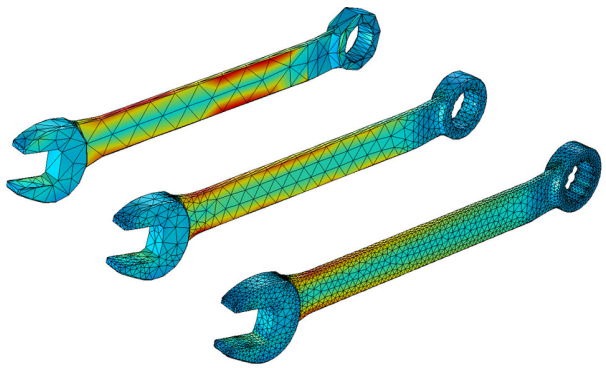

Figure 2.9: Successively finer mesh for the same object. Adapted from [25].

After obtaining the structural model and the solutions, it is important to wonder how should confidence in modeling and computation be critically assessed. This way, *Verification* and *Validation* of the results are the primary methods for building and quantifying this confidence.

Fundamentally, validation is the assessment of the accuracy of the structural and computational models by comparison of the numerical results with experimental data. The correct

definition of the experimental tests and the reliability of the experimental results are crucial issues in the validation process. On the other hand, verification is all about determining if the underlying structural model and its solution are accurately represented by the computational model. This means that, unlike validation, the relationship between the numerical results to the real world is not an important issue.

Comparing the numerical results for the problem with exact analytically obtained solutions allows us to obtain such verification. This verification must pass through *code verification*, to establish confidence in the mathematical model and solution algorithms, and *calculation verification*, to establish confidence that the discrete solution of the mathematical model is accurate [23].

To sum things up, verification allows to check that we are solving structural problems accurately, whereas validation tell us that we are solving the right problem.

In Chapter 4, the methods and procedures approached in this chapter are applied to the different beams, and the results later analyzed.

Chapter 3

Analytical Deflection of Compound Beams

In this chapter, after understanding what a telescopic beam is and how its mechanism works, as well as the different beam theories that can be used to approach the problem at hand, we begin the development of analytical models for three compound built-in beams.

In order to understand how the deflection at the tip of telescopic beams is influenced by certain parameters that can be variable or not, such as the length that can be altered or the flexural rigidity of the material that composes the beam's parts, which is a property of the material and cannot be changed, the complexity of this beam was brought down to a simple beam that represents a regular wing (Fig. 3.1).

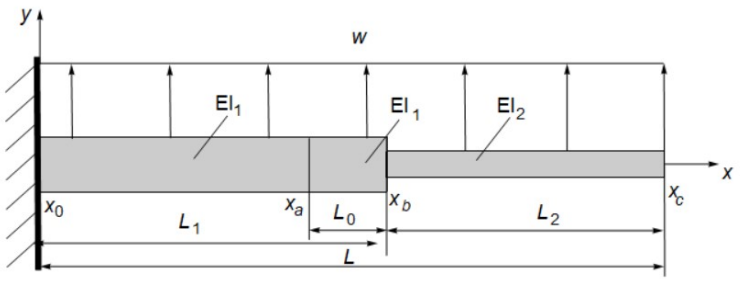

Figure 3.1: General representation of the wing as a beam for the three cases.

After that simplification, we assess the effect of different types of support between telescopic and fixed wing parts on the deflection shape of the beam. This beam is slender, of constant cross-section for each part that composes the telescopic mechanism and its cross-section is small compared to its length and normal to the x plane before and after the deflection.

Assuming small deflections, the Euler-Bernoulli beam theory is the one chosen to apply in order to study the beam's deformations, which are hereinafter referred to as displacements. The three cases that are studied are:

- Case 1: A cantilever beam constituted by two parts, clamped to each other.
- Case 2: A cantilever beam constituted by two parts, with the telescopic one simply supported to the fixed one and overhanging.
- Case 3: A cantilever beam in continuous contact with the telescopic part that slides inside the latter.

Understanding the different cases that are going to be analyzed is of the utmost importance. In every case the main goal is, for the most part, the same, which is trying to find a simplification for the equations that describe the rotation and deflection of the beams, as a function of the flexural rigidities and lengths of the different parts and compare them to a uniform beam.

Equation 3.1 represents the function that we are trying to obtain:

$$\frac{y}{y_{EIconstant}} = f(K_{EI}, K_{L_2}, K_{L_0}) \quad (3.1)$$

With Figure 3.1 in mind, the following assumptions are taken in consideration:

$$K_{EI} = \frac{EI_2}{EI_1} \quad (3.2)$$
$$K_{L_2} = \frac{L_2}{L} \quad (3.3)$$
$$K_{L_0} = \frac{L_0}{L} \quad (3.4)$$

which represent the ratio between the flexural rigidities (3.2) and lengths (3.3 and 3.4). The following assumptions represent the relationships between the distances and values.

$$L_2 = K_{L_2} L \quad (3.5)$$
$$L_1 = L(1 - K_{L_2}) \quad (3.6)$$
$$L_0 = K_{L_0} L \quad (3.7)$$
$$x_0 = 0 \quad (3.8)$$
$$x_a = L(1 - K_{L_2} - K_{L_0}) \quad (3.9)$$
$$x_b = L(1 - K_{L_2}) \quad (3.10)$$
$$x_c = L \quad (3.11)$$
$$\overline{x} = \frac{x}{L} \quad (3.12)$$

Applying the inequality $L_2 + L_0 \leq L_1$, we obtain the following constraint:

$$0 \leq K_{L_2} \leq \frac{1}{2}(1 - K_{L_0}) \quad (3.13)$$

As stated in 1.2.1, a telescopic mechanism implies that at least two different parts exist; one on the outside that is the root part and another one that slides inside the first. Before we start the analysis, we will talk about the control group. In line with what was said before, every case will be compared to the uniform beam and this will allow us to strengthen the ability to draw conclusions on the study.

That control group is a cantilevered beam with a uniformly distributed load. This guarantees that the rotation and deflection are caused only by the applied load by assuming that the deflection due to its self-weight is zero. This implies considering a massless beam [21].

Also, whenever there is a discontinuity on the beam, i.e. a change between segments occurs, it is imperative that the equations which describe the displacements are continuous, in order to guarantee a continuous function of displacement. With this in mind, we shall start analyzing the three different cases of beams that are approached in this study, which differ in the way that each part that composes it is attached to one another.

3.1 Control group - Uniform beam

In order to compare the different beams, it is important to understand how the general mechanism of a beam works and the general and simple equations that describe the displacements of said beam. In Figure 3.2 a simplified representation of the uniform beam is visible, with constant cross-section and material along its length, with a uniformly distributed applied load and with a fixed end (left side) and a free end (right side). Calculating the bending moment and shear force equations, allows us to obtain the rotation and deflection of the beam and we can use them to make the comparisons on this study.

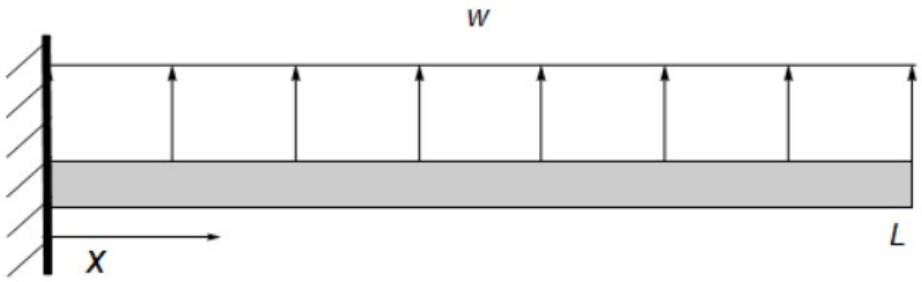

Figure 3.2: Uniform beam schematic

The shear force and bending moment equations are, for the uniform beam:

$$Q = w(L - x) \tag{3.14}$$
$$M = -\frac{w}{2}(L - x)^2 \tag{3.15}$$

Substituting the bending moment equation above in equation 2.4 allows us to obtain the equations for curvature, rotation and deflection of the uniform beam by integrating in x and making use of 3.12:

$$\frac{d^2y}{dx^2} = \frac{wL^2}{2EI}(1 - 2\overline{x} + \overline{x}^2) \tag{3.16}$$
$$\frac{dy}{dx} = \frac{wL^3}{6EI}(3\overline{x} - 3\overline{x}^2 + \overline{x}^3) \tag{3.17}$$
$$y = \frac{wL^4}{24EI}(6\overline{x}^2 - 4\overline{x}^3 + \overline{x}^4) \tag{3.18}$$

Replacing $\overline{x} = 1$ gives us the equations of displacement at the tip of the beam, i.e. the point where the displacements have the highest value, and the equations that are going to be used for the comparison between the different cases and this control beam. With the equations for the basic type of beam well know, the analysis of the three cases can proceed.

3.2 Case 1 - Cantilever beams

For the first case, the telescopic mechanism is represented by two cantilever beams in a way that one is clamped to a wall, representing the part clamped to the fuselage, and the other one is clamped to the first beam, representing the second part of the wing. Figure 3.3 is a schematic of the two different cross-section' beam with a uniformly applied distributed load w.

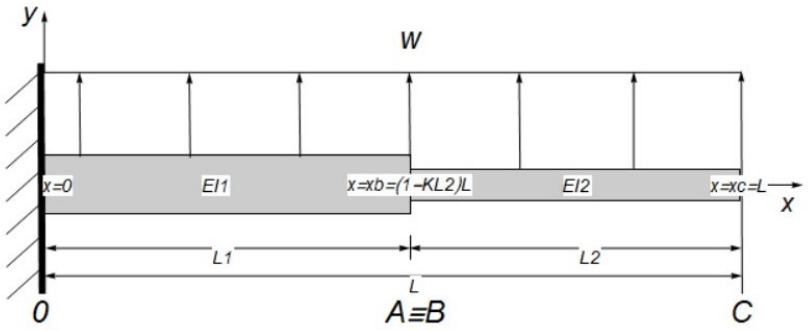

Figure 3.3: Telescopic beam schematic of Case 1.

3.2.1 Reactions

Assuming that EI_1 and EI_2 are the flexural rigidities of the root and tip parts, respectively, and $L_0 = 0$, therefore L being the total length of the beam such that $L = L_1 + L_2$, it is defined for the free body diagram that the y axis is positive pointing upwards, the x axis is positive to the right and moment is positive in the counter-clockwise direction. Next, we calculate the reactions at $x = 0$ (Fig. 3.4), obtaining the following equations for the bending moment and shear force:

$$M_0 = -\frac{wL^2}{2} \quad (3.19)$$

$$Q_0 = -wL \quad (3.20)$$

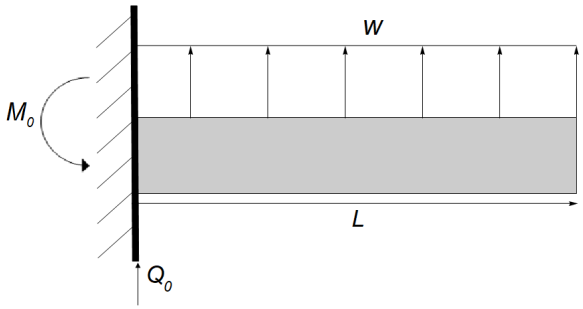

Figure 3.4: Reactions on the beam at $x = 0$.

We calculate the reactions at $x = x_b$ in a similar way (Fig. 3.5) solving $\Sigma F = 0$ and $\Sigma M = 0$

and making use of the free body diagram, obtaining:

$$M_B = -\frac{wL_2^2}{2} \quad (3.21)$$

$$Q_B = -wL_2 \quad (3.22)$$

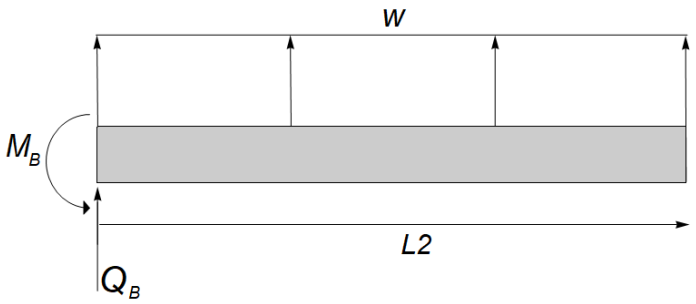

Figure 3.5: Reactions on the beam at $x = x_b$.

With this, we have obtained the value of the bending moment and shear force on both clamped sides of the two parts of the beam.

3.2.2 Bending moment and shear force equations

Following the rule of sign for bending moments by defining the bending moment as positive in the clockwise direction, we obtain the equations regarding the bending moment and shear force on the opposite sides of the ones we just calculated, therefore obtaining, for $0 \leq x \leq x_b$:

$$M = M_0 - Q_0 x - \frac{w}{2}x^2 \quad (3.23)$$

$$Q = -Q_0 - wx \quad (3.24)$$

By substituting equations 3.19 and 3.20 in equation 3.23 and equation 3.24, one gets:

$$M = -\frac{w}{2}(L - x)^2 \quad (3.25)$$

$$Q = w(L - x) \quad (3.26)$$

and because $A \equiv B$, at $x = x_b$:

$$M_A = M_B = -\frac{w}{2}(L - x_b)^2 \quad (3.27)$$

$$Q_A = Q_B = w(L - x_b) \quad (3.28)$$

Finally, using again the rule of sign of bending moments, we can calculate the bending moment and shear force at $x_b < x \leq x_c$, obtaining:

$$M = -\frac{w}{2}x^2 + (wx_b - Q_B)x - \frac{w}{2}x_b^2 + Q_B x_b + M_B \quad (3.29)$$

$$Q = -Q_B - w(x - x_b) \quad (3.30)$$

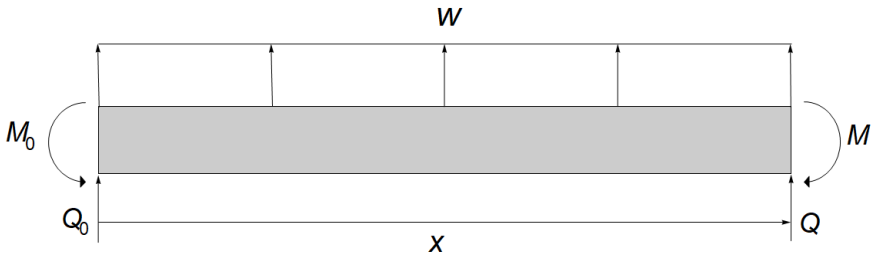

Figure 3.6: Reactions on the beam at $0 \leq x \leq x_b$.

By substituting equations 3.21 and 3.22 in equation 3.29 and equation 3.30, we obtain:

$$M = -\frac{w}{2}(L - x)^2 \quad (3.31)$$

$$Q = w(L - x) \quad (3.32)$$

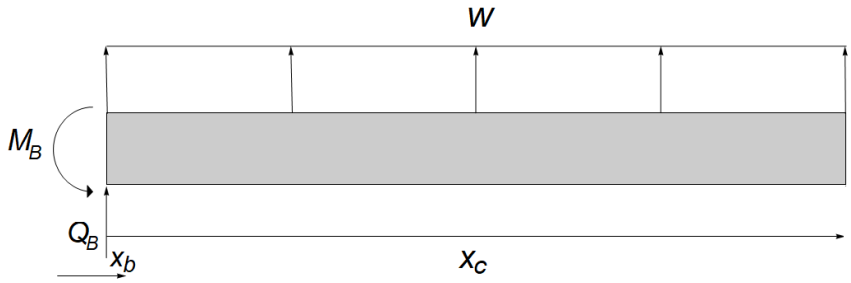

Figure 3.7: Reactions on the beam at $x_b < x \leq x_c$.

Now that the equations that represent the variation of the bending moment and shear force for $0 \leq x \leq x_b$ and $x_b < x \leq x_c$ have been obtained, we can assume an Euler-Bernoulli beam with its curvature given by the following equation:

$$\frac{d^2y}{dx^2} = -\frac{M}{EI} \quad (3.33)$$

and obtain the rotation and deflection by integrating once and twice, respectively.

Using the equations stated above it is possible to draw a representation of the shear force and bending moment diagrams represented by Figure 3.8 and with its variation along the beam's length.

3.2.3 Rotation and Deflection with Euler-Bernoulli Theory

In order to obtain the equation that defines the rotation and deflection of the beam for $0 \leq x \leq x_b$ and $x_b < x \leq x_c$, we will now substitute the equations of the bending moment of each part of the beam in equation 3.33 and proceed to integrate in x. To facilitate the calculations,

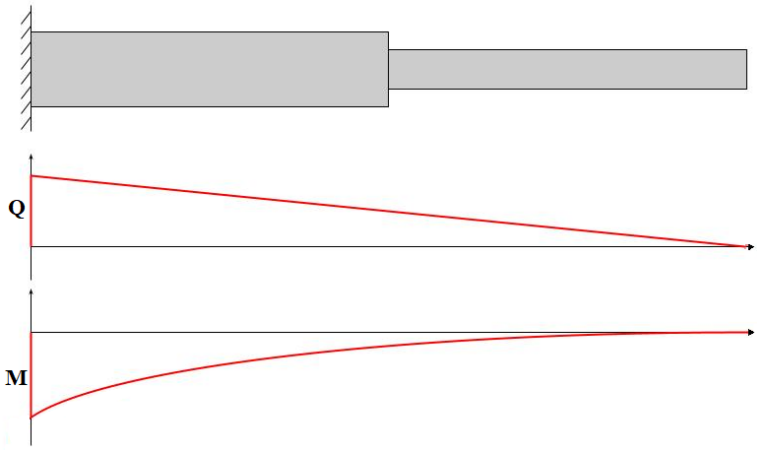

Figure 3.8: Shear Force and Bending Moment diagram representation of Case 1.

we use assumptions 3.10, 3.11 and 3.12 whenever it is necessary and introduce one more:

$$\overline{x}_b = (1 - K_{L_2}) \quad (3.34)$$

With these new assumptions, we are able to extract L from the equations and obtain the rotation and deflection as a non-dimensionalized function of x/L.

- From root to point $A \equiv B$: $0 \leq \overline{x} \leq (1 - K_{L_2})$

$$\frac{d^2y}{dx^2} = \frac{w}{2EI_1}\left(x^2 - 2Lx + L^2\right) \quad (3.35)$$

$$\frac{dy}{dx} = \frac{w}{2EI_1}\left(\frac{x^3}{3} - Lx^2 + L^2x\right) + B_1 \quad (3.36)$$

$$y = \frac{w}{2EI_1}\left(\frac{x^4}{12} - \frac{Lx^3}{3} + \frac{L^2x^2}{2}\right) + B_1x + B_2 \quad (3.37)$$

As we can see from above, equation 3.35 is obtained by using equation 3.25 in equation 3.33 and describes the curvature of the beam, equation 3.36 describes the rotation of the beam and equation 3.37 describes the deflection of the beam. In order to obtain the value of the constants B_1 and B_2, we make use of the boundary conditions 2.6 and conclude that at $x = 0$, $\frac{dy}{dx} = 0$ and $y = 0$. Thus, $B_1 = B_2 = 0$.
Simplifying comes:

$$\frac{dy}{dx} = \frac{wL^3}{6EI_1}\left(3\overline{x} - 3\overline{x}^2 + \overline{x}^3\right) \quad (3.38)$$

$$y = \frac{wL^4}{24EI_1}\left(6\overline{x}^2 - 4\overline{x}^3 + \overline{x}^4\right) \quad (3.39)$$

Next, we obtain the equations of the rotation and deflection at the point of discontinuity

$A \equiv B$, i.e., $\overline{x} = \overline{x}_b$, and substitute:

$$\left(\frac{dy}{dx}\right)_B = \frac{wL^3}{6EI_1}\left(3\overline{x}_b - 3\overline{x}_b^2 + \overline{x}_b^3\right) \quad (3.40)$$

$$(y)_B = \frac{wL^4}{24EI_1}\left(6\overline{x}_b^2 - 4\overline{x}_b^3 + \overline{x}_b^4\right) \quad (3.41)$$

- From point $A \equiv B$ to point C : $(1 - K_{L_2}) < \overline{x} \leq 1$

$$\frac{d^2y}{dx^2} = \frac{w}{2EI_1K_{EI}}\left(x^2 - 2Lx + L^2\right) \quad (3.42)$$

$$\frac{dy}{dx} = \frac{w}{2EI_1K_{EI}}\left(\frac{x^3}{3} - Lx^2 + L^2x\right) + C_1 \quad (3.43)$$

$$y = \frac{w}{2EI_1K_{EI}}\left(\frac{x^4}{12} - \frac{Lx^3}{3} + \frac{L^2x^2}{2}\right) + C_1x + C_2 \quad (3.44)$$

Just as it was done for $0 \leq \overline{x} \leq (1 - K_{L_2})$, we replaced the respective bending moment equation (eq. 3.31), for $(1 - K_{L_2}) < \overline{x} \leq 1$, in equation 3.33 and integrated in x to obtain the equation for the curvature (eq. 3.42), the equation for the rotation (eq. 3.43) and the equation for the deflection (eq. 3.44).

Assumption 3.2 is also applied, in the form of $EI_2 = K_{EI}EI_1$, in the above equations to simplify calculations. This time, due to the discontinuity point and because $L_0 = 0$, from assumptions 3.7 and 3.9 we obtain $x_a = x_b$, hence point A is equivalent to point B and the rotation and deflection at that point have the same value. This being said, we obtain the following boundary conditions:

$$\frac{dy}{dx} = \left(\frac{dy}{dx}\right)_B \text{ at } x = x_b \quad (3.45)$$

$$y = (y)_B \text{ at } x = x_b \quad (3.46)$$

In order to obtain the values of C_1 and C_2, we compute equations 3.43 and 3.44 with respect to C_1 and C_2, respectively, and make use of the boundary conditions above to substitute 3.45 in equation 3.43 and 3.46 in equation 3.44, and obtain:

$$C_1 = \frac{wL^3}{6EI_1}\left(3\overline{x}_b - 3\overline{x}_b^2 + \overline{x}_b^3\right)\left(1 - \frac{1}{K_{EI}}\right) \quad (3.47)$$

$$C_2 = \frac{wL^4}{24EI_1}\left(-6\overline{x}_b^2 + 8\overline{x}_b^3 - 3\overline{x}_b^4\right)\left(1 - \frac{1}{K_{EI}}\right) \quad (3.48)$$

With C_1 and C_2 calculated, we can replace their values in equations 3.43 and 3.44, with assumptions 3.12 and 3.34 and simplify, in order to obtain the final equations regarding the rotation and deflection of the beam in $(1 - K_{L_2}) < \overline{x} \leq 1$. This simplification leads us to the

following equations that only depend on EI_1, K_{EI}, K_{L_2}, L and $\overline{x}$:

$$\frac{dy}{dx} = \frac{wL^3}{6EI_1}\left[\frac{1}{K_{EI}}(3\overline{x} - 3\overline{x}^2 + \overline{x}^3) + \left(1 - \frac{1}{K_{EI}}\right)\left(1 - K_{L_2}^3\right)\right] \quad (3.49)$$

$$\begin{aligned} y = \frac{wL^4}{24EI_1}\Bigg\{ & \frac{1}{K_{EI}}(6\overline{x}^2 - 4\overline{x}^3 + \overline{x}^4) \\ & + \left(1 - \frac{1}{K_{EI}}\right)\Big[-1 - 3K_{L_2}^4 - 4K_{L_2}^3(-1 + \overline{x}) + 4\overline{x}\Big]\Bigg\} \end{aligned} \quad (3.50)$$

After these calculations, we can conclude that the equations that describe the rotation and deflection of the beam are, for $0 \leq \overline{x} \leq (1 - K_{L_2})$ equations 3.38 and 3.39 and for $(1 - K_{L_2}) < \overline{x} \leq 1$ equations 3.49 and 3.50, respectively.

If we substitute $\overline{x} = 1$, which is the equivalent to have $x = L$ on the previous equations, we obtain the equations regarding the rotation and deflection at the tip of the beam:

$$\left(\frac{dy}{dx}\right)_L = \frac{wL^3}{6EI_1}\left[\frac{1}{K_{EI}} + \left(1 - \frac{1}{K_{EI}}\right)\left(1 - K_{L_2}^3\right)\right] \quad (3.51)$$

$$(y)_L = \frac{wL^4}{24EI_1}\left[\frac{3}{K_{EI}} + \left(1 - \frac{1}{K_{EI}}\right)\left(3 - 3K_{L_2}^4\right)\right] \quad (3.52)$$

Equations 3.53 and 3.54 represent the ratio between the beam's rotation and deflection and the rotation and deflection equations for a uniform beam, at $x = L$:

$$\frac{\left(\frac{dy}{dx}\right)_L}{\left(\frac{dy}{dx}\right)_U} = 1 + \left(-1 + \frac{1}{K_{EI}}\right)K_{L_2}^3 \quad (3.53)$$

$$\frac{(y)_L}{(y)_U} = 1 + \left(-1 + \frac{1}{K_{EI}}\right)K_{L_2}^4 \quad (3.54)$$

Now it is possible to plot these equations to better understand the problem at hand and visualize how the rotation and deflection change along the beam, how it changes at the tip and what differences exist with a uniform beam, which are visible in 5.1.

3.3 Case 2 - Simply supported overhanging telescopic beam

For the second case, the telescopic mechanism is represented by a cantilever beam that represents the root part of the wing clamped to the fuselage, and a tip part that slides freely inside the first one and is a simply supported beam with four support points.

For this case, we will use assumptions 3.2, 3.3 and 3.4. Figure 3.9 represents the telescopic beam configuration for Case 2, and just as the first one, with an applied uniformly distributed load w.

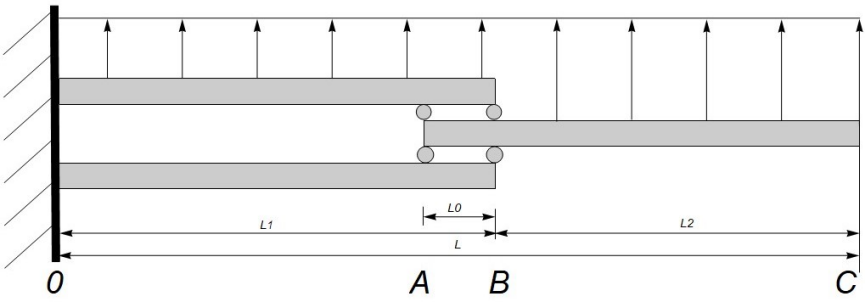

Figure 3.9: Telescopic beam schematic for Case 2.

3.3.1 Reactions

Assuming that EI_1 and EI_2 are the flexural rigidities of the root and tip parts, respectively, and L the total length of the beam such as $L = L_1 + L_2$, it is defined for the free body diagram that the y axis is positive pointing upwards, the x axis is positive to the right and moment is positive in the counter-clockwise direction.

In this case, it is necessary to assume that we deal, once again, with small deflections and the plane's cross-sections remain perpendicular to the x axis after the deformation. Next, assuming 3.9, 3.10 and 3.11, we get the following diagram:

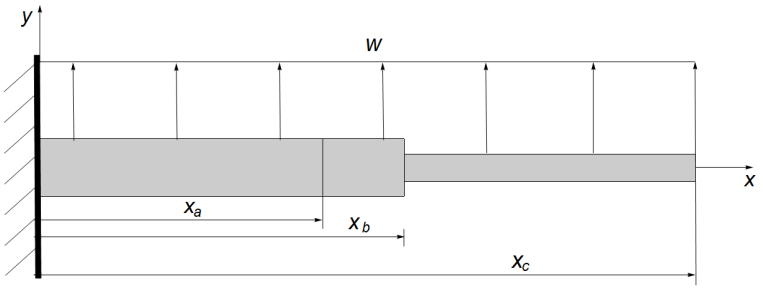

Figure 3.10: Case 2 diagram.

and proceed to calculate, just as was done for the first case, the reactions at $x = 0$ (Fig. 3.11), obtaining the following equations for the bending moment and shear force:

$$M_0 = -\frac{wL^2}{2} \quad (3.55)$$

$$Q_0 = -wL \quad (3.56)$$

3.3.2 Forces at Interface

In order to calculate either one of the forces at the interface between the root and tip parts of the beam (F), that are a result of the uniformly applied distributed load w (Fig. 3.12), we calculate the reactions only for the tip part of the beam, which allows us to calculate such forces rather easily. For that, the bending moment is calculated at the point at which force

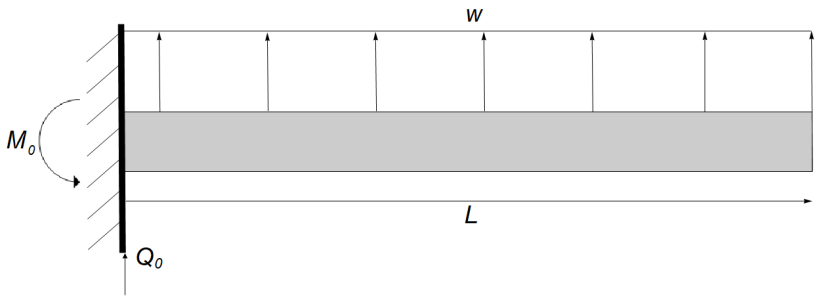

Figure 3.11: Reactions on the beam at $x = 0$.

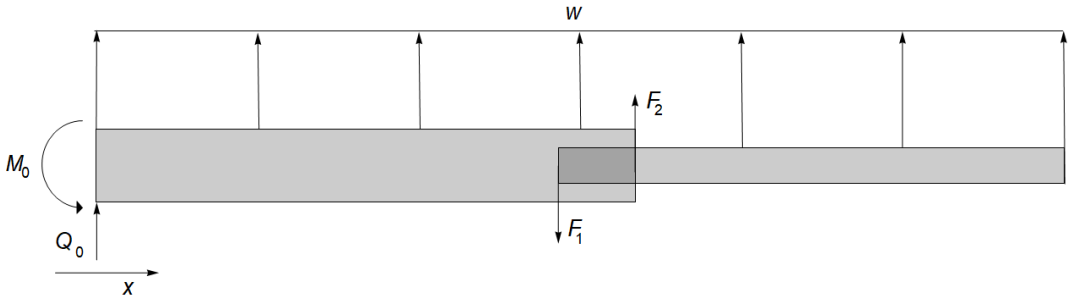

Figure 3.12: Reactions on the beam with F_1 and F_2 represented.

F_2 is applied and the load w is only applied to the outside segment of the tip part of the beam, being only distributed in $x_c - x_b$. Figure 3.13 represents the schematic used to calculate those reactions. Making use of the rule of sign of bending moments, with bending moment positive in the clockwise direction, and solving $\Sigma M = 0$ and $\Sigma F = 0$ we obtain the equations needed to calculate the values of F_1 and F_2:

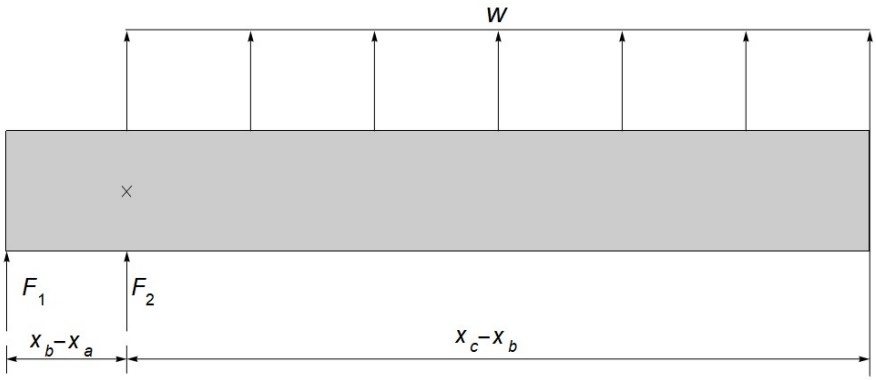

Figure 3.13: Reactions on the tip part of the beam used to calculate F_1 and F_2.

$$\Sigma M = 0 \Leftrightarrow F_1(x_b - x_a) - \frac{w}{2}(x_c - x_b)^2 = 0 \quad (3.57)$$

$$\Sigma F = 0 \Leftrightarrow F_1 + F_2 + w(x_c - x_b) = 0 \quad (3.58)$$

Simplifying and replacing $L_2 = x_c - x_b$, we obtain the final values of F_1 and F_2 which we can now substitute in the bending moment and shear force equations next, for each segment of

the beam:

$$F_1 = \frac{wL_2^2}{2L_0} \tag{3.59}$$

$$F_2 = -wL_2\left(1 + \frac{L_2}{2L_0}\right) \tag{3.60}$$

After F_1 and F_2 are calculated, we reverse its directions to apply to the root part of the beam, i.e, F_1 pointing downwards and F_2 also pointing downwards due to its negative value.

3.3.3 Bending moment and shear force equations

Again, following the rule of sign for bending moments, the equations for bending moment and shear force are obtained by solving $\Sigma M = 0$ and $\Sigma F = 0$, which represent the sum of all moments and sum of all forces, respectively, in each of the respective segments of the beam.

This way, we get for $0 \leq x < x_a$:

$$M = M_0 - Q_0 x - \frac{w}{2}x^2 \tag{3.61}$$

$$Q = -wx - Q_0 \tag{3.62}$$

From equations 3.55 and 3.56, we substitute in equations 3.61 and 3.62 and obtain the following simplified equations:

$$M = -\frac{w}{2}(L - x)^2 \tag{3.63}$$

$$Q = w(L - x) \tag{3.64}$$

and at $x = x_a$:

$$M_A = -\frac{w}{2}(L - x_a)^2 \tag{3.65}$$

$$Q_A = w(L - x_a) \tag{3.66}$$

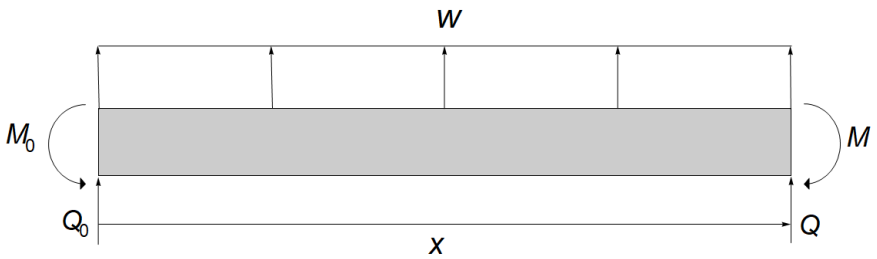

Figure 3.14: Reactions on the beam at $0 \leq x < x_a$.

For $x_a \leq x < x_b$, the process is similar but it is necessary to take into account the reaction caused by the supports on the beam because, unlike Case 1 where the different parts of the beam are cantilevered consecutively to one another, in this case the segments overlap as the

tip part slides inside the root one and has two points of support.

To help us understand, Figure 3.15 represents the next segment, where F_1 is the force caused by the load w.

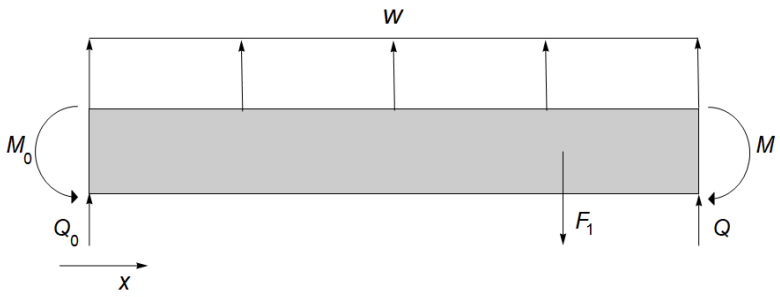

Figure 3.15: Reactions on the beam at $x_a \leq x < x_b$.

Now, it is possible to write the equations for bending moment and shear force at $x_a \leq x < x_b$, with the applied force F_1:

$$M = M_0 - \frac{w}{2}x^2 - Q_0 x + F_1(x - x_a) \quad (3.67)$$

$$Q = -wx - Q_0 + F_1 \quad (3.68)$$

which simplifying with 3.55, 3.56 and 3.59 comes:

$$M = -\frac{w}{2}(L - x)^2 + \frac{wL_2^2}{2L_0}(x - x_a) \quad (3.69)$$

$$Q = w\left(L + \frac{L_2^2}{2L_0} - x\right) \quad (3.70)$$

To obtain the equations for $x = x_b$, force F_2 appears, because it is the point where it is applied, just as we see in Figure 3.16. At x_b two values exist: the value immediately before that point, given by equation 3.70, and 0, given by equation 3.68 plus F_2, which results in equation 3.72 (already simplified). Replacing x by x_b just as supposed to, we obtain the value 0 for the shear force at that point.

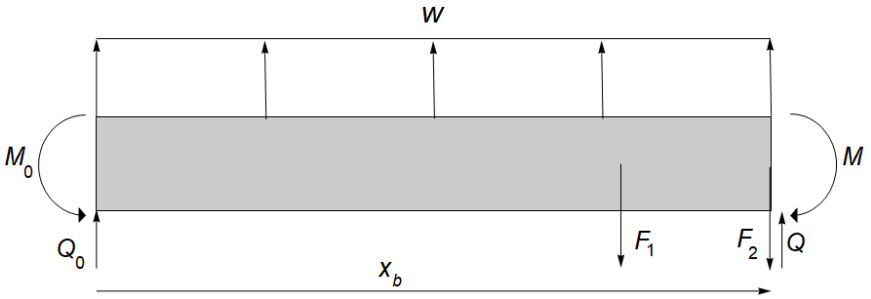

Figure 3.16: Reactions on the beam at $x = x_b$.

Thus obtaining:

$$M_B = -\frac{w}{2}(L - x_b)^2 + \frac{wL_2^2}{2L_0}(x_b - x_a) \quad (3.71)$$

$$Q_B = w(x_b - x) = 0 \quad (3.72)$$

For the last segment, $x_b \leq x \leq x_c$, both forces caused by the load w appear apllied on the beam and the following schematic can be drawn to better understand the applied forces.

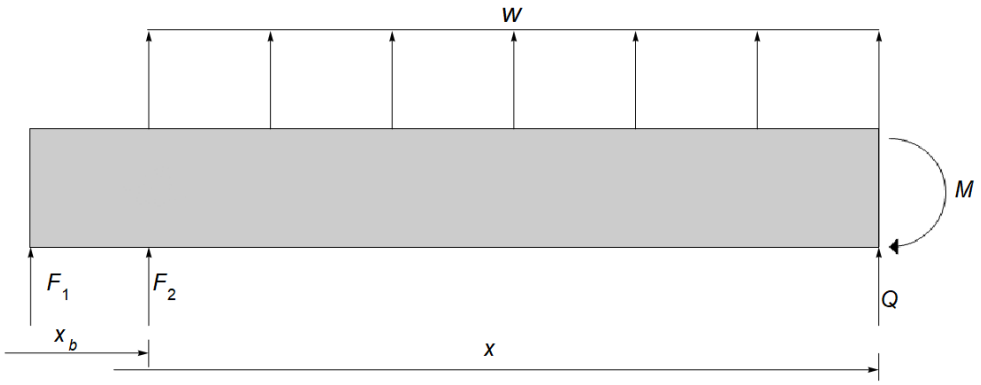

Figure 3.17: Schematic of the reactions on $x_b \leq x \leq x_c$.

From Figure 3.17, we obtain:

$$M = -\frac{w}{2}(x - x_b)^2 - F_2(x - x_b) - F_1(x - x_a) \quad (3.73)$$

$$Q = -w(x - x_b) - F_1 - F_2 \quad (3.74)$$

which simplifying comes:

$$M = -\frac{w}{2}(L - x)^2 \quad (3.75)$$

$$Q = w(L - x) \quad (3.76)$$

With all the equations describing the bending moment and shear force for all the segments of the beam calculated and simplified, we can assume an Euler-Bernoulli beam, with its curvature given by the following equation:

$$\frac{d^2y}{dx^2} = -\frac{M}{EI} \quad (3.33 \text{ revisited})$$

and obtain the rotation and deflection equations by integrating once and twice, respectively.

Using the equations obtained above, it is possible to draw a representation of the shear force and bending moment diagrams represented by Figure 3.18 and with its variation along the beam's length. In this case, the diagrams must be separated into two different diagrams due

to the existence of an overlapping section.

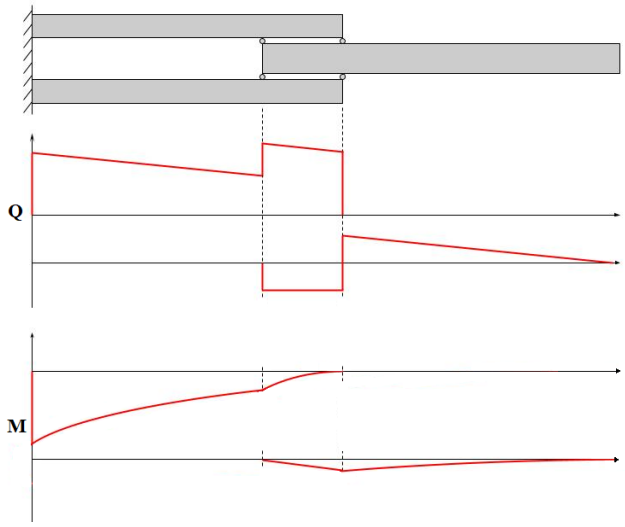

Figure 3.18: Shear Force and Bending Moment diagram representation of Case 2.

3.3.4 Rotation and Deflection with Euler-Bernoulli Theory

Obtaining the equations for the rotation and deflection of the beam for $0 \leq x < x_a$, $x_a \leq x < x_b$ and $x_b \leq x \leq x_c$, all the respective equations for the bending moment and shear force are substituted in equation 3.33 and integrated in x. To the following calculations, assumptions 3.9, 3.10, 3.11, 3.12 and 3.34 are applied, whenever it is appropriate to simplify calculations, and a new one is introduced:

$$\overline{x}_a = (1 - K_{L_2} - K_{L_0}) \quad (3.77)$$

- From root to point A : $0 \leq \overline{x} < (1 - K_{L_2} - K_{L_0})$:

$$\frac{d^2y}{dx^2} = \frac{w}{2EI_1}\left(x^2 - 2Lx + L^2\right) \quad (3.78)$$

$$\frac{dy}{dx} = \frac{w}{2EI_1}\left(\frac{x^3}{3} - Lx^2 + L^2x\right) + A_1 \quad (3.79)$$

$$y = \frac{w}{2EI_1}\left(\frac{x^4}{12} - \frac{Lx^3}{3} + \frac{L^2x^2}{2}\right) + A_1x + A_2 \quad (3.80)$$

To obtain the equations above, 3.63 was replaced in equation 3.33 and we get equation 3.78, which describes the curvature of the beam. Integrating once, equation 3.79 is obtained and describes the rotation of the beam, integrating twice we obtain equation 3.80 that describes the deflection of the beam. In order to calculate the value of A_1 and A_2, we again make use of the boundary conditions 2.6 and conclude that at $x = 0$, $\frac{dy}{dx} = 0$ and $y = 0$. Therefore $A_1 = 0$

and $A_2 = 0$, obtaining:

$$\frac{dy}{dx} = \frac{wL^3}{6EI_1}\left(3\overline{x} - 3\overline{x}^2 + \overline{x}^3\right) \quad (3.81)$$

$$y = \frac{wL^4}{24EI_1}\left(6\overline{x}^2 - 4\overline{x}^3 + \overline{x}^4\right) \quad (3.82)$$

Applying $\overline{x} = \overline{x}_a$ to equations 3.81 and 3.82 means that the equations now represent the rotation and deflection of the beam at the first point of discontinuity:

$$\left(\frac{dy}{dx}\right)_A = \frac{wL^3}{6EI_1}\left(3\overline{x}_a - 3\overline{x}_a^2 + \overline{x}_a^3\right) \quad (3.83)$$

$$(y)_A = \frac{wL^4}{24EI_1}\left(6\overline{x}_a^2 - 4\overline{x}_a^3 + \overline{x}_a^4\right) \quad (3.84)$$

- From point A to point B : $(1 - K_{L_2} - K_{L_0}) \leq \overline{x} < (1 - K_{L_2})$:

$$\frac{d^2y}{dx^2} = \frac{1}{EI_1}\left[\frac{w}{2}\left(L^2 - 2Lx + x^2\right) - F_1(x - x_a)\right] \quad (3.85)$$

$$\frac{dy}{dx} = \frac{1}{6EI_1}\left[w\left(3L^2x - 3Lx^2 + x^3\right) - F_1\left(3x^2 - 6xx_a\right)\right] + B_1 \quad (3.86)$$

$$y = \frac{1}{24EI_1}\left[w\left(6L^2x^2 - 4Lx^3 + x^4\right) - F_1\left(4x^3 - 12x^2x_a\right)\right] + B_1x + B_2 \quad (3.87)$$

As before, we applied the respective bending moment equation (3.69) to equation 3.33 and integrated in x to obtain the equation for the curvature (3.85), the equation for the rotation (3.86) and equation for the deflection (3.87).

Since point A is a discontinuity point, the values of rotation and deflection at that point from segment one ($0 \leq x < x_a$) are the same as the values of rotation and deflection at that same point on the following segment ($x_a \leq x < x_b$), hence the following boundary conditions appear:

$$\frac{dy}{dx} = \left(\frac{dy}{dx}\right)_A \text{ at } x = x_a \quad (3.88)$$

$$y = (y)_A \text{ at } x = x_a \quad (3.89)$$

In order to obtain the values of B_1 and B_2, we compute equations 3.86 and 3.87 with respect to B_1 and B_2, respectively, and use the boundary conditions above to substitute 3.88 in equation 3.86 and 3.89 in equation 3.87 to obtain:

$$B_1 = -\frac{wL^3}{4EI_1K_{L_0}}K_{L_2}^2(1 - K_{L_2} - K_{L0})^2 \quad (3.90)$$

$$B_2 = -\frac{wL^4}{12EI_1K_{L_0}}K_{L_2}^2(1 - K_{L_2} - K_{L0})^3 \quad (3.91)$$

With B_1 and B_2 calculated, we can replace their values in equations 3.86 and 3.87, with assumptions 3.12, 3.34 and 3.77 and simplify, in order to obtain the final equations regarding the rotation and deflection of the beam in $(1-K_{L_2}-K_{L_0}) \leq \overline{x} < (1-K_{L_2})$. This simplification leads to the following equations that only depend on EI_1, K_{L_2}, K_{L_0}, L and $\overline{x}$:

$$\begin{aligned}\frac{dy}{dx} = -\frac{wL^3}{12EI_1K_{L_0}}\Big[&3K_{L_2}^4 + 6K_{L_2}^3(K_{L_0}+\overline{x}-1) \\ &+ 3K_{L_2}^2(K_{L_0}+\overline{x}-1)^2 - 2K_{L_0}(3\overline{x}-3\overline{x}^2+\overline{x}^3)\Big]\end{aligned} \tag{3.92}$$

$$\begin{aligned}y = -\frac{wL^4}{24EI_1K_{L_0}}\Big[&2K_{L_2}^5 + 6K_{L_2}^4(K_{L_0}+\overline{x}-1) + 6K_{L_2}^3(K_{L_0}+\overline{x}-1)^2 \\ &+ 2K_{L_2}^2(K_{L_0}+\overline{x}-1)^3 - K_{L_0}(6\overline{x}^2-4\overline{x}^3+\overline{x}^4)\Big]\end{aligned} \tag{3.93}$$

Just like before, replacing $\overline{x} = \overline{x}_b$ gives the equation for the rotation and deflection for the second segment of the beam at the second discontinuity point, point B:

$$\begin{aligned}\left(\frac{dy}{dx}\right)_B = -\frac{wL^3}{12EI_1K_{L_0}}\Big[&3K_{L_2}^4 + 6K_{L_2}^3(K_{L_0}+\overline{x}_b-1) \\ &+ 3K_{L_2}^2(K_{L_0}+\overline{x}_b-1)^2 - 2K_{L_0}(3\overline{x}_b-3\overline{x}_b^2+\overline{x}_b^3)\Big]\end{aligned} \tag{3.94}$$

$$\begin{aligned}(y)_B = -\frac{wL^4}{24EI_1K_{L_0}}\Big[&2K_{L_2}^5 + 6K_{L_2}^4(K_{L_0}+\overline{x}_b-1) + 6K_{L_2}^3(K_{L_0}+\overline{x}_b-1)^2 \\ &+ 2K_{L_2}^2(K_{L_0}+\overline{x}_b-1)^3 - K_{L_0}(6\overline{x}_b^2-4\overline{x}_b^3+\overline{x}_b^4)\Big]\end{aligned} \tag{3.95}$$

- From point B to point C : $(1-K_{L_2}) \leq \overline{x} \leq 1$:

$$\frac{d^2y}{dx^2} = \frac{w}{2EI_2}\left(x^2-2Lx+L^2\right) \tag{3.96}$$

$$\frac{dy}{dx} = \frac{w}{2EI_2}\left(\frac{x^3}{3}-Lx^2+L^2x\right)+C_1 \tag{3.97}$$

$$y = \frac{w}{2EI_2}\left(\frac{x^4}{12}-\frac{Lx^3}{3}+\frac{L^2x^2}{2}\right)+C_1x+C_2 \tag{3.98}$$

For the final segment of the beam $(1-K_{L_2} \leq \overline{x} \leq 1)$, we apply the respective bending moment equation (3.75) in equation 3.33 and integrate in x to obtain the equation that describes the curvature (3.96), the equation that describes the rotation (3.97) and the equation that describes the deflection of the beam (3.98).

Just like the previous discontinuity point, at point B the value of the rotation and deflection of the first beam segment must be the same as the value of the rotation and deflection, at that same point, on the second segment. For that to verify, the following boundary conditions

must apply:

$$\frac{dy}{dx} = \left(\frac{dy}{dx}\right)_B \text{ at } x = x_b \quad (3.99)$$

$$y = (y)_B \text{ at } x = x_b \quad (3.100)$$

Substituting 3.99 in equation 3.97 and 3.100 in equation 3.98, and computing with respect to C_1 and C_2, we are able to obtain the values of those constants:

$$C_1 = -\frac{wL^3}{12EI_1K_{EI}}\left(2 - 2K_{L_2}^3 - 2K_{EI} + 2K_{L_2}^3K_{EI} + 3K_{L_2}^2K_{L_0}K_{EI}\right) \quad (3.101)$$

$$\begin{aligned} C_2 = -\frac{wL^4}{24EI_1K_{EI}}(&-1 + 4K_{L_2}^3 - 3K_{L_2}^4 + K_{EI} - 4K_{L_2}^3K_{EI} + 3K_{L_2}^4K_{EI} \\ &- 6K_{L_2}^2K_{L_0}K_{EI} + 6K_{L_2}^3K_{L_0}K_{EI} + 2K_{L_2}^2K_{L_0}^2K_{EI}) \end{aligned} \quad (3.102)$$

Replacing C_1 (3.101) in equation 3.97 and C_2 (3.102) in equation 3.98,with assumptions 3.12, 3.34 and 3.77, we obtain the final equations for the rotation and deflection of the beam, for $(1 - K_{L_2}) \leq \overline{x} \leq 1$. Simplifying, we get the following, that only depend on EI_1, K_{EI}, K_{L_2}, K_{L_0}, L and $\overline{x}$:

$$\frac{dy}{dx} = -\frac{wL^3}{12EI_1K_{EI}}\Big\{2K_{L_2}^3(K_{EI} - 1) + 3K_{L_2}^2K_{L_0}K_{EI} - 2\big[K_{EI} + (\overline{x} - 1)^3\big]\Big\} \quad (3.103)$$

$$\begin{aligned} y = -\frac{wL^4}{24EI_1K_{EI}}\Big\{&3K_{L_2}^4(K_{EI} - 1) + K_{EI} - (\overline{x} - 1)^4 - 4K_{EI}\overline{x} \\ &+ 2K_{L_2}^2K_{L_0}K_{EI}(-3 + K_{L_0} + 3\overline{x}) + K_{L_2}^3\big[4 - 4\overline{x} + K_{EI}(-4 + 6K_{L_0} + 4\overline{x})\big]\Big\} \end{aligned} \quad (3.104)$$

After obtaining the final calculations, we conclude that the equations that describe the rotation and the deflection of the beam are, for $0 \leq \overline{x} < (1 - K_{L_2} - K_{L_0})$ equations 3.81 and 3.82, for $(1 - K_{L_2} - K_{L_0}) \leq \overline{x} < (1 - K_{L_2})$ equations 3.92 and 3.93 and for $(1 - K_{L_2}) \leq \overline{x} \leq 1$ equations 3.103 and 3.104, respectively.

By substituting $\overline{x} = 1$, which is equivalent to having $x = L$, in the last two equations (3.103 and 3.104), we obtain the equations regarding the rotation and deflection at the tip of the beam:

$$\left(\frac{dy}{dx}\right)_L = -\frac{wL^3}{12EI_1K_{EI}}\big[2K_{L_2}^3(K_{EI} - 1) - 2K_{EI} + 3K_{L_2}^2K_{L_0}K_{EI}\big] \quad (3.105)$$

$$(y)_L = -\frac{wL^4}{24EI_1K_{EI}}\left[3K_{L_2}^4(K_{EI}-1) - 3K_{EI} + 6K_{L_2}^3K_{L_0}K_{EI} + 2K_{L_2}^2K_{L_0}^2K_{EI}\right] \tag{3.106}$$

Equations 3.107 and 3.108 represent the ratio between the beam's rotation and deflection and the rotation and deflection equations for a uniform beam, at $x = L$:

$$\frac{\left(\frac{dy}{dx}\right)_L}{\left(\frac{dy}{dx}\right)_U} = 1 - \frac{3K_{L_2}^2K_{L_0}}{2} + K_{L_2}^3\left(\frac{1}{KEI} - 1\right) \tag{3.107}$$

$$\frac{(y)_L}{(y)_U} = 1 - 2K_{L_2}^3K_{L_0} - \frac{2K_{L_2}^2K_{L_0}^2}{3} + K_{L_2}^4\left(\frac{1}{K_{EI}} - 1\right) \tag{3.108}$$

Plotting these equations gives us notion of how the rotation and deflection change for the second case beam, visible in 5.2.

3.4 Case 3 - Overhanging telescopic beam with continuous contact

Case 3 differs from the second one by having constant contact between the root and tip parts on the overlapping segment, instead of having defined contact points. The tip segment slides freely in the longitudinal direction inside the root segment. Assumptions 3.2, 3.3 and 3.4 are used to analyze this case.

Figure 3.19 represents the configuration of the telescopic mechanism of Case 3, with a applied uniformly distributed load w and a new load appears, j, which is distributed along the neutral axis, on the overlapping segment caused by the continuous contact, which is better explained later in this section.

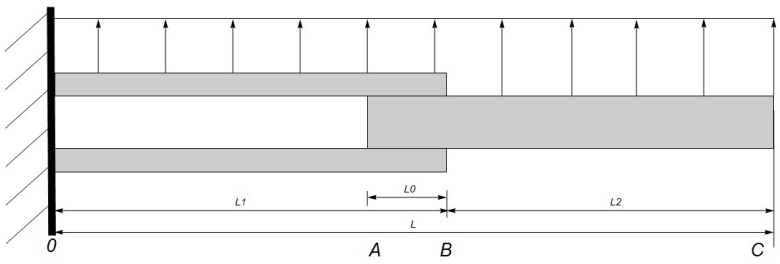

Figure 3.19: Telescopic beam schematic for Case 3.

3.4.1 Reactions

Assuming that EI_1 and EI_2 are the flexural rigidities of the root and tip segments, respectively, and L the total length of the beam such that $L = L_1 + L_2$, it is defined for the free body diagram that the y axis is positive pointing upwards, the x axis is positive pointing to the right and moment is positive in the counter-clockwise direction.

It is assumed that we deal with small deflections and the plane's cross-sections remain perpendicular to the x axis after the deformation. Assuming 3.9, 3.10 and 3.11, the following diagram is obtained:

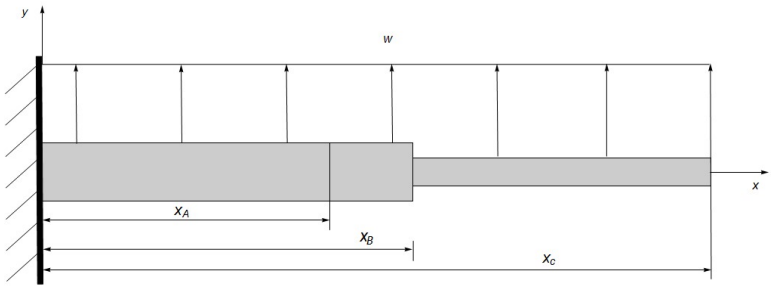

Figure 3.20: Case 3 diagram.

and we proceed to calculate the reactions at $x = 0$ (Fig. 3.21) in order to obtain the equations for the bending moment and shear force:

$$M_0 = -\frac{wL^2}{2} \quad (3.109)$$

$$Q_0 = -wL \quad (3.110)$$

Figure 3.22 represents the beam with its reactions and the distributed load j applied, as stated above. This distributed load starts decreasing from point x_a until its minimum value when it crosses the segment's neutral axis and increases again until the end of the overlapping segment at point x_b.

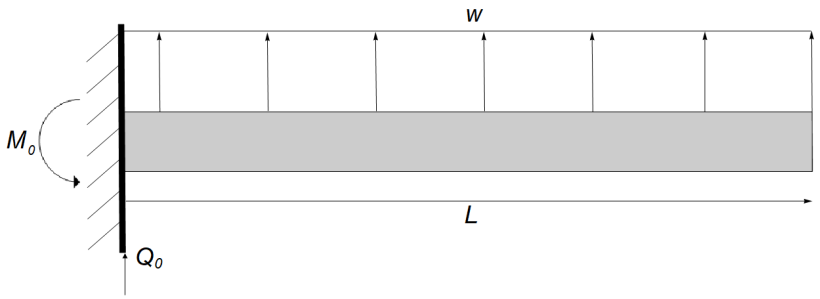

Figure 3.21: Reactions on the beam at $x = 0$.

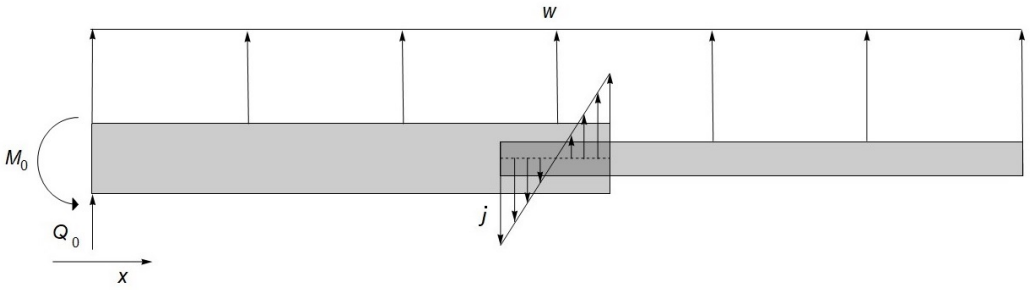

Figure 3.22: Reactions on the beam with load j applied.

3.4.2 Load at Interface

To calculate the resulting distributed load j at the overlapping segment (Fig. 3.22) the calculations are performed only on the tip segment. Thus, the bending moment is calculated at the point where load j stops, point x_b and the load w is only applied on the outside part of the tip segment, i.e., only distributed in $x_c - x_b$. Figure 3.23 represents the schematic used to calculate the load.

Since it is unknown how the distribution of load j is acting on the beam, we calculate its slope using two known points of the load, which are denoted as j_1 and j_2 (Fig. 3.23). Since $j(x_a) = j_1$, the following equation is obtained:

$$j(x) = \frac{j_2 - j_1}{x_b - x_a}(x - x_a) + j_1 \quad (3.111)$$

If we write equation 3.111 as:

$$j(x) = \left(j_1 - \frac{j_2 x_a}{x_b - x_a} + \frac{j_1 x_a}{x_b - x_a}\right) + \left(\frac{j_2}{x_b - x_a} - \frac{j_1}{x_b - x_a}\right) x \quad (3.112)$$

it is easier to solve $\Sigma F = 0$ (eq. 3.113) and $\Sigma M = 0$ (eq. 3.114) and integrate to obtain the shear force equation and integrating the product of $j(x)$ with the moment arm, to obtain the bending moment equation caused by load j, around point $x = x_a$. For the calculations to be simplified, j is calculated as pointing upwards and later, with j_1 and j_2 obtained, the directions of the load are corrected depending on their respective signal, as seen in Figure 3.23.

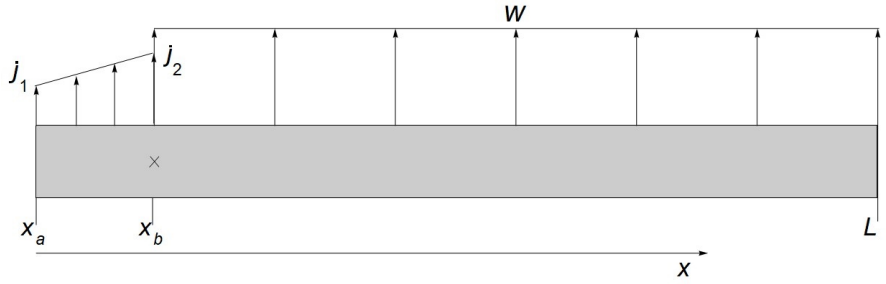

Figure 3.23: Reactions on the tip part of the beam used to calculate J.

$$\Sigma F = 0 \Leftrightarrow \int_{x_a}^{x_a+L_0} j(x)\,dx + \int_{x_a+L_0}^{L} w\,dx = 0 \quad (3.113)$$

$$\Sigma M = 0 \Leftrightarrow \int_{x_a}^{x_a+L_0} j(x)(x - x_a - L_0)\,dx + \int_{x_a+L_0}^{L} w(x - x_a - L_0)\,dx = 0 \quad (3.114)$$

Solving a system of equations with the two above, it is possible to obtain the values of j_1 and

j_2:

$$j_1 = \frac{w\left(3L^2 - 4L_0L - 6Lx_a + L_0^2 + 4L_0x_a + 3x_a^2\right)}{L_0^2} \quad (3.115)$$

$$j_2 = -\frac{w(L - L_0 - x_a)\left[-3L(L_0 + 2x_a - 2x_b) + L_0^2 + 3L_0x_a + 6x_a(x_a - x_b)\right]}{L_0^3} \quad (3.116)$$

Substituting 3.115 and 3.116 in equation 3.112 and using $x_a = L - L_2 - L_0$, the equation that defines load j on the tip segment is obtained:

$$j(x) = wL_2\left[\left(\frac{-4L_0^2 + 6L(L_0 + L_2) - 6L_2^2 - 9L_0L_2}{L_0^3}\right) - \left(\frac{6(L_0 + L_2)}{L_0^3}\right)x\right] \quad (3.117)$$

The symmetrical of the previous equation ($-j$) gives us the equation for this load on the root segment and it is hereunder denominated as $r = -j$, which describes the configuration expected and represented in Figure 3.22.

3.4.3 Bending moment and shear force equations

Following the rule of sign of bending moments by defining the bending moment as positive in the clockwise direction, the equations for bending moment and shear force are obtained by solving the sum of all moments and all forces equal to zero, $\Sigma M = 0$ and $\Sigma F = 0$ respectively.

Referring to Fig. 3.24 the equations are, for $0 \leq x < x_a$, the following:

$$M = M_0 - Q_0x - \frac{w}{2}x^2 \quad (3.118)$$

$$Q = -wx - Q_0 \quad (3.119)$$

Replacing 3.109 and 3.110 in equations 3.118 and 3.119 we obtain the following simplified equations:

$$M = -\frac{w}{2}(L - x)^2 \quad (3.120)$$

$$Q = w(L - x) \quad (3.121)$$

and at $x = x_a$:

$$M_A = -\frac{w}{2}(L - x_a)^2 \quad (3.122)$$

$$Q_A = w(L - x_a) \quad (3.123)$$

Figure 3.25 represents the reactions on the beam for $x_a \leq x < x_b$ on the root segment, where load r is now applied:

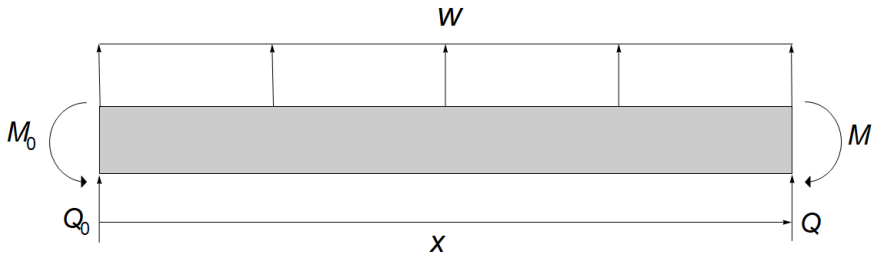

Figure 3.24: Reactions on the beam at $0 \leq x < x_a$.

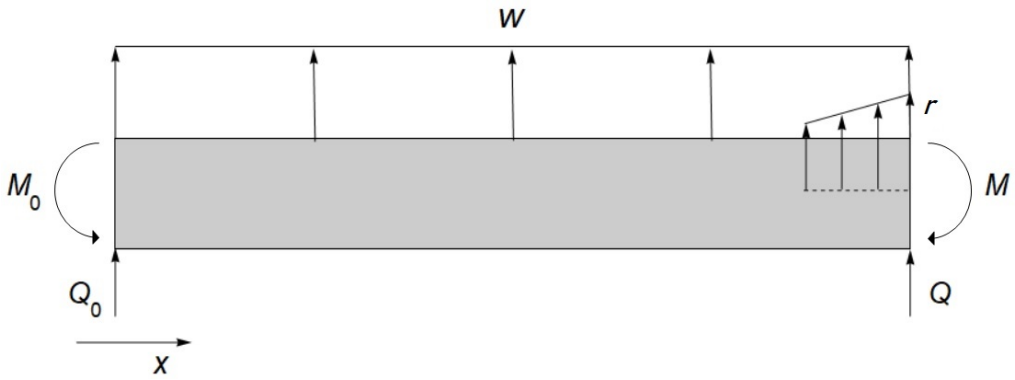

Figure 3.25: Reactions on the beam at $x_a \leq x < x_b$.

For this segment, it is necessary to take into account load r and how it is applied. In order to obtain the equations, we need to integrate r in its interval of application. However, variable x cannot be used to integrate, so as not to conflict with its use as a coordinate. For that matter, u is used as a local integration variable. Hence, the bending moment due to r is described by:

$$\int_{x_a}^{x_a+L_0} r(u)(x-u)\,du, \quad \forall u \in [x_a, x_a+L_0]$$

and the bending moment and shear force equations for $x_a \leq x < x_b$ are:

$$M = M_0 - Q_0 x - \frac{w}{2}x^2 - \int_{x_a}^{x} r(u)(x-u)\,du, \quad \forall u \in [x_a, x_b] \tag{3.124}$$

$$Q = -Q_0 - wx - \int_{x_a}^{x} r(x)\,dx \tag{3.125}$$

which simplifying with 3.109, 3.110 and 3.117 comes:

$$M = -\frac{w}{2L_0^3}\left\{(L_0+L_2)(-L+L_2+x)^2\Big[L_0^2+3L_0L_2+2L_2(-L+L_2+x)\Big]\right\} \tag{3.126}$$

$$\begin{aligned} Q = \frac{w}{L_0^3}\Big\{ & L_0^3L - L_0^3x - L_2(-L+L_0+L_2+x)\Big[L_0^2 - 3L(L_0+L_2) \\ & + 3L_0(L_2+x) + 3L_2(L_2+x)\Big]\Big\} \end{aligned} \tag{3.127}$$

and $x = x_b$:

$$M_B = -\frac{w}{2L_0^3}\left\{(L_0+L_2)(-L+L_2+x_b)^2\left[L_0^2+3L_0L_2+2L_2(-L+L_2+x_b)\right]\right\} \quad (3.128)$$

$$Q_B = 0 \quad (3.129)$$

In the same segment, $x_a \leq x < x_b$, but for the tip part, the equations for the shear force and bending moment are obtained from integrating load j's equation:

$$M = \frac{L_2 w(-L+L_0+L_2+x)^2(-2L(L_0+L_2)+2L_2(L_2+x)+L_0(L_2+2x))}{2L_0^3} \quad (3.130)$$

$$Q = \frac{L_2 w(-L+L_0+L_2+x)(L_0^2-3L(L_0+L_2)+3L_0(L_2+x)+3L_2(L_2+x))}{L_0^3} \quad (3.131)$$

For the final segment, in $x_b \leq x \leq x_c$, the load j is now applied in the opposite direction of the previous segment, as it is only reacting on the tip segment, visible in Figure 3.26: By

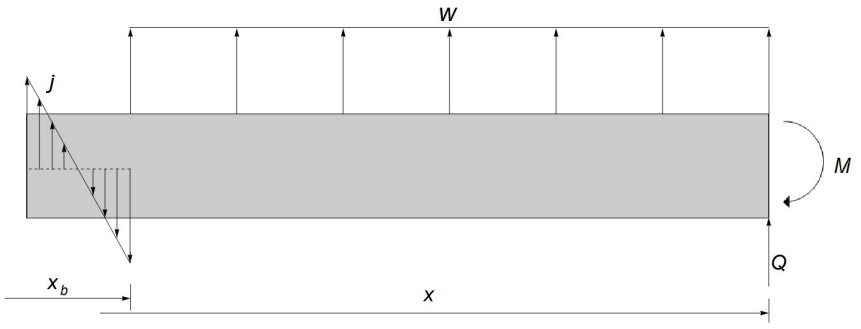

Figure 3.26: Reactions on the beam at $x_b \leq x \leq x_c$.

integrating the product between load j and the moment arm, the equation for the moment caused by the load is obtained. It must be integrated in the interval of values on which the load is applied. Thus obtaining the bending moment and shear force equations:

$$M = -\frac{w}{2}(x-x_b)^2 - \int_{x_a}^{x_a+L_0} j(u)(x-u)\,du, \quad \forall u \in [x_a, xa+L_0] \quad (3.132)$$

$$Q = -w(x-x_b) - \int_{x_a}^{x_a+L_0} j(x)\,dx \quad (3.133)$$

which simplifying comes:

$$M = -\frac{w}{2}(L-x)^2 \quad (3.134)$$

$$Q = w(L-x) \quad (3.135)$$

With all the equations that describe the bending moment and shear force for the three segments of the beam calculated and simplified, we can assume an Euler-Bernoulli beam, with

its curvature given by the following equation:

$$\frac{d^2y}{dx^2} = -\frac{M}{EI} \quad \text{(3.33 revisited)}$$

and obtain the rotation and deflection equations by integrating once and twice, respectively.

Using the equations obtained above, it is possible to draw a representation of the shear force and bending moment diagrams represented by Figure 3.27 and with its variation along the beam's length. In this case, the diagrams must be separated into two different diagrams due to the existence of an overlapping section.

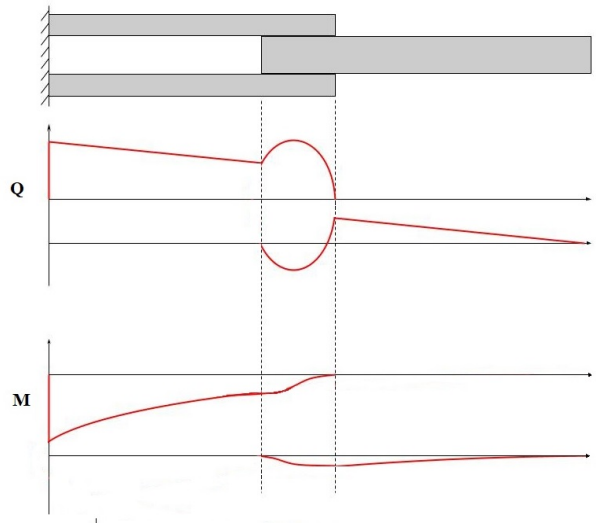

Figure 3.27: Shear Force and Bending Moment diagram representation of Case 3.

3.4.4 Rotation and Deflection with Euler-Bernoulli Theory

After obtaining the equations for the rotation and deflection of the beam for $0 \leq x < x_a$, $x_a \leq x < x_b$ and $x_b \leq x \leq x_c$, all the respective equations for the bending moment and shear force are substituted in equation 3.33 and integrated in x. To the following calculations, assumptions 3.9, 3.10, 3.11, 3.12, 3.34 and 3.77 are applied, whenever it is appropriate, to simplify calculations.

For the interval $0 \leq \overline{x} < (1 - K_{L_2} - K_{L_0})$, the procedure to obtain the equations for the rotation and deflection is the same as for Case 2. These equations are:

$$\frac{dy}{dx} = \frac{wL^3}{6EI_1}\left(3\overline{x} - 3\overline{x}^2 + \overline{x}^3\right) \quad (3.136)$$

$$y = \frac{wL^4}{24EI_1}\left(6\overline{x}^2 - 4\overline{x}^3 + \overline{x}^4\right) \quad (3.137)$$

Applying $\overline{x} = \overline{x}_a$ to equations 3.136 and 3.137 means that the equations now represent the

rotation and deflection of the beam at the first point of discontinuity:

$$\left(\frac{dy}{dx}\right)_A = \frac{wL^3}{6EI_1}\left(3\overline{x}_a - 3\overline{x}_a^2 + \overline{x}_a^3\right) \quad (3.138)$$

$$(y)_A = \frac{wL^4}{24EI_1}\left(6\overline{x}_a^2 - 4\overline{x}_a^3 + \overline{x}_a^4\right) \quad (3.139)$$

- From point A to point B : $(1 - K_{L_2} - K_{L_0}) \leq \overline{x} < (1 - K_{L_2})$:

$$\frac{d^2y}{dx^2} = \frac{w}{2EI_1}\left\{\frac{(L_0 + L_2)(-L + L_2 + x)^2\Big[L_0^2 + 3L_0L_2 + 2L_2(-L + L_2 + x)\Big]}{L_0^3}\right\} \quad (3.140)$$

$$\begin{aligned}\frac{dy}{dx} = \frac{w}{12EI_1L_0^3}\Big\{&(L_0 + L_2)x\big[-6(L - L_2)^2\big[-L_0^2 - 3L_0L_2 + 2(L - L_2)L_2\big]\\ &+ 6\big[3L^2L_2 + L_2(L_0^2 + 3L_0L_2 + 3L_2^2) - L(L_0^2 + 3L_0L_2 + 6L_2^2)\big]x\\ &+ 2\big[L_0^2 + 3L0L2 + 6L2(-L + L2)\big]x^2 + 3L_2x^3\big]\Big\} + B_1\end{aligned} \quad (3.141)$$

$$\begin{aligned}y = \frac{w}{12EI_1L_0^3}\Big\{&(L_0 + L_2)(-3(L - L_2)^2\big[-L_0^2 - 3L_0L_2 + 2(L - L_2)L_2\big]x^2\\ &+ 2\big[3L^2L_2 + L_2(L_0^2 + 3L_0L_2 + 3L_2^2) - L(L_0^2 + 3L_0L_2 + 6L_2^2\big]x^3\\ &+ \frac{1}{2}\big[L_0^2 + 3L_0L_2 + 6L_2(-L + L_2)\big]x^4 + \frac{3L_2x^5}{5}\Big\} + B_1x + B_2\end{aligned} \quad (3.142)$$

As before, the respective bending moment equation (3.126) is applied to equation 3.33 and integrated in x to obtain the equation for the curvature (3.140), the equation for the rotation (3.141) and equation for the deflection (3.142).

Since point A is a discontinuity point, the values of rotation and deflection at that point from segment one ($0 \leq x < x_a$) are the same as the values of rotation and deflection at that same point on the following segment ($x_a \leq x < x_b$), hence the following boundary conditions:

$$\frac{dy}{dx} = \left(\frac{dy}{dx}\right)_A \text{ at } x = x_a \quad (3.143)$$

$$y = (y)_A \text{ at } x = x_a \quad (3.144)$$

To obtain the values of B_1 and B_2, we compute equations 3.141 and 3.138 in 3.143 and equations 3.142 and 3.139 in 3.144, thus:

$$B_1 = -\frac{wL^3}{12EI_1K_{L_0}^3}\Big\{K_{L_2}(-1 + K_{L_0} + K_{L_2})^3\big[3K_{L_0} + K_{L_0}^2 - 3(-1 + K_{L_2})K_{L_2}\big]\Big\} \quad (3.145)$$

$$B_2 = -\frac{wL^4}{120EI_1K_{L_0}^3}\Big\{K_{L_2}(-1+K_{L_0}+K_{L_2})^4\big[4K_{L_0}^2-6(-1+K_{L_2})K_{L_2} + 3K_{L_0}(2+K_{L_2})\big]\Big\} \tag{3.146}$$

Having B_1 and B_2 calculated, it is possible to substitute their values in equations 3.141 and 3.142, assuming 3.12 and 3.77, and simplifying in order to obtain the final equations regarding the rotation and deflection of the beam in $(1-K_{L_2}-K_{L_0}) \leq \overline{x} < (1-K_{L_2})$. This simplification leads to the following equations that only depend on EI_1, K_{L_2}, K_{L_0}, L and $\overline{x}$:

$$\begin{aligned}\frac{dy}{dx} = \frac{wL^3}{12EI_1K_{L_0}^3}\Big\{&(-K_{L_0}^5K_{L_2}-3K_{L-0}^4K_{L_2}^2+8K_{L_0}^2K_{L_2}(-1+K_{L_2}+\overline{x})^3\\ &+3K_{L_2}^2(-1+K_{L_2}+\overline{x})^4+3K_{L_0}K_{L_2}(-1+K_{L_2}+\overline{x})^3(-1+3K_{L_2}+\overline{x})\\ &+2KL_0{}^3\big[3K_{L_2}^2(-1+\overline{x})+3K_{L_2}(-1+\overline{x})^2+\overline{x}(3-3\overline{x}+\overline{x}^2)\big]\Big\}\end{aligned} \tag{3.147}$$

$$\begin{aligned}y = -\frac{wL^4}{120EI_1K_{L_0}^3}\Big\{&4K_{L_0}^6K_{L_2}+K_{L_0}^5K_{L_2}\big[19K_{L_2}+10(-1+\overline{x})\big]\\ &+30K_{L_0}^4K_{L_2}^2(-1+K_{L_2}+\overline{x})\\ &-20K_{L_0}^2K_{L_2}(-1+K_{L_2}+\overline{x})^4-6K_{L_2}^2(-1+K_{L_2}+\overline{x})^5\\ &-3K_{L_0}K_{L_2}(-1+K_{L_2}+\overline{x})^4(-2+7K_{L_2}+2\overline{x})\\ &+5K_{L_0}^3\big[2K_{L_2}^4-6K_{L_2}^2(-1+\overline{x})^2-4K_{L_2}(-1+\overline{x})^3-\overline{x}^2(6-4\overline{x}+\overline{x}^2)\big]\Big\}\end{aligned} \tag{3.148}$$

Replacing $\overline{x} = \overline{x}_b$ gives the rotation and deflection equations for the overlapping segment of the beam, at the second discontinuity point:

$$\begin{aligned}\frac{dy}{dx} = \frac{wL^3}{12EI_1K_{L_0}^3}\Big\{&(-K_{L_0}^5K_{L_2}-3K_{L_0}^4K_{L_2}^2+8K_{L_0}^2K_{L_2}(-1+K_{L_2}+\overline{x}_b)^3\\ &+3K_{L_2}^2(-1+K_{L_2}+\overline{x}_b)^4+3K_{L_0}K_{L_2}(-1+K_{L_2}+\overline{x}_b)^3(-1+3K_{L_2}+\overline{x}_b)\\ &+2KL_0{}^3\big[3K_{L_2}^2(-1+\overline{x}_b)+3K_{L_2}(-1+\overline{x}_b)^2+\overline{x}_b(3-3\overline{x}_b+\overline{x}_b^2)\big]\Big\}\end{aligned} \tag{3.149}$$

$$\begin{aligned}y = -\frac{wL^4}{120EI_1K_{L_0}^3}\Big\{&4K_{L_0}^6K_{L_2}+K_{L_0}^5K_{L_2}\big[19K_{L_2}+10(-1+\overline{x}_b)\big]\\ &+30K_{L_0}^4K_{L_2}^2(-1+K_{L_2}+\overline{x}_b)\\ &-20K_{L_0}^2K_{L_2}(-1+K_{L_2}+\overline{x}_b)^4-6K_{L_2}^2(-1+K_{L_2}+\overline{x}_b)^5\\ &-3K_{L_0}K_{L_2}(-1+K_{L_2}+\overline{x}_b)^4(-2+7K_{L_2}+2\overline{x}_b)\\ &+5K_{L_0}^3\big[2K_{L_2}^4-6K_{L_2}^2(-1+\overline{x}_b)^2-4K_{L_2}(-1+\overline{x}_b)^3-\overline{x}_b^2(6-4\overline{x}_b+\overline{x}_b^2)\big]\Big\}\end{aligned} \tag{3.150}$$

- From point B to point C : $(1-K_{L_2}) \leq \overline{x} \leq 1$:

$$\frac{d^2y}{dx^2} = \frac{w}{2EI_2}\left(x^2 - 2Lx + L^2\right) \tag{3.151}$$

$$\frac{dy}{dx} = \frac{w}{2EI_2}\left(\frac{x^3}{3} - Lx^2 + L^2x\right) + C_1 \tag{3.152}$$

$$y = \frac{w}{2EI_2}\left(\frac{x^4}{12} - \frac{Lx^3}{3} + \frac{L^2x^2}{2}\right) + C_1x + C_2 \tag{3.153}$$

For the final segment of the beam $(1-K_{L_2} \leq \overline{x} \leq 1)$, we apply the respective bending moment equation (3.134) in equation 3.33 and integrate in x to obtain the equation that describes the curvature (3.151), the equation that describes the rotation (3.152) and the equation that describes the deflection of the beam(3.153).

Similarly to the previous discontinuity point, at point B the value of the rotation and deflection of the root beam segment must be the same as the value of the rotation and deflection, at that same point, on the tip segment. For that to verify, the following boundary conditions must apply:

$$\frac{dy}{dx} = \left(\frac{dy}{dx}\right)_B \text{ at } x = x_b \tag{3.154}$$

$$y = (y)_B \text{ at } x = x_b \tag{3.155}$$

Replacing 3.154 in equation 3.152 and 3.155 in equation 3.153 and computing with respect to C_1 and C_2, it is possible to obtain the respective values of those constants:

$$C_1 = -\frac{wL^3}{12EI_1K_{EI}}\left[2 + 2K_{L_2}^3(-1 + K_{EI}) - 2K_{EI} + K_{L_0}^2K_{L_2}K_{EI} + 3K_{L_0}K_{L_2}^2K_{EI}\right] \tag{3.156}$$

$$\begin{aligned} C_2 = -\frac{wL^4}{120EI_1K_{EI}}\Big\{&5(-1 + K_{EI}) + 15K_{L_2}^4(-1 + K_{EI}) \\ &+ 2K_{L_0}^2(-5 + 2K_{L_0})K_{L_2}K_{EI} \\ &+ K_{L_0}(-30 + 19K_{L_0})K_{L_2}^2K_{EI} + 10K_{L_2}^3\left[2 + (-2 + 3K_{L_0})K_{EI}\right]\Big\} \end{aligned} \tag{3.157}$$

Substituting 3.156 in equation 3.152 and 3.157 in equation3.153 and assuming 3.12, 3.34 and 3.77, the final equations that describe the rotation and deflection of the beam, for $(1-K_{L_2}) \leq \overline{x} \leq 1$, are obtained. Simplifying, we get the following equations, that only depend on EI_1, K_{EI}, K_{L_2}, K_{L_0}, L and $\overline{x}$:

$$\begin{aligned} \frac{dy}{dx} = -\frac{wL^3}{12EI_1K_{EI}}\Big\{&2K_{L_2}^3(-1 + K_{EI}) + K_{L_0}^2K_{L_2}K_{EI} + 3K_{L_0}K_{L_2}^2K_{EI} \\ &- 2\left[K_{EI} + (-1 + \overline{x})^3\right]\Big\} \end{aligned} \tag{3.158}$$

$$
\begin{aligned}
y = -\frac{wL^4}{120EI_1K_{EI}}\Big\{&15K_{L_2}^4(-1+K_{EI}) + K_{L_0}K_{L_2}^2K_{EI}\big[19K_{L_0} + 30(-1+\overline{x})\big] \\
&+ 2K_{L_0}^2K_{L_2}K_{EI}(-5+2K_{L_0}+5\overline{x}) + 10K_{L_2}^3\big[2-2\overline{x} \\
&+ K_{EI}(-2+3K_{L_0}+2\overline{x})\big] - 5\big[(-1+\overline{x})^4 + K_{EI}(-1+4\overline{x})\big]\Big\}
\end{aligned} \tag{3.159}
$$

After performing the final calculations, we conclude that the equations that describe the rotation and the deflection of the beam are, for $0 \leq \overline{x} < (1 - K_{L_2} - K_{L_0})$ equations 3.136 and 3.137, for $(1-K_{L_2}-K_{L_0}) \leq \overline{x} < (1-K_{L_2})$ equations 3.147 and 3.148 and for $(1-K_{L_2}) \leq \overline{x} \leq 1$ equations 3.158 and 3.159, respectively.

By substituting $\overline{x} = 1$, which is equivalent to having $x = L$, in the two equations above (3.158 and 3.159), we obtain the equations regarding the rotation and deflection at the tip of the beam:

$$
\begin{aligned}
\left(\frac{dy}{dx}\right)_L = -\frac{wL^3}{12EI_1K_{EI}}\big[&2K_{L_2}^3(-1+K_{EI}) - 2K_{EI} + K_{L_0}^2K_{L_2}K_{EI} \\
&+ 3K_{L_0}K_{L_2}^2K_{EI}\big]
\end{aligned} \tag{3.160}
$$

$$
\begin{aligned}
(y)_L = -\frac{wL^4}{120EI_1K_{EI}}\big[&15K_{L_2}^4(-1+K_{EI}) - 15K_{EI} + 4K_{L_0}^3K_{L_2}K_{EI} \\
&+ 19K_{L_0}^2K_{L_2}^2K_{EI} + 30K_{L_0}K_{L_2}^3K_{EI}\big]
\end{aligned} \tag{3.161}
$$

Equations 3.162 and 3.163 represent the ratio between the beam's rotation and deflection and the rotation and deflection equations for a uniform beam, at $x = L$:

$$
\frac{\left(\frac{dy}{dx}\right)_L}{\left(\frac{dy}{dx}\right)_U} = 1 - \frac{K_{L_0}^2K_{L_2}}{2} - \frac{3K_{L_0}K_{L_2}^2}{2} + K_{L_2}^3\left(-1+\frac{1}{K_{EI}}\right) \tag{3.162}
$$

$$
\frac{(y)_L}{(y)_U} = 1 - \frac{4K_{L_0}^3K_{L_2}}{15} - \frac{19K_{L_0}^2K_{L_2}^2}{15} - 2K_{L_0}K_{L_2}^3 + K_{L_2}^4\left(-1+\frac{1}{K_{EI}}\right) \tag{3.163}
$$

With all three cases studied and their respective equations for the displacements obtained, the numerical analysis will proceed. In Chapter 5, the results are presented as well as the plots of all the equations obtained in this chapter.

Chapter 4

Numerical Analysis of Compound Beams

In the previous chapter, the analytical analysis of the beams was finished and, after understanding what a numerical analysis is and how to approach a certain problem, it is time to apply it to this study and see if the results are in accordance with the analytic results. In order to obtain the Finite Element Analysis (FEA) for the three cases, we make use of the computational software for engineering simulation ANSYS.

As it was stated in 2.5, after the problem is identified, and before the analysis itself, some questions need to be addressed in order to obtain an accurate structural model. We know this is a problem of static nature and the most important physical phenomena is the deflection of the structure i.e., directional deformation. We also know that the main goal is to achieve deflection values that are consistent with the analytical ones. With this in mind, it is possible to start building the structural model, which is done with ANSYS's 3D modeling tool *SpaceClaim* [26].

Because this is a structural analysis, it is not possible to obtain results with non-dimensionalized properties in the same way as in Chapter 3, so certain values were attributed to some properties that were previously not needed to obtain results. These mechanical properties are w, E, I and L.

The values given which are common to all three cases are $w = 1000N/m$ and $L = 1000mm$. The remaining parameters depend on the different studied cases and will be explained in the respective section.

4.1 Case 1

With Case 1 being the easiest to analyze, the geometry is rather simple. This being said, a uniform beam was built and split in two different bodies, which represent the two different segments. Making the cross-sections of both bodies the same, it is possible to control the flexural rigidity ratio by changing the Young's modulus of the tip segment. Figure 4.1 shows the structural model built in *SpaceClaim* [26].

This model is then uploaded to ANSYS's workbench where we proceed with the analysis. The next step is the discretization of the beam's domain, which is the construction of a mesh composed of finite elements and nodes using a method defined by the user, in this case the Tetrahedron's method with computer controlled element order, which can be seen in Figure

4.2.

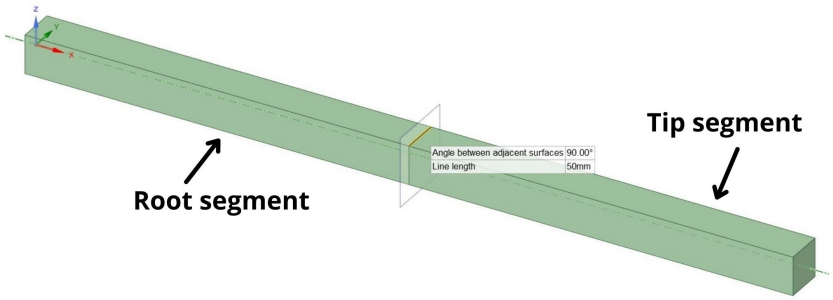

Figure 4.1: Structural model for Case 1 with visible mid-plane (trimetric view).

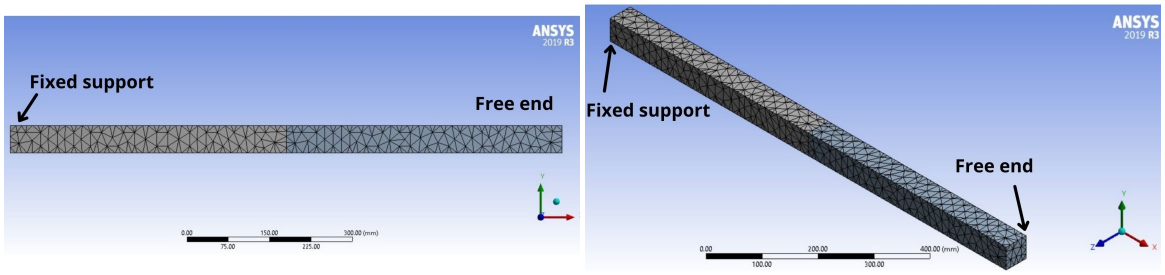

(a) Mesh (side view). (b) Mesh (isometric view).

Figure 4.2: Case 1 Tetrahedron method mesh.

After the mesh is created and refined, the boundary conditions, physical properties of the materials and loads acting on the structure are defined. These are the fixed support of the root segment, which allows no movement in any direction whatsoever, the applied load on the top faces of the beam, a *Bonded* contact between the two segments and the materials that compose the beam.

In order to obtain the results, a solution must be defined and in this case, to analyze the deflection, a solution for directional deformation is applied in the Y direction. The results for this deformation are presented in Chapter 6.

4.2 Case 2

Similarly to the previous case, it is necessary to build a structural model for this second beam case. This was achieved by building three bodies, just as seen in Figure 4.3, where one simulates the root segment and the other two act just the same way as if they were only one body. This is necessary in order to accurately apply the load w to the tip segment.

This time, since the cross-sections are no longer equal to one another, it is required that some calculations are performed in order to obtain the value of I for both segments and from that it is possible to obtain the value of E for the tip segment and control the value of K_{EI}. Note that the root segment has a hollow squared cross-section and the tip segment is a solid body with a solid squared cross-section (see 6.2). The values of K_{L_2} and K_{L_0} were also chosen.

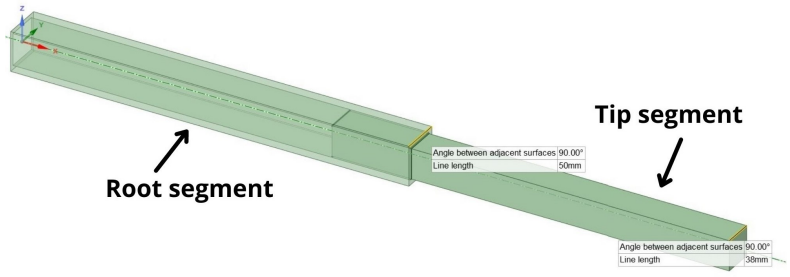

Figure 4.3: Structural model for Case 2 (trimetric view).

In order to begin the analysis of this case, it is important to understand the type of support of the tip segment at its inboard segment. Since there are two compression forces acting in the overlapped parts, it is necessary to simulate those exact forces in the structural model. For that, four small pieces were built inside the root part (Fig. 4.4) in order to guarantee that when the tip segment touches them as a reaction of the applied load, there is compression being simulated in the normal direction. On the other hand, the two faces can also separate from each other in the normal direction but there is no movement whatsoever in the tangential direction. These four pieces have a very small dimension ($1mm$) in the XZ plane, so they do not influence significantly the beam's cross-section area moment of inertia (I). This will, however, introduce some error in the final results which will later be taken into account.

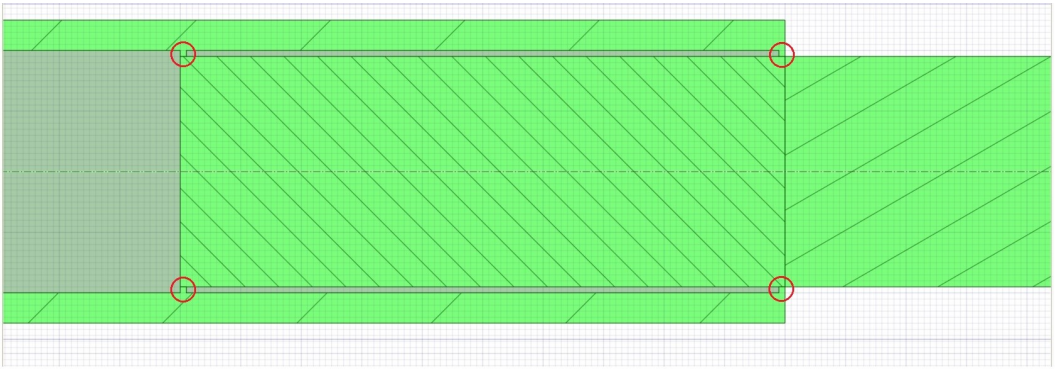

Figure 4.4: Structural model with XZ plane cross-section and support pieces.

With the structural model built, it is possible to start applying the mesh method in Ansys's workbench. The method chosen is, like in the first case, the Tetrahedron method, with computer controlled element order. The final generated and refined mesh is visible in Figure 4.5.

With the mesh generated, it is necessary to apply the boundary conditions. These consist in a fixed support at the beginning of the root segment, which simulates a cantilever-type support. Next, the load on the top faces of the beam and the contacts between the different bodies are applied. These contacts are a *Bonded* contact between the two bodies that compose the tip segment, which ultimately behave as a single body, and a *Rough* contact between the support pieces and the tip segment. Finally, the material properties of each body that allow to control the flexural rigidity ratio are applied.

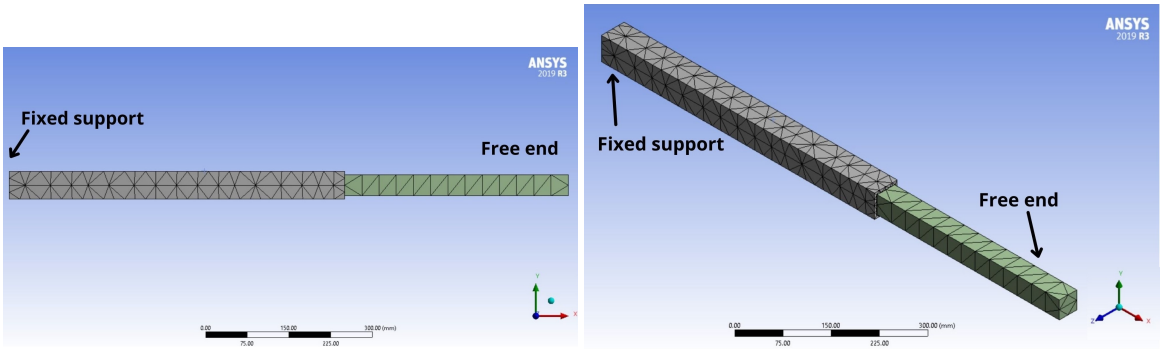

(a) Mesh (side view). (b) Mesh (isometric view).

Figure 4.5: Case 2 Tetrahedron method mesh.

To finish the analysis, a solution for directional deformation is applied in the Y direction in order to be in accordance with the global coordinate system, to obtain the results for the beam's deflection. The results for this deformation are presented in Chapter 6.

4.3 Case 3

Case 3 is very similar to the second case in the way that the tip segment goes inside the root segment. However, there is no need for the support pieces because the contact between both segments must be continuous. Figure 4.6 shows the structural model built using *SpaceClaim* [26] where it is possible to see the three bodies that compose it. Again, like in Case 2, one of the bodies represents the root segment and the other two represent the tip segment.

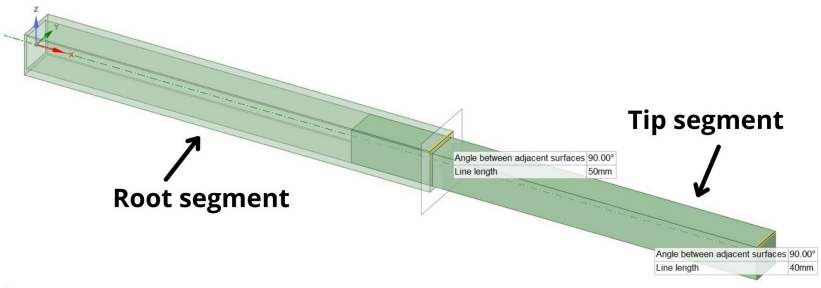

Figure 4.6: Structural model for Case 3 (trimetric view).

Although the bodies are in full contact with each other, the cross-sections are not equal so some calculations are required in order calculate the correct flexural rigidity ratio. Similarly to Case 2, the root segment has a hollow squared cross-section and the tip segment is a solid body with a solid squared cross-section (see 6.3). The length ratios K_{L_0} and K_{L_2} are also chosen.

So as to begin the analysis, once again we need to understand the contacts between the bodies and segments and to ensure that the two bodies that compose the tip segment work as one, a *Bonded* contact is applied, so no movement between them is allowed whatsoever. For the contact between the tip and root segment, a *Rough* contact is applied to each face of both

bodies in the horizontal plane. This contact will allow separation in the normal direction, if necessary, and compression when in contact, but it does not allow any movement in the tangential direction (Fig. 4.7).

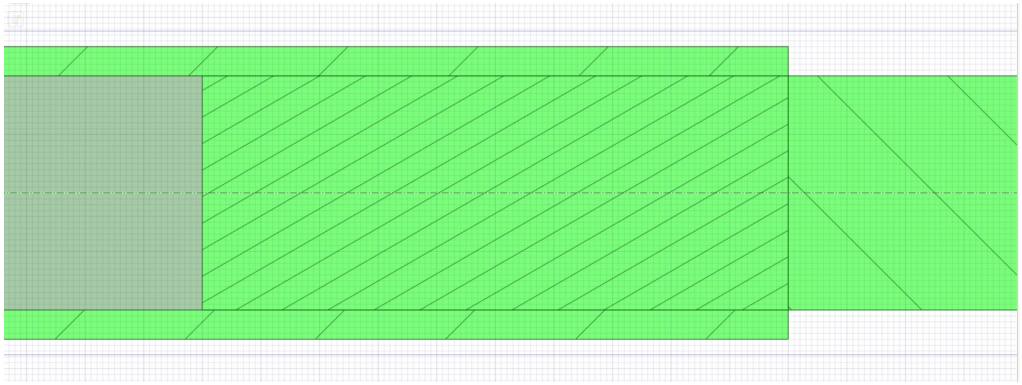

Figure 4.7: Structural model with XZ plane cross-section and visible continuous contact.

Having the structural model finished, we can apply the mesh method in ANSYS's workbench, which is the same as the previous two cases, the Tetrahedron method with computer controlled element order. Figure 4.8 shows the final generated and refined mesh:

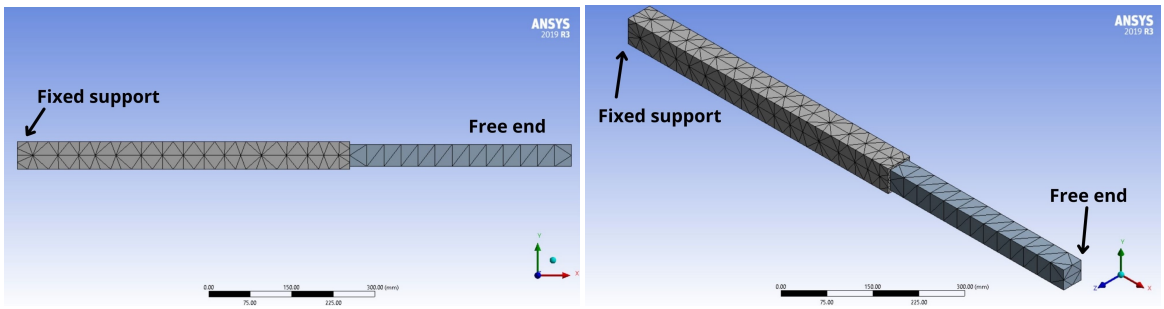

(a) Mesh (side view). (b) Mesh (isometric view).

Figure 4.8: Case 3 Tetrahedron method mesh.

After the discretization of the model, we can apply the boundary condition which is a fixed support at the left face of the root segment that represents the cantilever support. Also the applied load is added on the top faces of the beam on the root segment body and on the outer body of the tip segment. This is the reason why two bodies compose the tip segment, because the load does not act on the overlapping part. Lastly, the materials are applied to each body with the properties that allow K_{EI} to have the chosen value.

To obtain the results for the deflection, a solution for directional deformation is applied in the Y direction. Again, the directions of the boundary conditions, applied load and solutions must be consistent with the global coordinate system. The results for this deformation are presented in Chapter 6.

Chapter 5

Analytical Results

In this chapter, the results regarding the analytical analysis of the beam's deflection are presented. As stated in the first chapter, the goal of this study is to understand how the different types of support of the different segments of the telescopic beam, as well as how the characteristics of those segments influence the rotation and deflection of the beam. After all the necessary calculations are made and the equations defining the rotation and deflection for the tip of the beam are obtained, a MATLAB code was built in order to plot these equations. The values of K_{L_2} and K_{EI} are iteratively specified in order to evaluate the changes in the rotation and deflection at the tip of the beam described by the equations obtained in Chapter 3.

The different plots presented are based on two different situations: the first one implies that K_{L_2} has constant value and K_{EI} varies in the interval $]0, 1]$. These values were chosen because if $K_{EI} = 0$, we obtain undefined divisions (see 3.2.3 and 3.3.4) and when $K_{EI} = 1$, the flexural rigidities of both parts of the beam are equal. This being said, there are no defined values of rotation or deflection in the plots for $K_{EI} = 0$.

The second situation implies that K_{EI} has constant value and K_{L_2} varies in the interval $K_{L_2} = 0$, which means that the beam is only made up by the the root part and therefore equivalent to a uniform beam, and $K_{L_2} \leq \frac{1}{2}(1 - K_{L_0})$, the boundary condition that maximizes K_{L_2} (3.13) allowing us to understand how that segment's length affects the rotation and deflection.

5.1 Case 1

5.1.1 Rotation and deflection along the beam's length

For the first case, let us first plot the equations that describe the rotation and deflection throughout the beam. For this we take equations 3.38 and 3.39, which describe the rotation and deflection for the root segment and equations 3.49 and 3.50, which describe the rotation and deflection for the tip segment, respectively, and plot them using MATLAB.

To make things simple, we plot $\frac{dy}{dx} / \frac{wL^3}{6EI_1}$ as a function of $\overline{x} = x/L$ for the rotation and $y / \frac{wL^4}{24EI_1}$ as a function of $\overline{x} = x/L$ for the deflection. The values chosen for K_{EI} are 1, for control, and 0.5 for comparison and the value chosen for K_{L_2} is 0.4, randomly. Remembering 3.9 and 3.10, which are equivalent because $K_{L_0} = 0$, we know that the discontinuity point must be $\overline{x} = 0.6$. Figures 5.1 (a) and (b) represent the displacements along the beam and how they

change due to flexural rigidity differences between the root and tip parts.

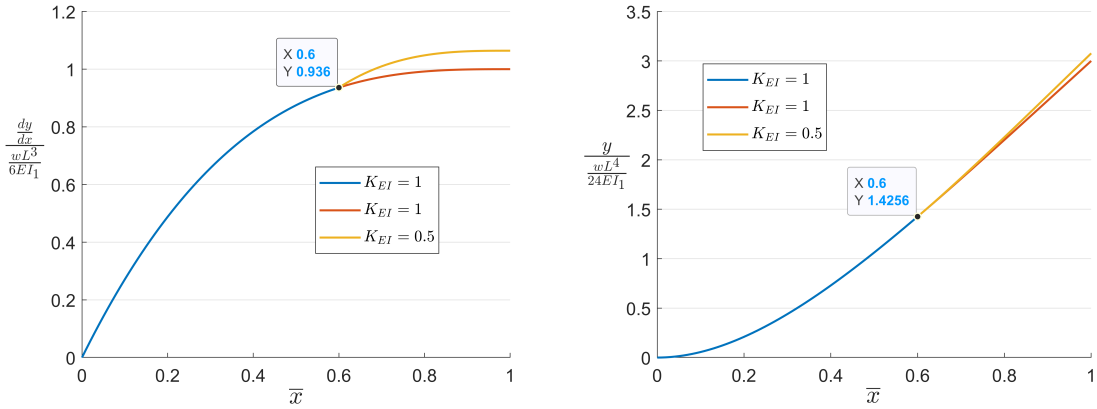

(a) Rotation.

(b) Deflection.

Figure 5.1: Sample displacements throughout the beam's length for different values of K_{EI}.

In Figure 5.1(a), it is possible to see the discontinuity point of the beam and the value of the rotation for that point, that is the same for every plotted equation. The blue line corresponds to the rotation equation of the root segment $(0 \leq \overline{x} \leq 0.6)$ and the orange (below) and yellow (above) lines correspond to the rotation equation of the tip segment $(0.6 < \overline{x} \leq 1)$. In that same Figure, we can see that the difference between the orange (bellow) and yellow (above) lines is due to the flexural rigidity, that is, smaller EI results in larger rotation.

In Figure 5.1(b), at the same point $(\overline{x} = 0.6)$, the value of the deflection is the same for the equations plotted and the function is continuous, regardless of the value of K_{EI} and K_{L_2}. Similarly to the rotation plot, the blue line represents the deflection for the root segment of the beam $(0 \leq \overline{x} \leq 0.6)$ and the orange and yellow lines correspond to the deflection on the tip segment of the beam $(0.6 < \overline{x} \leq 1)$.

The yellow line has higher deflection value than the orange line because it corresponds to a smaller EI. This change only occurs on the tip segment because the equations do not depend directly of EI_1, the flexural rigidity of the root part, but instead of K_{EI}, the flexural rigidity ratio.

5.1.2 Rotation and deflection on the beam's tip

Next, we analyze the rotation and deflection ratio, which is the comparison with a uniform beam and for that we apply equations 3.53 and 3.54 to the MATLAB code, and obtain the following plots, for rotation and deflection (Figs. 5.2 and 5.3).

The constant values chosen for K_{L_2} are 0.1, 0.2, 0.3, 0.4 and 0.5. It is important to note that because $K_{L_0} = 0$ for the first case, the maximum value for K_{L_2} is 0.5 and, because when $K_{L_2} = 0$ we have just the root part of the beam, it is more interesting to evaluate what

happens if K_{L_2} has a value closer to zero than being actually zero. The constant values chosen for K_{EI} are 0.2, 0.4, 0.6, 0.8 and 1 and were chosen in such way that they are evenly distributed along the interval stated in the beginning of this chapter.

- Rotation:

After plotting equation 3.53 with the values stated earlier, we obtain two different graphs which can be seen in Figures 5.2 (a) and (b).

From Figure 5.2(a), where the value that remains constant is K_{L_2}, the rotation at the tip of the beam is higher when K_{EI} has lower values and K_{L_2} has higher values. This means that the rotation is higher when the tip part of the beam has smaller flexural rigidity than the root part, and also when the telescopic segment is larger. As K_{EI} approaches 1, for any value of K_{L_2}, the rotation gets closer to the value of the rotation for a uniform beam.
Knowing this, the following can be stated:

$$\lim_{K_{EI}\to 1} \frac{\left(\frac{dy}{dx}\right)_L}{\left(\frac{dy}{dx}\right)_U} = 1 \quad (5.1)$$

From Figure 5.2(b), the same phenomena can be seen in the line represented by $K_{EI} = 1$ which, regardless of the value of K_{L_2}, is constant and equal to 1. This lets us know that one of the most important characteristics of the beam that influences the rotation is the flexural rigidity.

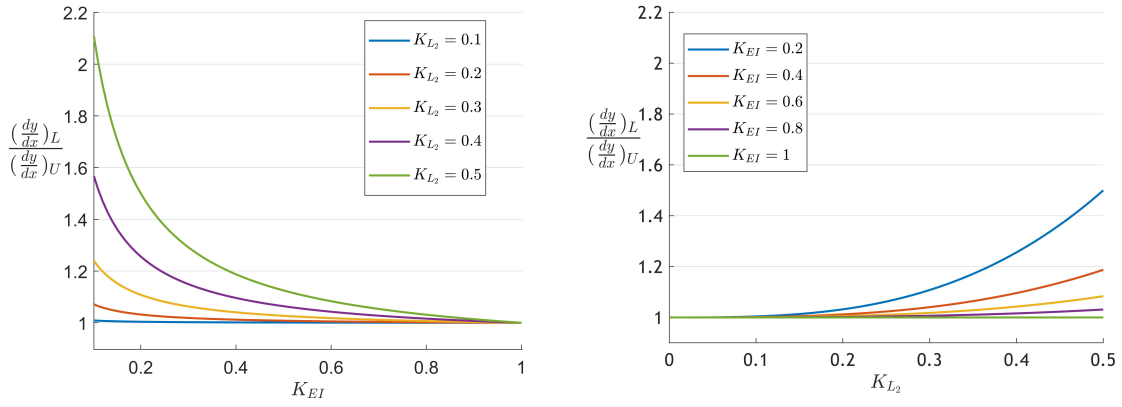

(a) Tip rotation with constant K_{L_2}.

(b) Tip rotation with constant K_{EI}.

Figure 5.2: Tip rotation - comparison with uniform beam.

- Deflection:

In order to analyze the deflection of the beam, we first need to analyze Figures 5.3 (a) and (b). Similarly to the rotation, there is no value for the deflection when $K_{EI} = 0$.
From Figure 5.3(a) we can see that for any value of K_{L_2}, when K_{EI} reaches 1, i.e. both segments of the beam have the same flexural rigidity, the deflection ratio has a value of 1,

which is the same as being a uniform beam.
This result enables to state that:

$$\lim_{K_{EI}\to 1} \frac{(y)_L}{(y)_U} = 1 \quad (5.2)$$

From Figure 5.3(b), it is possible to see that smaller values of K_{EI}, meaning that the tip segment has lower flexural rigidity, lead to a larger deflection of the tip of the beam which in turn increases as the extending length increases.

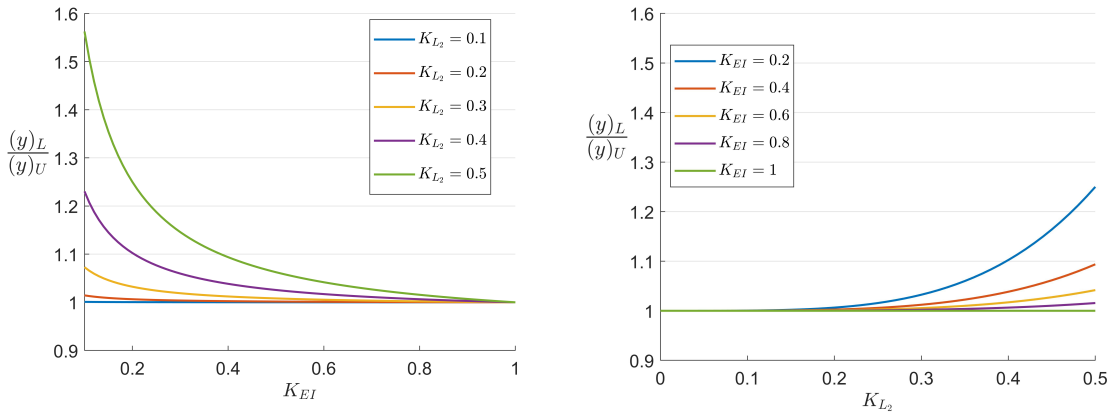

(a) Tip deflection with constant K_{L_2}.

(b) Tip deflection with constant K_{EI}.

Figure 5.3: Tip deflection - comparison with uniform beam.

By observing the graphs of Figure 5.3, we can write the following:

• The closer K_{EI} gets to 1, the smaller and closer the rotation and deflection of the tip of the beam gets to a uniform beam, regardless of the length of the tip segment.

• For smaller K_{EI} values, but larger K_{L_2} values, the larger the rotation and deflection of the tip of the beam gets and further away from the values for a uniform beam.

This happens for Case 1 due to the fact that the tip segment is cantilevered at its inboard segment ($K_{L_0} = 0$) so the influence of the tip segment on the root segment is minimal.

5.2 Case 2

5.2.1 Rotation and deflection along the beam's length

So far, Case 1 was simpler due to the fact that $K_{L_0} = 0$, which gives only two different lines in the rotation and deflection plots. Since this no longer applies to Case 2, we have three sections on the plots.
Just like the previous section, the respective equations are plotted using MATLAB. These equations are, for the rotation, equations 3.81, 3.92 and 3.103, and for the deflection equations 3.82, 3.93 and 3.104. To simplify, we plot $\frac{dy}{dx}/\frac{wL^3}{12EI_1}$ as a function of $\overline{x} = x/L$ for the

rotation and $y/\frac{wL^4}{24EI_1}$ as a function of $\overline{x} = x/L$ for the deflection.

The values chosen for K_{EI} are, like previously, 1 for control and 0.5 for comparison, and for K_{L_2} the value chosen is 0.4, randomly. For K_{L_0} a value of 0.1 was selected, which is explained hereunder. From 3.9 and 3.10, we obtain the discontinuity points of the beam for the next example, which are $\overline{x}_a = 0.5$ and $\overline{x}_b = 0.6$. Figures 5.4 (a) and (b) represent the displacements along the beam and how the change in the flexural rigidity influences these displacements:

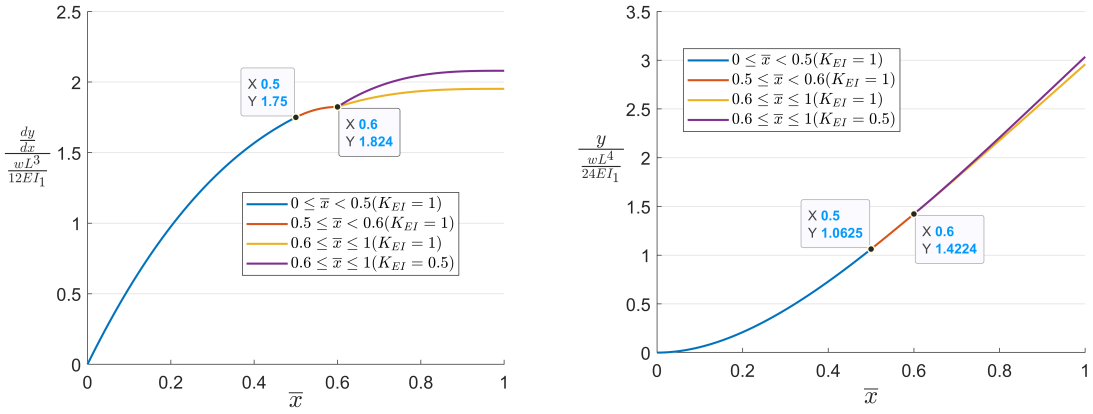

(a) Rotation.

(b) Deflection.

Figure 5.4: Sample displacements along the beam's length for different values of K_{EI}.

Figure 5.4(a) describes the rotation along the beam and it is possible to see the three different segments, separated by the two discontinuity points and their values, which are equal for the first two equations at $\overline{x}_a$ and equal for the second and third equations at $\overline{x}_b$. The blue line corresponds to the rotation equation of the root segment $(0 \leq \overline{x} < 0.5)$, the orange line corresponds to the rotation equation for the overlapping segment $(0.5 \leq \overline{x} < 0.6)$ and the yellow and purple lines correspond to the rotation equation for the tip segment $(0.6 \leq \overline{x} \leq 1)$. Because the purple line (above) stands for a smaller value of K_{EI}, its values of rotation are higher than the ones described by the yellow line (below).

For the deflection equations we have Figure 5.4(b) and again, the first two equations have the same value at $\overline{x}_a$ and the second and third have the same value at $\overline{x}_b$, and maintain the continuity of the deflection function. The blue line represents the deflection on the root segment $(0 \leq \overline{x} < 0.5)$, the orange line represents the deflection on the sliding inner section $(0.5 \leq \overline{x} < 0.6)$ and the yellow and purple lines correspond to the deflection on the tip segment of the beam $(0.6 \leq \overline{x} \leq 1)$. Because the purple line (above) represents a smaller K_{EI}, its deflection values are higher than the yellow line's (below) values.

Now that we have an idea of how the rotation and deflection change along the beam for Case 2, let us see how the tip displacements change comparing to a uniform beam.

5.2.2 Rotation and deflection at the beam's tip

Applying equations 3.107 and 3.108 to the MATLAB code previously built allows us to plot the rotation an deflection of the tip of the beam for the second case. Because K_{L_0} is different than zero, two values were attributed: 0.1 and 0.05. These values represent an inner section of contact of the two segments of 10% and 5% of the length of the beam, respectively.

The values for K_{EI} are the same as the ones chosen for Case 1, i.e. 0.2, 0.4, 0.6, 0.8 and 1, and so are the values of K_{L_2} with exception of the maximum value which, from $K_{L_2} \leq \frac{1}{2}(1-K_{L_0})$, the boundary condition that maximizes K_{L_2} (3.13), is equal to 0.45 for $K_{L_0} = 0.1$ and 0.475 for $K_{L_0} = 0.05$.

- Rotation

Plotting equation 3.107 with the values from above gives the graphs that describe the rotation ratio that can be seen in Figures 5.5 (a) and (b) $(K_{L_0} = 0.1)$ and Figures 5.6 (a) and (b) $(K_{L_0} = 0.05)$.

In Figure 5.5(a) K_{L_2} has constant value and the values for the rotation at the tip are higher for lower values of K_{EI} and higher values of K_{L_2}. This tells us that the rotation is higher when the tip segment has smaller flexural rigidity than the root segment and when the telescopic segment is larger. As K_{EI} increases, the rotation approaches the uniform beam's rotation. At a certain value of K_{EI}, approximately 0.8, the rotation gets smaller than the rotation of the uniform beam, for higher values of K_{L_2}. This means that after that point of K_{EI}, the larger the telescopic segment, the smaller the rotation ratio gets.

In Figure 5.6(a) the same can be verified but the overall values of the rotation ratio are higher for small values of K_{EI}. When the latter approaches 1, the rotation is still smaller than the uniform beam, but higher than it is for $K_{L_0} = 0.1$ in Figure 5.5(a).

Now turning our attention to Figure 5.5(b), where the constant value is K_{EI}, it is possible to see that the less extended the telescopic segment is, the closer the rotation is to the uniform beam. As K_{L_2} gets higher, the rotation ratio also gets higher for smaller values of K_{EI}. For higher values of K_{EI}, around 0.8, the opposite happens and the rotation gets smaller than the uniform beam's rotation.

The same phenomena can be seen for a smaller value of K_{L_0} in Figure 5.6(b) but the overall values of rotation ratio are higher, which is consistent with a smaller contact length between the root and tip segments and with what was concluded between Figures 5.5(a) and 5.6(a).

- Deflection

Applying equation 3.108 to MATLAB with the values of K_{EI}, K_{L_2} and K_{L_0} chosen in 5.2.1 and 5.2.2 allows us to obtain the plots that describe the deflection ratio at the tip of the beam,

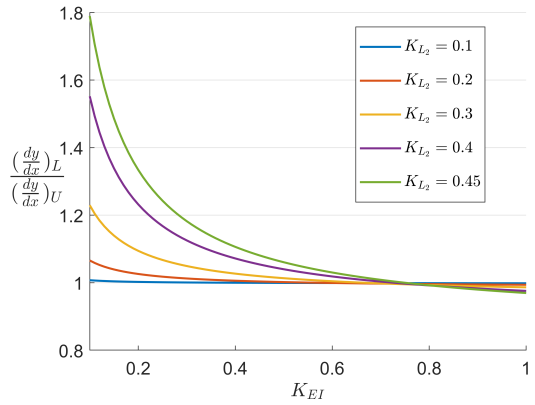

(a) Tip rotation with constant K_{L_2}.

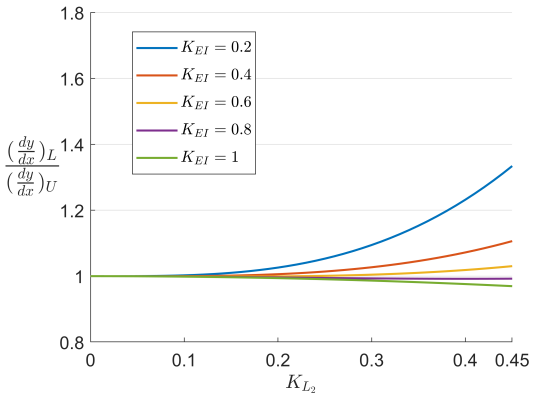

(b) Tip rotation with constant K_{EI}.

Figure 5.5: Tip rotation - comparison with uniform beam for $K_{L_0} = 0.1$.

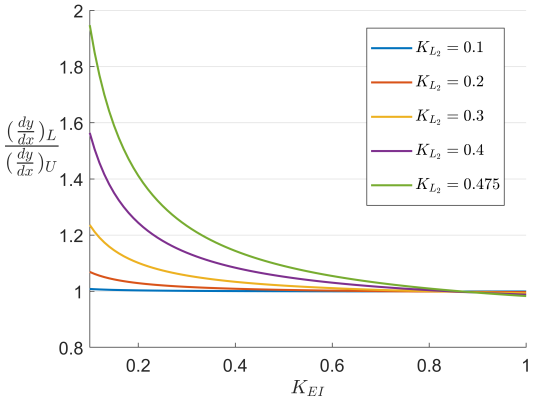

(a) Tip rotation with constant K_{L_2}.

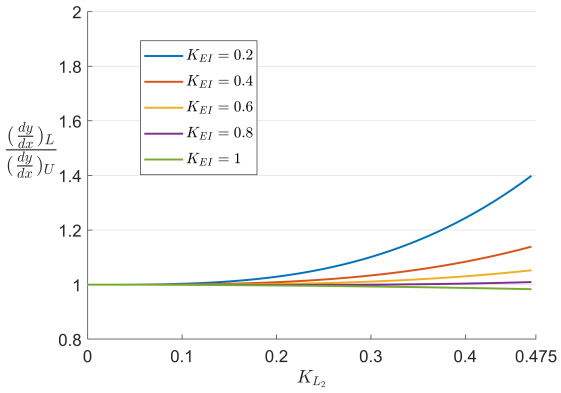

(b) Tip rotation with constant K_{EI}.

Figure 5.6: Tip rotation - comparison with uniform beam for $K_{L_0} = 0.05$.

which can be seen in Figures 5.7 (a) and (b), for $K_{L_0} = 0.1$, and Figures 5.8 (a) and (b), for $K_{L_0} = 0.05$.

In Figure 5.7(a) the fixed value is K_{L_2} and we can see that for lower values of K_{EI} and higher values of K_{L_2}, the deflection takes higher values and strays away from the uniform beam values, meaning that when the tip segment has lower flexural rigidity than the root segment and the larger the telescopic section is, the higher are the values of the deflection. When K_{EI} increases, the deflection values decrease and approach the uniform beam values of deflection. Similarly to the rotation, at a certain value of K_{EI} the deflection ratio gets smaller than 1 for higher values of K_{L_2}, meaning that from that point on, the larger the telescopic segment, the lower the deflection ratio gets. This can be explained by the existence of a downwards force at the interface that counteracts the deflection and depends on the length of the segments.

Figure 5.8(a) represents the same changes as Figure 5.7(a) but with a smaller value of K_{L_0}. The mechanical behavior is similar with the latter case but with the difference that the overall values of deflection ratio are higher and the deflection ratio only gets smaller than 1 at a

higher value of K_{EI}.

Looking now at Figure 5.7(b), where the fixed value is K_{EI}, it is possible to see that less extension of the telescopic segment means a deflection value closer to the uniform beam. As K_{L_2} approaches its maximum value, the deflection ratio also gets higher for smaller values of K_{EI}. However, when K_{EI} has high values such as 1, the deflection is smaller than the deflection of a uniform beam. In Figure 5.8(b) the same results are visible but the majority of the deflection ratio values are higher.

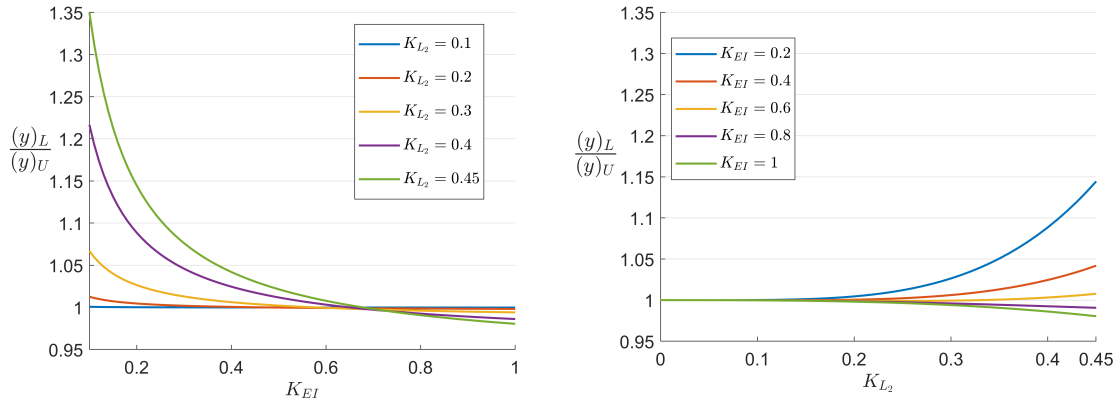

(a) Tip deflection with constant K_{L_2}.

(b) Tip deflection with constant K_{EI}.

Figure 5.7: Tip deflection - comparison with uniform beam for $K_{L_0} = 0.1$.

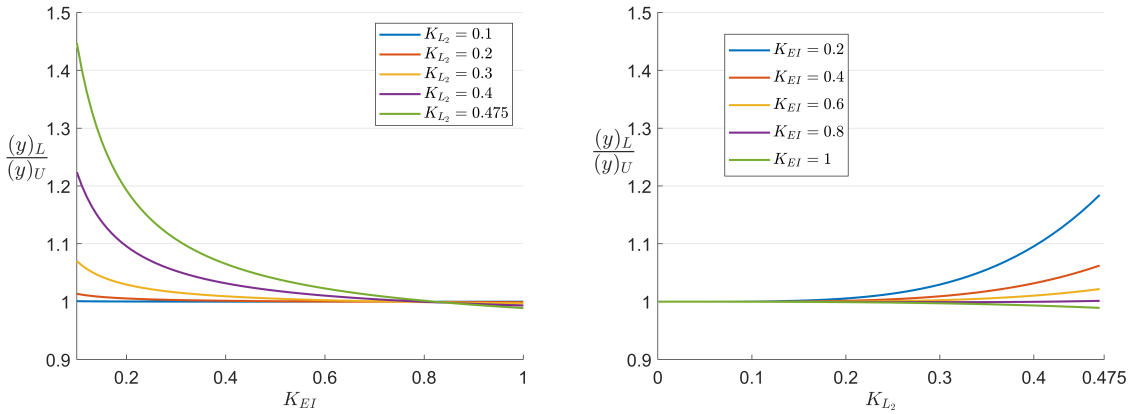

(a) Tip deflection with constant K_{L_2}.

(b) Tip deflection with constant K_{EI}.

Figure 5.8: Tip deflection - comparison with uniform beam for $K_{L_0} = 0.05$.

Having the rotation and deflection plots analyzed, we can conclude that:

• For small values of K_{EI}, the longer the telescopic segment the higher the value of the rotation and deflection of the tip of the beam.

• As K_{EI} gets higher, the rotation and deflection ratios get closer to 1 until a certain value where they get smaller than 1. After that, the higher the value of K_{L_2}, the smaller the dis-

placements are in comparison with the uniform beam.

• For small K_{EI} values, but high K_{L_2} values, the larger the displacements of the tip of the beam and further away from the values of a uniform beam.

• A lower value of K_{L_0} means a higher rotation and deflection for the majority of values of K_{EI} and K_{L_2}.

In Case 2 it is possible to see that if an inner sliding section exists $(K_{L_0} \neq 0)$, its length has influence on the displacement that occur on the beam.

5.2.3 Ideal length of overlapping segment for minimum deflection

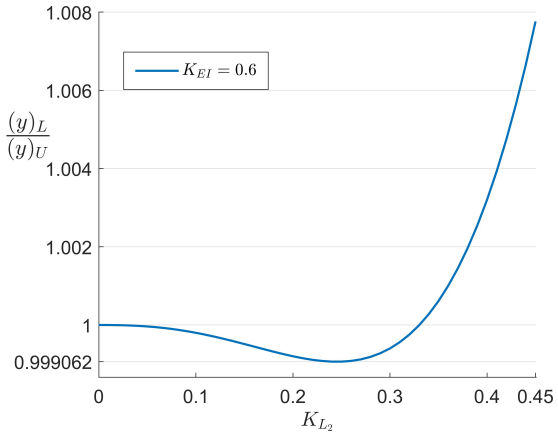

Figure 5.9: Tip deflection for $K_{EI} = 0.6$ and $K_{L_0} = 0.1$.

In Figure 5.9 an example plot for the deflection is visible and the values attributed are $K_{EI} = 0.6$ and $K_{L_0} = 0.1$. There, it is possible to see that even though the value of K_{L_2} increases, there is an interval, approximately between 0.1 and 0.35, on which the value of the deflection decreases and is lower than 1 and then it increases again. This means that on that interval, the deflection is smaller than the deflection for a uniform beam.

These results are in accordance with the hypothesis presented in the beginning of this study, where it was proposed that an ideal interval of telescopic segment length exists where the deflection value decreases, before it increases again until it reaches its maximum value.

5.3 Case 3

5.3.1 Rotation and deflection along the beam's length

The analysis of Case 3 is similar to the analysis of Case 2. Making use of MATLAB, the equations regarding the beam's displacements are plotted and they are, for the rotation, equations 3.136, 3.147 and 3.158 and, for the deflection, equations 3.137, 3.148 and 3.159. Again, to sim-

plify the analysis, we plot $\frac{dy}{dx}/\frac{wL^3}{6EI_1}$ as a function of $\overline{x} = x/L$ for the rotation and $y/\frac{wL^4}{24EI_1}$ as a function of $\overline{x} = x/L$ for the deflection.

The values chosen for K_{EI} are once again 1 for control and 0.5 for comparison. For K_{L_0} the value chosen is again 0.1. The discontinuity points of the beam can be calculated from 3.9 and 3.10 and they are $\overline{x}_a = 0.5$ and $\overline{x}_b = 0.6$ for this example. Figures 5.10 (a) and (b) represent the rotation and deflection along the beam's axis and it is visible the changes that occur to those displacements due to a change in the flexural rigidity ratio:

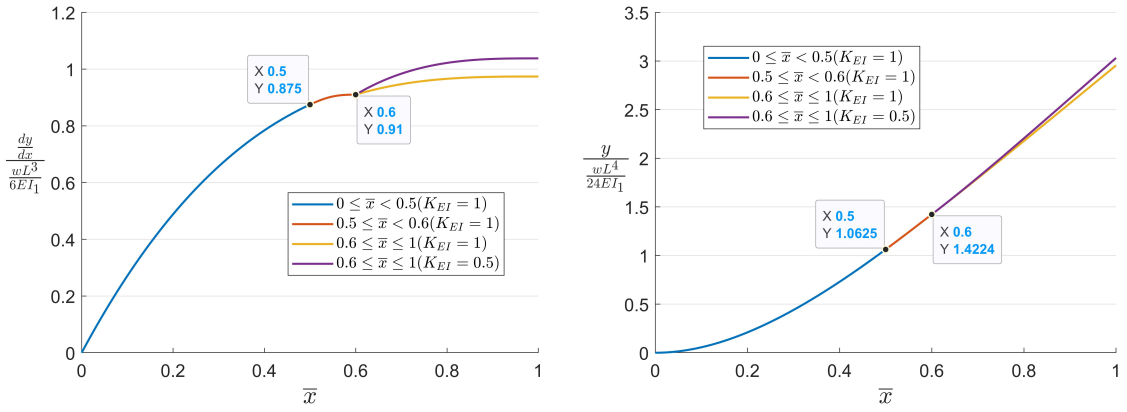

(a) Rotation.

(b) Deflection.

Figure 5.10: Sample displacements along the beam's length for different values of K_{EI}.

Figure 5.10(a) describes the rotation along the beam and three different segments are visible and are separated by two discontinuity points. Those points represent the changes in segments in the real beam. However, those points are only discontinuity points on the real beam and not in the analysis because the equations obtained guarantee that exists continuity in the displacement. This means that at $\overline{x}_a$, the first and second segment equations must have the same value and the same applies to to the second and third segments, at $\overline{x}_b$.

The blue line corresponds to the rotation equation of the root segment $(0 \leq \overline{x} < 0.5)$, the orange line corresponds to the rotation equation for the inboard segment $(0.5 \leq \overline{x} < 0.6)$ and the yellow and purple lines correspond to the rotation equation for the tip segment $(0.6 \leq \overline{x} \leq 1)$. Because the purple line (above) represents a smaller value of K_{EI}, its values of rotation are higher than the ones described by the yellow line (below).

The deflection equations are described in Figure 5.10(b) and their values must again be the same in each discontinuity points: the first and second segments have the same value at $\overline{x}_a$ and the second and third segments have the same value at $\overline{x}_b$. The blue line represents the deflection on the root segment $(0 \leq \overline{x} < 0.5)$, the orange line represents the deflection on the overlapping section $(0.5 \leq \overline{x} < 0.6)$ and the yellow and purple lines correspond to the deflection on the tip segment of the beam $(0.6 \leq \overline{x} \leq 1)$. Because the purple line (above) describes a smaller K_{EI}, its deflection values are higher than the yellow line's (below) values.

In the next subsection the displacement equations are compared with the control group, the uniform beam equations.

5.3.2 Rotation and deflection on the beam's tip

The process to analyze the displacement on the beam's tip is essentially the same as the two previous cases. Equations 3.162 and 3.163 are applied to the existent MATLAB code and values are attributed to the variables in question. These values are: for K_{L_0} - 0.1 and 0.05 - which represent an overlapping segment of 10% and 5%, respectively; for K_{EI} the values are the same as the ones chosen for Case 1 and 2, i.e. 0.2, 0.4, 0.6, 0.8 and 1, and so are the values of K_{L_2} with exception of the maximum value which, from 3.13, the boundary condition that maximizes K_{L_2}, is equal to 0.45 for $K_{L_0} = 0.1$ and 0.475 for $K_{L_0} = 0.05$.

- Rotation

By plotting equation 3.162 in MATLAB with the values stated above, the graphs obtained describe the rotation ratios seen in Figures 5.11 (a) and (b) $(K_{L_0} = 0.1)$ and Figures 5.12 (a) and (b) $(K_{L_0} = 0.05)$.

In Figure 5.11(a), K_{L_2} has constant value and the values for the rotation are higher for lower values of K_{EI} and higher values of K_{L_2}, meaning that the rotation at the tip increases when the tip segment has smaller flexural rigidity than the root segment and when the telescopic segment is larger. As K_{EI} increases, the rotation decreases and approaches the values of the uniform beam's rotation until it surpasses it to smaller values. This means that around $K_{EI} = 0.75$, the beam's rotation is smaller than the rotation of a uniform beam, even though the value of K_{EI} is still increasing. Also, the larger the telescopic segment, the smaller the rotation ratio gets.

In Figure 5.12(a) the same phenomena can be visualized but the overall rotation ratio values are higher and the point at which the ratio goes below 1 is higher (around 0.9).

Looking now to Figure 5.11(b), where K_{EI} is now constant, the smaller the telescopic segment is, the closer the rotation ratio gets to 1. As K_{L_2} increases, so does the rotation ratio for small values of K_{EI}. For values of K_{EI} higher than 0.6, the opposite happens and rotation ratio decreases.

In Figure 5.12(b), for smaller value of K_{L_0}, similar behavior can be observed but again with the overall values of rotation ratio higher than in Figure 5.11(b). In this case, for $K_{EI} = 0.8$ the rotation ratio is higher than 1, the same behavior as $K_{EI} = 0.6$, 0.4 and 0.2.

- Deflection

With equation 3.163 computed in MATLAB with the same values chosen for K_{L_2}, K_{L_0} and K_{EI}, Figures 5.13 (a) and (b) $(K_{L_0} = 0.1)$ and Figures 5.14 (a) and (b) $(K_{L_0} = 0.05)$ are

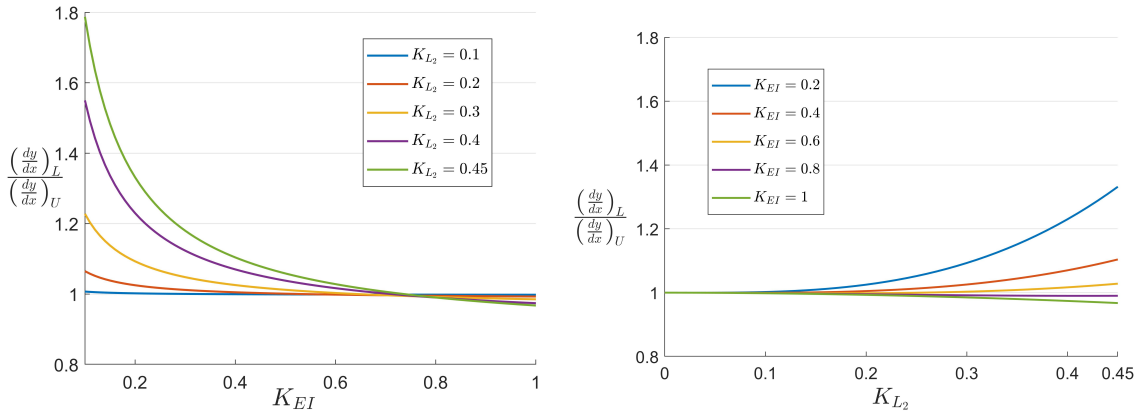

(a) Tip rotation with constant K_{L_2}.

(b) Tip rotation with constant K_{EI}.

Figure 5.11: Tip rotation - comparison with uniform beam for $K_{L_0} = 0.1$.

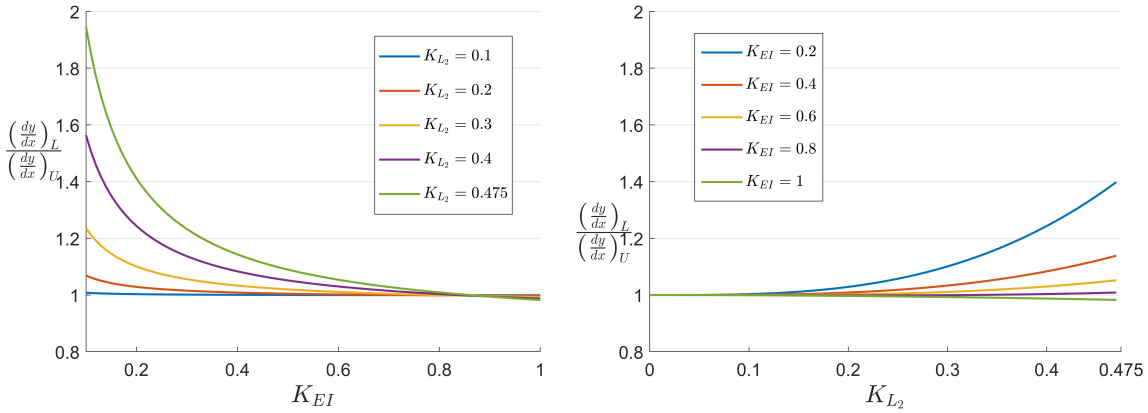

(a) Tip rotation with constant K_{L_2}.

(b) Tip rotation with constant K_{EI}.

Figure 5.12: Tip rotation - comparison with uniform beam for $K_{L_0} = 0.05$.

obtained, which describe the deflection ratio at the tip of the beam.

In Figure 5.13(a) K_{L_2} has fixed values and we see that the deflection ratio increases as K_{L_2} increases and K_{EI} decreases. An increasing value of K_{EI} causes the deflection ratio to decrease rapidly until, just as it happens for the rotation, it gets smaller than 1 for higher values of K_{L_2}. This means that after that point, the larger the telescopic segment is, the smaller the deflection comparing to a uniform beam. This behavior can be explained by the existence of a downwards load at the interface that counteracts the deflection and depends on the length of the segments.

Figure 5.14(a) shows the same behavior as the previous Figure for a value of $K_{L_0} = 0.05$. Similarly to the rotation, the overall values of deflection ratio are higher and the point where the deflection ratio gets smaller than 1 is much higher than it is for $K_{L_0} = 0.1$.

Figure 5.13(b) represents the same equations as the previous plots, but for a constant value of K_{EI}. Small values of K_{L_2} signify a deflection ratio close to 1. As K_{L_2} increases, so does

the deflection ratio for small values of K_{EI}. For higher flexural rigidity ratios such as 0.8 and 1, the deflection ratio is smaller than 1, i.e. a deflection value smaller than the deflection of a uniform beam. The same phenomena is visible in Figure 5.14(b) but most deflection ratio values are higher.

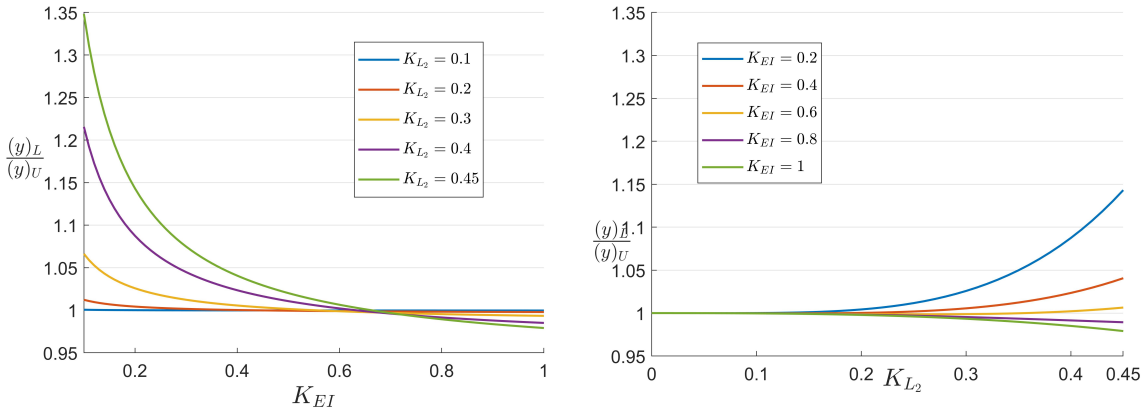

(a) Tip deflection with constant K_{L_2}.

(b) Tip deflection with constant K_{EI}.

Figure 5.13: Tip deflection - comparison with uniform beam for $K_{L_0} = 0.1$.

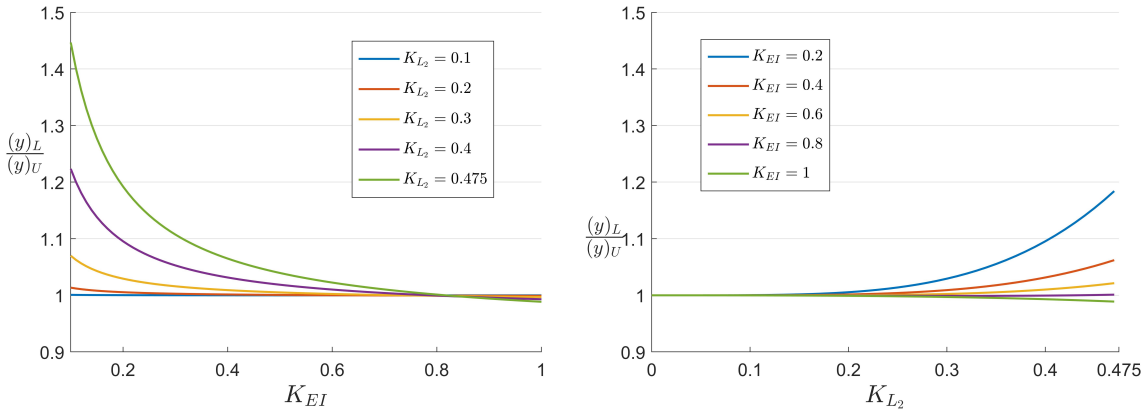

(a) Tip deflection with constant K_{L_2}.

(b) Tip deflection with constant K_{EI}.

Figure 5.14: Tip deflection - comparison with uniform beam for $K_{L_0} = 0.05$.

With the rotation and deflection plots analyzed, we can conclude that:

• For small values of K_{EI}, the longer the telescopic segment the higher the value of the rotation and deflection of the tip of the beam.

• As K_{EI} increases, the rotation and deflection ratios get closer to 1 until a certain value where they get smaller than 1. After that, the higher the value of K_{L_2}, the smaller the displacements are in comparison with the uniform beam.

• For small K_{EI} values, but high K_{L_2} values, the larger the displacements of the tip of the beam and further away from the values of a uniform beam.

• A lower value of K_{L_0} means a higher rotation and deflection for the majority of values of K_{EI} and K_{L_2}.

If an overlapping section exists ($K_{L_0} \neq 0$), its length has an influence on the displacements that occur on the beam.

5.3.3 Ideal length of overlapping segment for minimum deflection

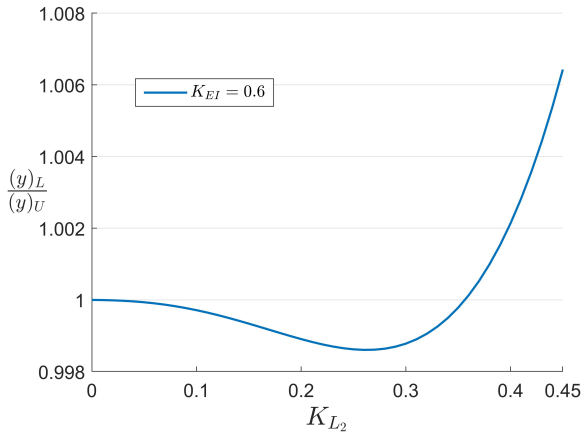

Figure 5.15: Tip deflection for $K_{EI} = 0.6$ and $K_{L_0} = 0.1$.

In Figure 5.15 represents an example plot for the deflection, whose attributed values are $K_{EI} = 0.6$ and $K_{L_0} = 0.1$, where it is visible that although the value of K_{L_2} increases, there is an interval, approximately between 0.1 and 0.38, where the value of the deflection decreases and is lower than 1 and then it increases again. This means that on that interval, the deflection is smaller than the deflection for a uniform beam.

Again, these results are in accordance with the hypothesis presented in beginning of this study, where it was proposed that an ideal interval of telescopic segment length exists where the deflection value decreases, before it increases again until it reaches its maximum value.

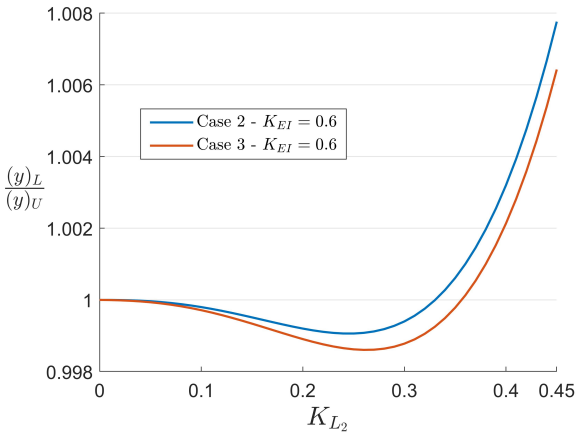

Figure 5.16: Tip deflection for $K_{EI} = 0.6$ and $K_{L_0} = 0.1$.

In Figure 5.16 are visible the equation plots for tip deflection for $K_{EI} = 0.6$ and $K_{L_0} = 0.1$ for Case 2 (eq. 3.108) and Case 3 (eq. 3.163), so they can be compared. It is possible to see that for Case 3, the deflection decreases more than with a Case 2 type of support.

Chapter 6

Numerical Results

To obtain valid results in this study, it is imperative that both analytical and numerical results are in accordance. It is obvious that, as explained earlier, some errors appear due to both computational and structural model design approximations but it is expected that these errors are reduced because the dimensions of the model and displacement are relatively small. In this chapter each case is analyzed separately for the numerical analysis and then compared with the respective analytic results. The choice of values for the different ratios was explained in Chapter 5 and those values were the ones used in the numerical analysis. Nevertheless, that choice and the respective values is again explained in this chapter, for each one of the different cases. The value chosen for E is the one from Structural Steel, $E = 2 \times 10^5 MPa$. Because the numerical analysis is an iterative process, it is necessary to chose a stopping criteria in order to stop the iterations. This criteria is the convergence of the mesh and it was chosen that a 1% change in the directional deformation value, from the previous iteration to the following, was sufficient to obtain good results.

6.1 Case 1

In Chapter 4, the method to numerically analyze the displacement of the beams was explained so now it is important to analyze the results. As seen, the beam for Case 1 has a very simple structural model and, because the cross-sections of each segment are the same, it is only necessary to change the value of E for the tip segment ($E_2 = 1 \times 10^5 MPa$), in order to obtain the desired value of $K_{EI} = 0.5$. Figure 6.1 shows the measures of the root and tip cross-sections, which are equal ($50mm$):

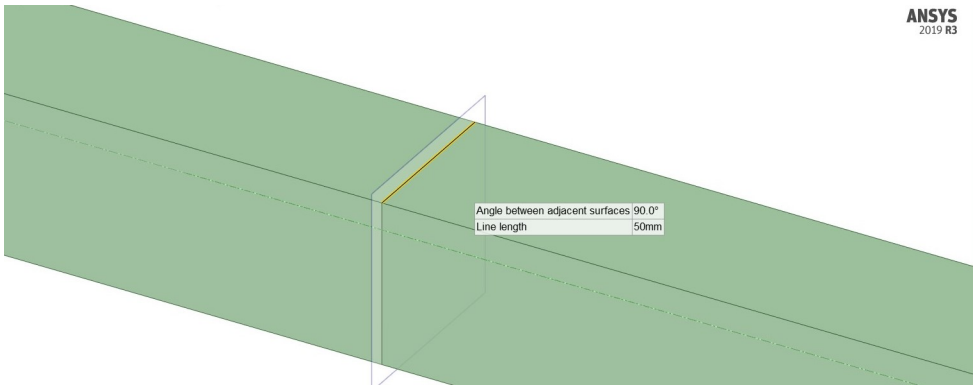

Figure 6.1: Case 1 beam's cross-section measures.

Since K_{L_2} can vary between 0 and $K_{L_2} \leq \frac{1}{2}(1 - K_{L_0})$, the value chosen is its maximum value, $K_{L_2} = 0.5$ and the total length of the beam is $L = 1000mm$. With these values as input, we obtain the following results from ANSYS:

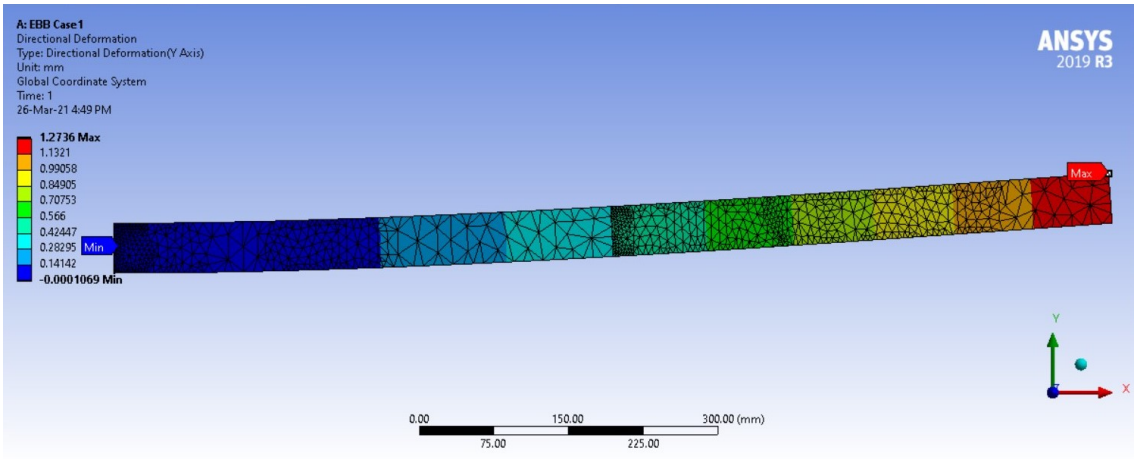

Figure 6.2: Directional deformation solution for Case 1 (side view).

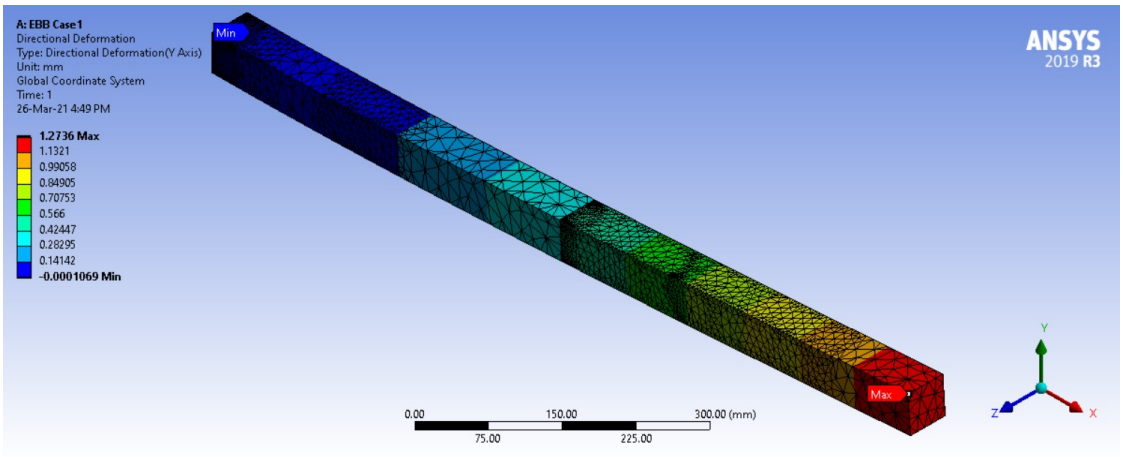

Figure 6.3: Directional deformation solution for Case 1 (isometric view).

From Figures 6.2 and 6.3 and left to right, it is visible that the deflection increases towards the beam's tip. The color scheme represents the "amount" of displacement; blue signifies a smaller deflection and red signifies a larger deflection. It is also visible the maximum value of deflection, which is $1.2736mm$.

Applying the same input values into equation 3.52, we obtain the following value for deflection on the tip of the beam, which is where the maximum value is located: $y = 1.2750mm$.

Figure 6.4 has the plots from ANSYS and from the equations obtained in Chapter 3 (eqs. 3.39 and 3.50) that describe the deflection along the beam's axis. It is visible that the curves overlap for the majority of values, especially on the root segment, and from the results of deflection, it is possible to state that the beam only suffers small deflections, i.e. the Euler-Bernoulli theory and the equations obtained accurately describe the deflection of the beam, and the structural model of that same beam is accurately built. A zoomed section of the plot is visible, around the tip, with both maximum deflection values.

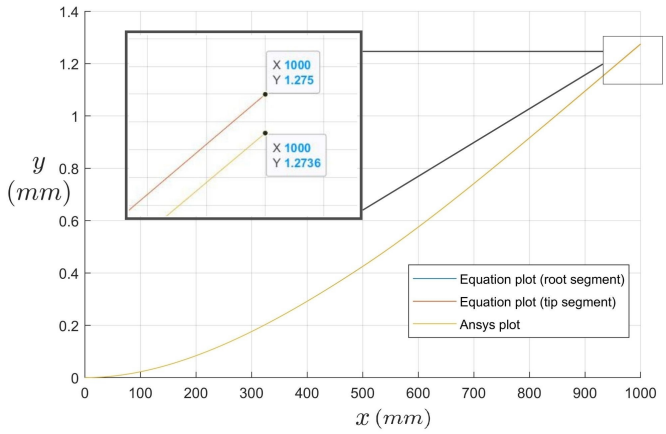

Figure 6.4: Case 1: Ansys and Equation graphs for deflection along the beam.

6.2 Case 2

Before analyzing the results for Case 2, it is necessary to present the values for the constants K_{EI}, K_{L_2} and K_{L_0} and how those values were chosen. Firstly, let us analyze the beam's cross-sections, seen in Figure 6.5:

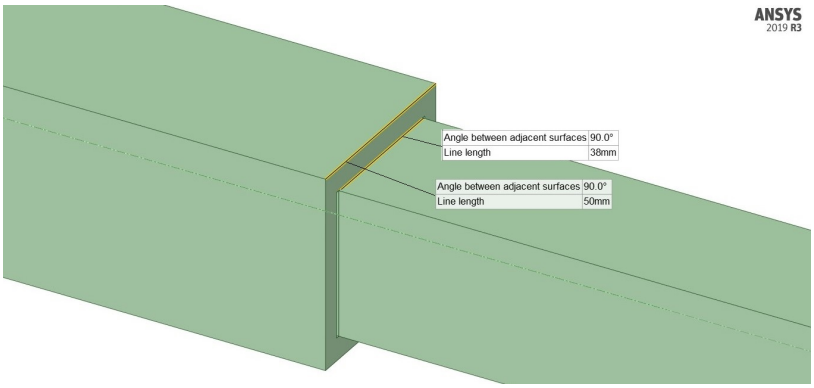

Figure 6.5: Case 2 beam's root and tip cross-section measures.

As seen above, the root segment is a hollow body and its cross-section has a side length of $50mm$ and a thickness of $5mm$, except on two points of the inside horizontal faces, where the support pieces are applied. This means that the thickness of the tip segment's cross-section must be $38mm$. Due to the fact that these support pieces are only on the horizontal plane, there is a gap between the vertical faces of segments, which introduces an error in the final result for deformation. However, as shall be seen hereunder, this error is rather small.

Understanding how the cross-sections are built, it is possible to do the necessary calculations to obtain the values of I and apply a correct value of E_2 ($1.7697 \times 10^5 MPa$) to the tip segment and obtain $K_{EI} = 0.5$. The values for K_{L_2} and K_{L_0} are, just like in the previous chapter, 0.4 and 0.1, respectively and the total length of the beam is $L = 1000mm$. Introducing these values in ANSYS, the following results are obtained:

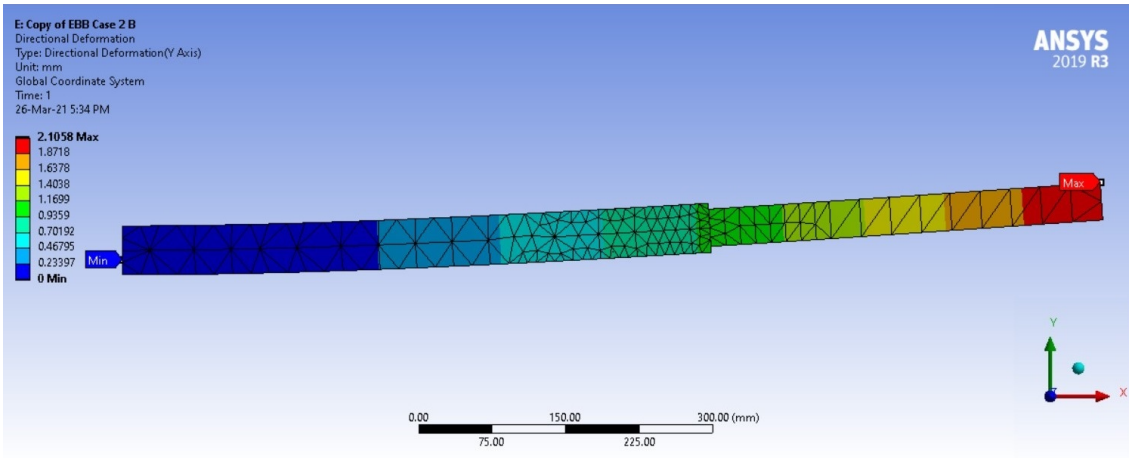

Figure 6.6: Directional deformation solution for Case 2 (side view).

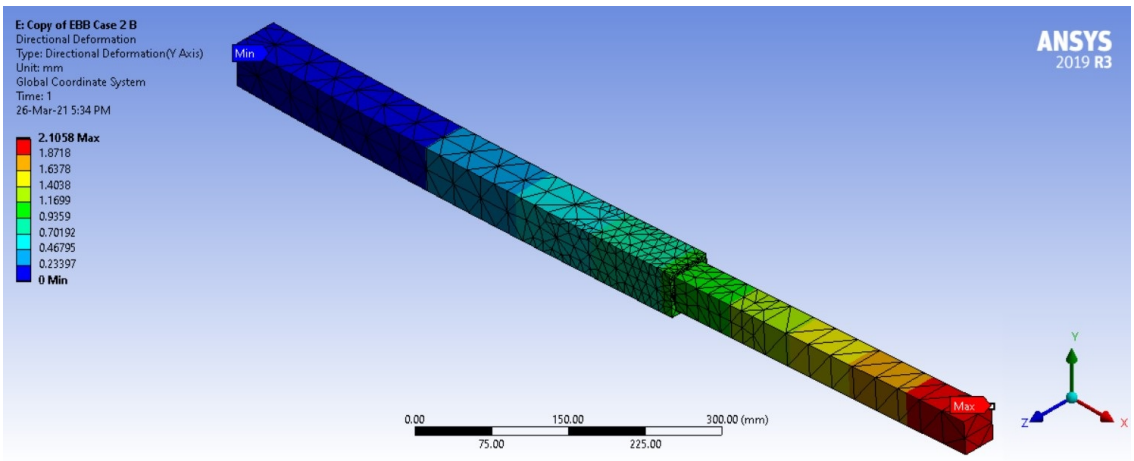

Figure 6.7: Directional deformation solution for Case 2 (isometric view).

Figures 6.6 and 6.7 show the results of the deflection along the beam's axis using a color scheme that means that the deflection increases towards the tip of the beam, blue being the smallest values and red the highest. The maximum value of displacement is also visible, and it is equal to $2.1058mm$

Applying the same input values into equation 3.106 returns the value of the deflection at the tip of the beam, which is $2.0564mm$. These results are consistent with the Euler-Bernoulli theory because of their low values and also it is possible to see the error that exists due to the support pieces and the area moment of inertia. It is known that the numerical value must be larger than the analytical value because of the way that the structural model is built. The amount of deformation that the tip segment exerts on the root segment is much higher in the numerical analysis than in the analytical, where this is not possible to take into account. The tip segment, while deforming upwards, forces the opening of the root segment to widen in the Y direction (red arrows in Fig. 6.8).

In Figure 6.8 it is possible to see the behavior of the support pieces and the inboard segment as well as their reaction to the applied load, where two of them are in compression with the

tip segment's faces.

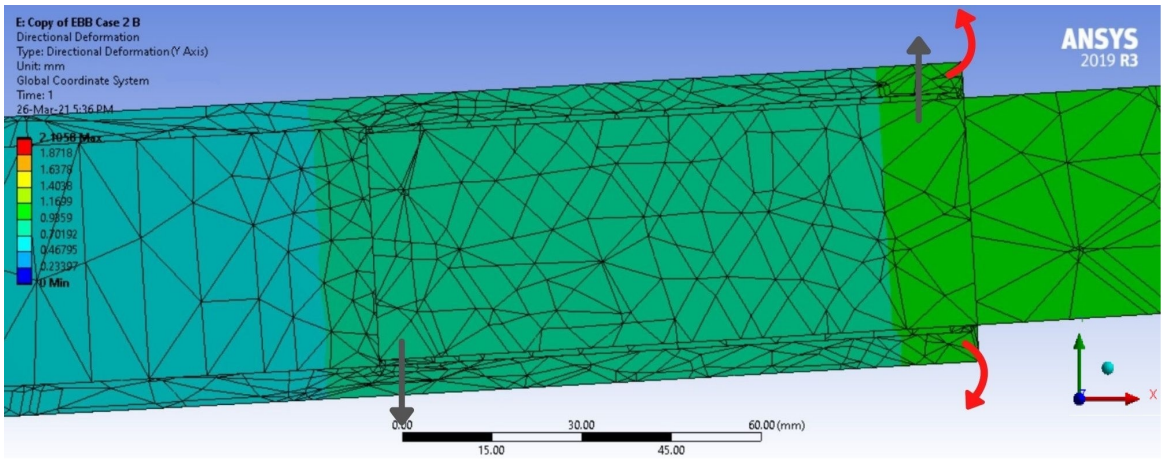

Figure 6.8: XY plane cross-sectional solution at the support pieces and internal mesh elements.

In Figures 6.9 (a) and (b) it is visible where the two segments separate from each other due to the deformation. This happening, signifies that the support pieces work how they are supposed to. By separating on one side, they must exert compression on the opposite side.

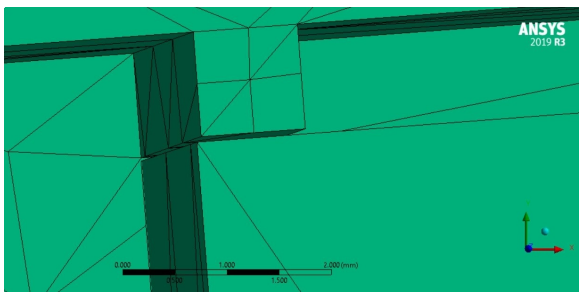

(a) Upper left side support piece.

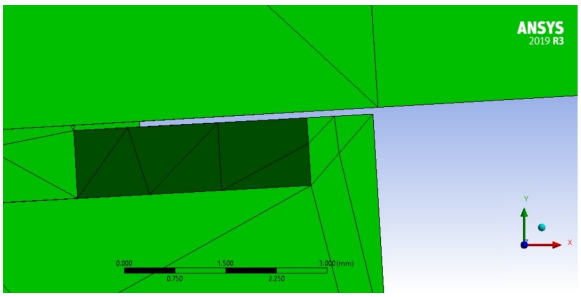

(b) Lower right side support piece.

Figure 6.9: Case 2 support pieces in separation (XY plane cross-section detail).

Figure 6.10 represents the plots from Ansys and from equations 3.82, 3.93 and 3.104 obtained in Chapter 3, which describe the beam's deflection along its axis.

These two plots allow us to compare the analytical and numerical deflection results. The values for the deflection were obtained from Ansys and it is possible to plot them in the same graph as the equations in order for both lines to be overlapping. It is visible that the values are very similar at the beginning and then tend to diverge from each other towards the tip. Nevertheless, the maximum values of deflection, which are visible, are not far from each other. The overlapping segment is well visible and in the same interval of values ($[x_a, x_b]$), in this case $[500, 600](mm)$, for both plots. In Ansys's plot, the segment is represented as the two lines on top of each other, a sign that at the overlap segment, there are two sets of values (one for the root and other for the tip segment), whereas in the equation plot, there is an equation that describes that same segment.

As stated earlier, this difference in values comes from the computational errors associated with the numerical analysis and also from the way that the structural model is built. Also, by assuming an Euler-Bernoulli beam the shear forces are negligible on the analytical analysis, whereas in numerical analysis, although with a small effect, they are not, which contributes to an existent difference of values towards the tip.

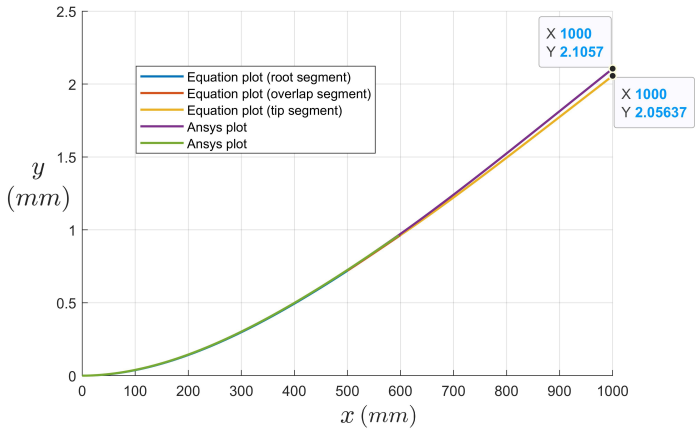

Figure 6.10: Case 2: Ansys and Equation graphs for deflection along the beam.

6.3 Case 3

Prior to the analysis of the results for Case 3, it is necessary to present the values for the constants K_{EI}, K_{L_2} and K_{L_0} and how those values were chosen. Figure 6.11 represent the beam's cross-sections, from which we can obtain I and therefore, the value of E to use for the tip segment.

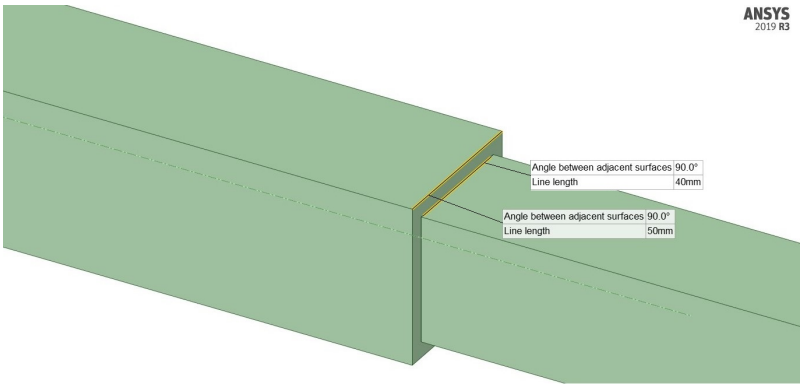

Figure 6.11: Case 3 beam's root and tip cross-section measures.

Similarly to the previous case, the root segment's cross-section is a hollowed square with a side length of $50mm$ and a thickness of $5mm$. This thickness is constant across the beam's axis. The tip segment has a squared cross-section with a side length of $40mm$. Knowing this, allows us to calculate the area moments of inertia and consequently the value of E_2 ($1.4414 \times 10^5 MPa$) for the tip segment which gives the desired ratio of $K_{EI} = 0.5$. The values for K_{L_2} and K_{L_0} are chosen, like on the previous chapter, 0.4 and 0.1, respectively

and the total length of the beam is $L = 1000mm$. With that data introduced in ANSYS, the following solution is visible in Figures 6.12 and 6.13.

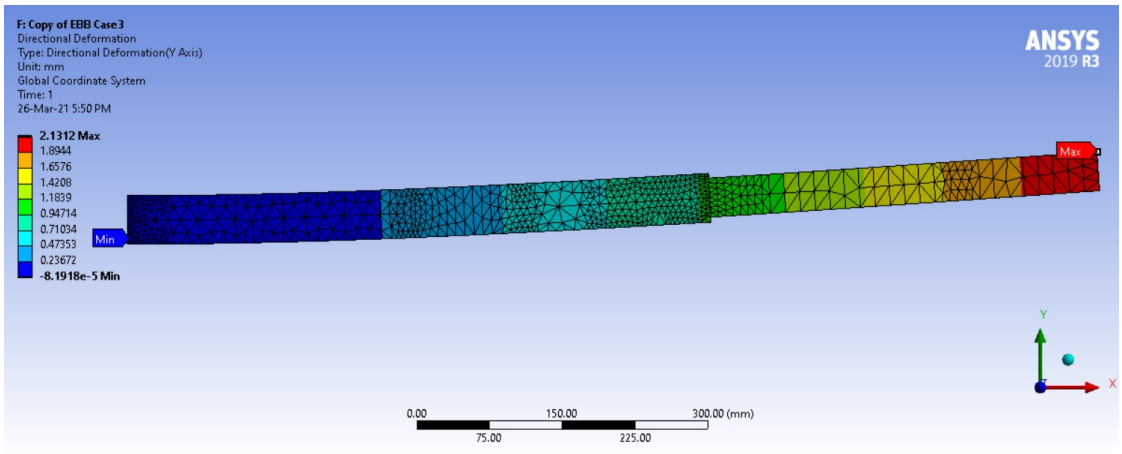

Figure 6.12: Directional deformation solution for Case 3 (side view).

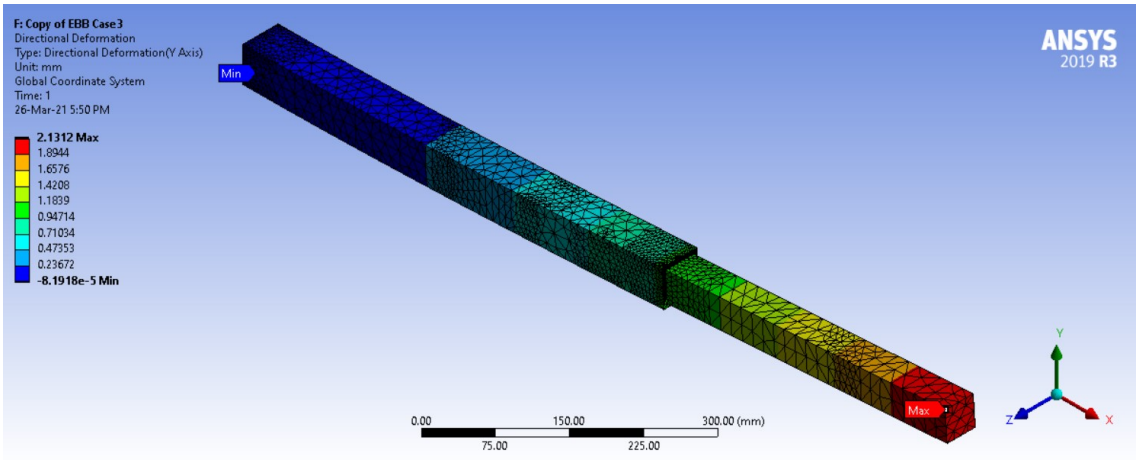

Figure 6.13: Directional deformation solution for Case 3 (isometric view).

The results appear in color, along the beam and the deflection is higher as we move closer to the tip of the beam. In blue we see small values of deformation and in red high values of deformation. The maximum value is visible and it is equal to $2.1312mm$.

Applying the chosen input values in equation 3.161 returns the value of the deflection at the tip of the beam, which is $2.0542mm$. Similarly to the second case, there is a difference between the numerical and analytical values, the latter being smaller. This is due to the assumptions considered in the Euler-Bernoulli beam theory, which neglects the effects of shear strains, amongst other. This does not happen in the numerical analysis, where every effect contributes to the results.

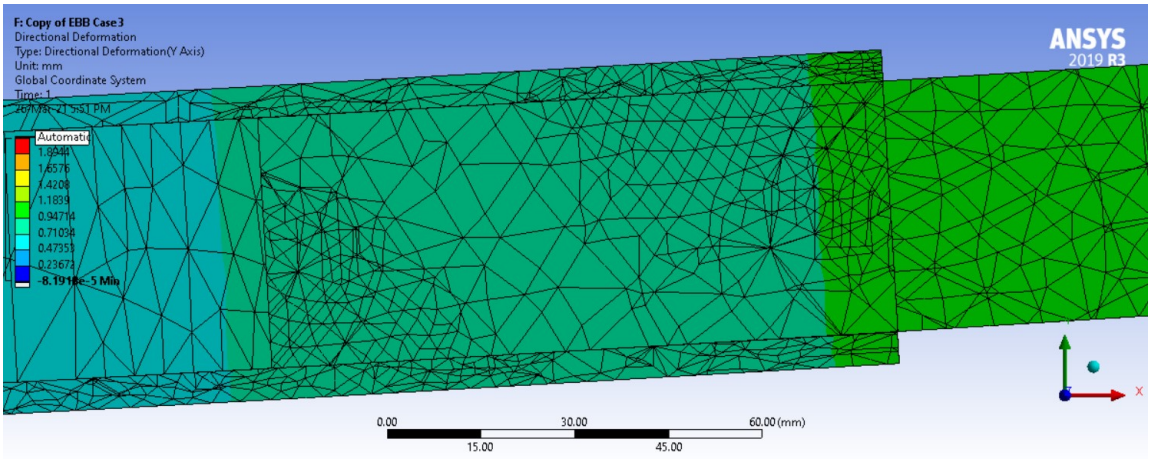

Figure 6.14: XY plane cross-sectional solution and internal mesh elements.

In Figure 6.14 it is possible to see how the contact surfaces between the root and tip segments react to the deformation by compressing against each other. By cross-sectioning the beam in the XY plane, we can see that the elements are smaller where compression is occurring and larger where the faces tend to separate.

Figures 6.15 (a) and (b) show how the two segments of the beam separate from each other due to the deformation. On the opposite direction, there are compression forces happening, which is consistent with the Figure above.

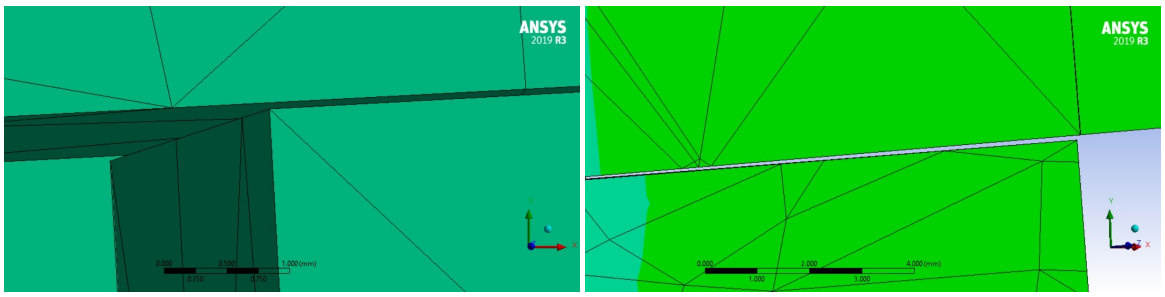

(a) Upper left side separation. (b) Lower right side separation.

Figure 6.15: Case 3 segments separating (XY plane cross-section detail).

In Figure 6.16 it is possible to see the plots from Ansys and the equations which describe the deflection from equations 3.137, 3.148 and 3.159, from Chapter 3.

Having the two plots from the different types of analysis in the same graph allows us to have an idea of how different the values are. It is visible that the values are mostly the same in the root segment and tend to diverge as we reach the tip segment. The values of the deflection at the tip are similar in both analysis and the inboard segment is well visible and within the same interval of values ($[x_a, x_b]$), particularly $[500, 600](mm)$, for both plots. The equation plots are similar to what was seen in the previous chapter and they are described by three equations: one for the root segment, one for the overlapping segment and one for the tip segment. For the plots extracted from Ansys, there are only two lines which represent the

two different bodies of the structural model and the overlapping segment is represented by those two lines also overlapping, which means that in that segment there are two sets of values for deflection.

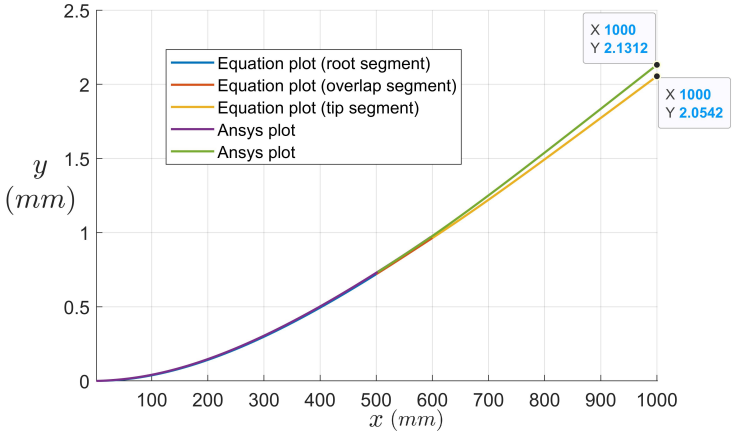

Figure 6.16: Case 3: Ansys and Equation graphs for deflection along the beam.

6.4 Comparison of the three cases

In this final Section, after all the analysis are performed and the results obtained, Table 6.1 is built in which both the analytical and numerical values of deflection for the three cases are analyzed as well as the difference between them are shown:

Table 6.1: Comparison of analytical and numerical results for tip deflection.

	Tip deflection (mm)		
	Analytical analysis	Numerical analysis	Relative difference
Case 1	1.2750	1.2736	0.001098
Case 2	2.0564	2.1058	0.024023
Case 3	2.0542	2.1312	0.036129

From Table 6.1 it is visible that the analytical analysis has higher value than the numerical analysis only for Case 1. This is most likely due to the fact that while in the analytical analysis boundary conditions exist for the point where the segments meet, when analyzed in Ansys this beam acts like a uniform beam even with the same boundary conditions applied. Due to the lack of overlapping segment, there is also no influence from the tip segment on the root segment.

In both Case 2 and Case 3 the numerical analysis has higher value than the analytical one, as expected. This is mostly due to the rotation that occurs on the interface between the root and tip segments, more than the fact that the Euler-Bernoulli beam theory neglects the transverse shear forces acting on the beam and other deformations such as the one explained in 6.2, whereas in Ansys that does not happen. Although the deflections and the cross-section dimensions are small comparing to the beam's length, it is not possible in Ansys to neglect the shear effects. This causes the numerical values to differ from the analytical ones. How-

ever, it is quite visible that the difference is small, being approximately 0.11% for Case 1, approximately 2.4% for Case 2 and approximately 3.6% for Case 3.

Although the difference in Case 3 is the highest, it is the one that shows a smaller deflection value in the analytical analysis. Case 2 is the one that shows a smaller deflection value in the numerical analysis.

From these results, it is safe to admit that the equations obtained using the Euler-Bernoulli beam theory accurately describe the rotation and deflection of the telescopic beam model and the results from ANSYS support these results, thus obtaining the desired *Verification*.

From 5.3.3 it is possible to see that the margin of inboard length hypothesised in the beginning of this study is real. Case 3 type of support is the one that allows a lower value of deflection in that interval of segment length.

Chapter 7

Conclusion

The use of telescopic wings in aviation has been studied for a long time now and its contributions are known to be extremely positive in terms of adaptation and multifunctionality to whatever mission the aircraft needs to perform.

The study approached in this dissertation appeared with the purpose of simplifying the complex geometry of telescopic wings and its structural models into more simple beam geometries in order to analyze its displacements. Different types of supports were analyzed in order to understand how they would change the rotation and deflection at the tip of the beams as well as the overall displacements.

Understanding how a telescopic mechanism works, it is normal to think that the longer the mechanism is, i.e. a more extended telescopic segment, the larger the deflection would be on the tip of the beam. Since studies [13] have shown that there could be a margin of overlapping segment where it was possible to experience a decreasing deflection value before starting to reach larger and undesirable values, it was of the utmost importance to verify if such hypothesis was valid and how could it be predicted for future use.

Choosing an analytical theory that would enable a simple and effective study of the displacements and obtention of equations that could describe those displacements accurately using simple input variables was the first step. The Euler-Bernoulli beam theory was used for every case but the boundary conditions and reactions needed to be adapted to each type of mechanism studied.

After the equations were obtained, there was a need for them to be validated. Applying a numerical analysis through the use of Finite Element Methods was the logical choice. Making use of the computational tool Ansys enabled to create different structural models that would then be analyzed by applying mesh methods and boundary conditions that would simulate the desired behaviors of the beams. With the obtained results, it was possible to understand if the goal of the study was achieved.

The results showed that the equations accurately describe, for a preliminary project, the behavior of each telescopic mechanism and its displacements and that the difference between the analytical and numerical analysis are relatively small comparing to the order of magnitude of the results. Between Case 2 and 3, Case 3 proved to be the one to obtain smaller displacements in the analytical analysis and Case 2 the one to obtain smaller displacements

in the numerical analysis.

From the analytical analysis it was proven the main goal of this study: there is indeed an ideal margin of inboard segment length that produces a minimal deflection, with the exception of a fully closed telescopic configuration equivalent to a regular uniform beam, that can be calculated using simple beam characteristics that are known.

It was also verified that, for some values of length ratios and flexural rigidity ratios, the deflection of a telescopic beam can actually be smaller than a regular uniform beam.

7.1 Future Work

Implementing new assumptions to this study could give extra insight on the way that the deflection depends on said ratios. The most interesting would be, to obtain the tip deflection for different extended tip parts such as: $L = L_1 + L_2$, $L_1 > L_0 + L_2$, $L' = L_1 + L'_2$ and $L'_0 = L_0 + L - L'$, where L', L'_0 and L'_2 represent the respective segment length, after the movement. This would mean that if the L_2 segment ought to decrease in length, the inboard L_0 segment would increase in the same proportion, and vice-versa. This way, the total length of the beam would also depend on the inboard segment's length, being more accurate if a physical structural model ought to be built and tested.

Studying the analytical model with a different theory such as Timoshenko's beam theory could lead to more accurate results between the analytical and the numerical analysis. Studying the strains and deformations at the interface would benefit in order to understand how much they affect the results obtained.

Applying this study to a telescopic wing configuration would also be interesting so to see if the same results can be expected and what and how would they be different. This could lead to the construction of a computational tool, based on the analytical calculations and theories, that would predict the structural behaviors of the telescopic mechanisms for future use in the aeronautical industry.

Bibliography

[1] Radovan Richta, "The scientific & technological revolution," *Australian Left Review*, pp. 54–67, 1967.

[2] L. D. Horst Baier, "Active and morphing aerospace structures-a synthesis between advanced materials, structures and mechanisms," *International Journal of Aeronautical and Space Sciences*, vol. 12, pp. 225–240, 2011.

[3] D. Li, S. Zhao, A. Da Ronch, J. Xiang, J. Drofelnik, Y. Li, L. Zhang, Y. Wu, M. Kintscher, H. P. Monner, A. Rudenko, S. Guo, W. Yin, J. Kirn, S. Storm, and R. de Breuker, "A review of modelling and analysis of morphing wings," *Progress in Aerospace Sciences*, vol. 100, pp. 46–62, 2018.

[4] T. A. Weisshaar, "Morphing aircraft technology – new shapes for aircraft design," *Multifunctional Structures / Integration of Sensors and Antennas*, vol. RTO-MP-AVT-141, pp. 1–20, 2006.

[5] A. Sofla, S. A. Meguid, K. T. Tan, and W. K. Yeo, "Shape morphing of aircraft wing: Status and challenges," *Materials & Design*, vol. 31, no. 3, pp. 1284–1292, 2010.

[6] S. Barbarino, O. Bilgen, R. M. Ajaj, M. I. Friswell, and D. J. Inman, "A review of morphing aircraft," *Journal of Intelligent Material Systems and Structures*, vol. 22, no. 9, pp. 823–877, 2011.

[7] G. Reich and B. Sanders, "Introduction to morphing aircraft research," *Journal of Aircraft*, vol. 44, no. 4, p. 1059, 2007.

[8] R. Ajaj, A. Keane, D. Inman, "Morphing aircraft- the need for a new design philosophy," *7th Ankara International Aerospace Conference*, 2013.

[9] Neal D.A., Good M.G., Johnston C.O., Robertshaw H.H., Mason W.H., Inman D.J., "Design and wind-tunnel analysis of a fully adaptive aircraft configuration," *45th AIAA/ASME/ASCE/AHS/ASC Structures, Structural Dynamics and Materials Conference*, vol. 1727, pp. 1–9, 2004.

[10] Daniel P. Raymer, *AIRCRAFT DESIGN: A Conceptual Approach*. American Institute of Aeronautics and Astronautics, 1992.

[11] J.-P. Chivot, "Des ailes en long ou en travers," (Accessed: 20/08/2020). [Online]. Available: https://www.aerovfr.com/2020/08/des-ailes-en-long-ou-en-travers/

[12] Mak-101, “Авиационная энциклопедия: Уголок неба (aviation encyclopedia),” (Accessed: 20/08/2020). [Online]. Available: http://www.airwar.ru/enc/xplane/mak10.html

[13] Rui Filipe Martins Fernandes Cunha, “Structural analysis of a variable-span wing-box,” Master Thesis, Universidade da Beira Interior, 10/2014.

[14] “Beam types,” (Accessed: 22/08/2020). [Online]. Available: http://semesters.in/definition-and-types-of-a-beam-notes-pdf-ppt/lecture-9-shear-force-and-bending-moment-in-beams-6-728/

[15] O. A. Bauchau and J. I. Craig, *Structural analysis: With applications to aerospace structures*, ser. Solid mechanics and its applications. Dordrecht and New York: Springer, 2009, vol. 163.

[16] C. Wang, “Timoshenko beam-bending solutions in terms of euler-bernoulli solutions,” *Journal of Engineering Mechanics*, vol. 121, no. 6, 1995.

[17] “bernoulli beam,” (Accessed: 28/08/2020). [Online]. Available: https://en.m.wikipedia.org/wiki/Euler%E2%80%93Bernoulli_beam_theory#

[18] J. M. Gere and S. P. Timoshenko, *Mechanics of Materials*. PWS Publishing Company, 1997.

[19] C. M. Wang, S. Kitipornchai, C. W. Lim, and M. Eisenberger, “Beam bending solutions based on nonlocal timoshenko beam theory,” *Journal of Engineering Mechanics*, vol. 134, no. 6, pp. 475–481, 2008.

[20] “Timoshenko beam,” (Accessed: 31/08/2020). [Online]. Available: https://en.wikipedia.org/wiki/Timoshenko-Ehrenfest_beam_theory

[21] R. Feynman, Leighton, R. B., and M. Sands, *The Feynman Lectures on Physics: Mainly Electromagnetism and Matter*, 1989, vol. 2.

[22] T. Beléndez, C. Neipp and A. Beléndez, “Large an small deflections of a cantilever beam,” *European Journal of Physics*, vol. 23, 2002.

[23] E. Oñate, *Structural Analysis with the Finite Element Method. Linear Statics: Volume 1: Basis and Solids*, 1st ed. Springer, 2009, vol. 1.

[24] J. N. Reddy, *Introduction to the Finite Element Method*, 2nd ed. McGraw-Hill, 1993.

[25] C. M. Cyclopedia, “Finite element mesh refinement,” (Accessed: 03/02/2021). [Online]. Available: https://br.comsol.com/multiphysics/mesh-refinement

[26] A. Inc., “Ansys spaceclaim 3d modeling software,” (Accessed: 16/05/2021). [Online]. Available: https://www.ansys.com/products/3d-design/ansys-spaceclaim